UNIVERSITY OF CALIFORNIA,
IRVINE

Addressing the Reactor Antineutrino Anomaly with a New Detector Array for Fission Fragment Beta-Spectroscopy

DISSERTATION

submitted in partial satisfaction of the requirements
for the degree of

DOCTOR OF PHILOSOPHY

in Physics

by

Elizabeth Klara Marie Heckmaier

Dissertation Committee:
Professor Franklin Dollar, Chair
Professor A. J. Shaka
Professor Henry W. Sobel

2018

DEDICATION

For my family and fourteen-year-old me, who decided the most wonderful way to spend one's time was to learn a great deal about impossibly small things.

TABLE OF CONTENTS

LIST OF FIGURES

LIST OF TABLES

Page

ACKNOWLEDGMENTS

I would like to acknowledge the numerous individuals who have helped to make this work possible.

At UCI, I offer my many thanks to Professor Dollar and Professor Sobel for very kindly agreeing to serve on my dissertation committee, and their valuable feedback. Thank you also to Dr. Nilsson for serving on my advancement committee and folding me into the larger nuclear science group.

I must extend my sincere gratitude to Dr. Shaka for his wisdom, advice, and incredible dedication in ensuring the success of his students. I absolutely cannot thank him enough.

At LLNL, I would like to gratefully acknowledge Dr. Nicholas Scielzo for serving as my mentor and allowing me to work on this exciting project—none of this would be possible without his invaluable guidance, assistance, and patience. Thank you as well to Stephen Padgett, for his help in preparing for the experiment. Many thanks to Justin Munson for teaching me about HPGe detectors and his hard work before, during, and after the run.

At Argonne, I would like to thank Guy Savard and Jason Clark for their assistance in preparing for the experiment, troubleshooting, and providing me with wonderful beam. I would also like to thank Brad DiGiovine, for his help with the tape station and allowing me use of his nice power supplies. Shaofei Zhu and Mike Carpenter were absolutely indispensable, and I very much appreciate their assistance with the data acquisition system. Thank you to Mary Burkey and the others in the amazing ^{8}Li/BPT group, as well as the lab's outstanding support staff.

I would also like to thank the Nuclear Science and Security Consortium for their funding assistance and abundance of professional development opportunities.

I am indebted to my amazing friends, Ben, Jessica, and Rachel for providing me with much needed reprieves from the rigors of graduate school over these many years.

My family has been a steady source of strength over the years. Thank you to my mother, for serving as my biggest cheerleader, and my father, for his constant encouragement. Any achievement would not be possible without their unfaltering support and love.

Lastly, but not least, I would like to thank Eric, my wonderful partner of 10 years, for his love and encouragement—I am extraordinarily fortunate.

This material is based upon work supported by the Department of Energy National Nuclear Security Administration through the Nuclear Science and Security Consortium under Award Number(s) DE-NA0003180. This research used resources of Argonne National Laboratory's ATLAS facility, which is a DOE Office of Science User Facility.

CURRICULUM VITAE

Elizabeth Klara Marie Heckmaier

EDUCATION

Doctor of Philosophy in Physics **2018**
University of California, Irvine

Dissertation: "Addressing the Reactor Antineutrino Anomaly with a New Detector Array for Fission Fragment Beta-Spectroscopy"

Chair: Professor F. Dollar (University of California, Irvine).

Advisor: Professor A. J. Shaka (University of California, Irvine).

Principal Investigator: Dr. N. D. Scielzo (Lawrence Livermore National Laboratory).

Masters of Science in Physics **2013**
University of California, Irvine

Bachelor of Arts in Physics **2009**
University of California, Berkeley

PUBLICATIONS AND PRESENTATIONS

E. K. M. Heckmaier, N. D. Scielzo, et al., "A New Detector Array for First-Forbidden Beta-Decay Transitions and Spectra Measurements" (in preparation)

E. K. M. Heckmaier, N. D. Scielzo, et al., "Direct Beta Spectra Measurements of ^{92}Rb and ^{96}Y" (in preparation)

E. K. M. Heckmaier, N. D. Scielzo, et al., "A Novel Method of Plastic Scintillator Calibration for Fission Fragment Beta-Spectroscopy" (in preparation)

T.Y. Hirsh, et al., The use of cosmic-ray muons in the energy calibration of the Beta-decay Paul Trap silicon-detector array, Nucl. Instrum. Methods Phys. Res. A, 887 (2018), pp. 94-100, https://doi.org/10.1016/j.nima.2018.01.021.

E. K. M. Heckmaier, N. D. Scielzo, A. J. Shaka, M. Nilsson, "A New Detector Array for Fission Fragment Beta Spectroscopy," (2017), poster presented at NSSC September Workshop and Advisory Board Meeting

E. K. M. Heckmaier, N. D. Scielzo, A. J. Shaka, "Addressing the Reactor Antineutrino Anomaly with Fission Fragment Beta Spectroscopy," (2017), poster presented at NNSA University Program Review Meeting

E. K. M. Heckmaier, N. D. Scielzo, A. J. Shaka, "Plastic Scintillator Calibration for Fission Fragment-Spectroscopy," (2016), poster presented at University and Industry Technical Interchange (UITI) Program and Technical Review Meeting

A. J. Mitchell, et al., "Recent advances in β-decay spectroscopy at CARIBU," EPJ Web Conf., 123 (2016) 04006. https://doi.org/10.1051/epjconf/201612304006

E. K. M. Heckmaier, N. D. Scielzo, A. J. Shaka, "Simulation Studies of a New Detector Array for ^{92}Rb and ^{96}Y Beta-Spectroscopy Experiments," (2015), poster presented at University and Industry Technical Interchange (UITI) Program and Technical Review Meeting

E. K. M. Heckmaier, C. A. Schoepke, et al., "Development of Experimental Physics Capabilities at U.C. Berkeley for National Security-Related Research," (2009), poster presented at the 1st Workshop on Special Topics in Homeland Nuclear Security

RESEARCH EXPERIENCE

Graduate Research Assistant, Shaka Group **2014 - Present**
University of California, Irvine

Commissioned a new beta detector array at Argonne National Laboratory.

Developed detector simulations using Geant4.

Analyzed the beta spectra of short-lived fission products to probe the reactor antineutrino anomaly.

Post-Baccalaureate Research Assistant, Accelerator & Fusion Research Division **2010**
Lawrence Berkeley National Laboratory

Aided in the design of the beamline for a retrofitted 3.5 MeV electron accelerator located on the UC Berkeley campus.

Performed electron optics calculations and beam modeling for applications to Nuclear Resonance Florescence experiments.

Undergraduate Research Assistant, Morse Group **2009**
Department of Nuclear Engineering
University of California, Berkeley

Retrofitted a 7 MeV tandem deuteron accelerator into a 3.5 MeV electron accelerator for the Domestic Nuclear Threat Security (DoNuTS) Initiative.

Installed and aligned charging chains, beam tube, vacuum and beam profile systems.

Undergraduate Research Assistant, Edelstein Group **2007 - 2008**
Space Sciences Laboratory
University of California, Berkeley

Performed spectroscopic data analysis of Spitzer Space Telescope IRS images of interstellar medium in the Cygnus Loop supernova remnant.

Undergraduate Research Assistant, Smoot Group **2006 - 2007**
Department of Physics
University of California, Berkeley

Expanded www.universeadventure.org, an educational website for cosmology and astrophysics outreach.

ACADEMIC EXPERIENCE

Teaching Assistant **2013**
Department of Mathematics
University of California, Irvine

Teaching Assistant **2010 - 2012**
Department of Physics and Astronomy
University of California, Irvine

Assistant **2008 - 2009**
Physics Instructional Labs, Department of Physics
University of California, Berkeley

Grader **2007**
Department of Astronomy
University of California, Berkeley

PROFESSIONAL DEVELOPMENT

Nuclear Science and Security Consortium

Nuclear Safeguards Summer School **2017**
Los Alamos National Laboratory

Public Policy and Nuclear Threats (PPNT) Boot Camp **2016**
University of California Institute on Global Conflict
and Cooperation (IGCC)

ABSTRACT OF THE DISSERTATION

Addressing the Reactor Antineutrino Anomaly with a New Detector Array for Fission Fragment Beta-Spectroscopy

By

Elizabeth Klara Marie Heckmaier

Doctor of Philosophy in Physics

University of California, Irvine, 2018

Professor Franklin Dollar, Chair

Since the discovery of the neutrino in 1956, nuclear reactors have played an important role in understanding the properties of beta decay and probing the nature of the weak interaction. Repeatedly, reactor-based experimental studies of neutrino oscillations have observed a deficit in measured values of antineutrino flux relative to the flux predicted by prominent fissile antineutrino models [7, 2]. Most recently, the Daya Bay experiment reported measured antineutrino flux relative to the number predicted by current models of reactor antineutrino spectra of 0.946 ± 0.022 [10]. Several explanations have been put forward, including the possibility of new physics beyond the standard model (e.g., sterile neutrinos), or deficiencies in current models of ^{235}U fission product beta spectra [19]. This work describes efforts to directly measure the beta spectrum of ^{92}Rb, one of the largest contributors to the aggregate ^{235}U antineutrino spectrum, using a new detector array constructed at Argonne National Laboratory's CARIBU user facility.

Chapter 1

Introduction and Overview

1.1 The Standard Model

1.1.1 Particles of the Standard Model

The prevailing Standard Model (SM) of particle physics is the culmination of decades of experimental and theoretical efforts to describe matter and interactions at the most fundamental level. Particles of the Standard Model are grouped as fermions (particles with half-integer spin, obeying Fermi-Dirac statistics), or bosons (particles with integer spin, following Bose-Einstein statistics).

Matter particles are fermions that are sub-classified into quarks or leptons, grouped by the manner in which they interact. Charged fermions interact via the electromagnetic force (mediated by the photon); however all fermions interact weakly (via $W^{\pm}$ and Z gauge bosons). Quarks are distinguished from leptons by strong force (gluon) interactions. There are 3 identifiable mass-generations of matter particles, sub-grouped into 6 varieties (flavors)

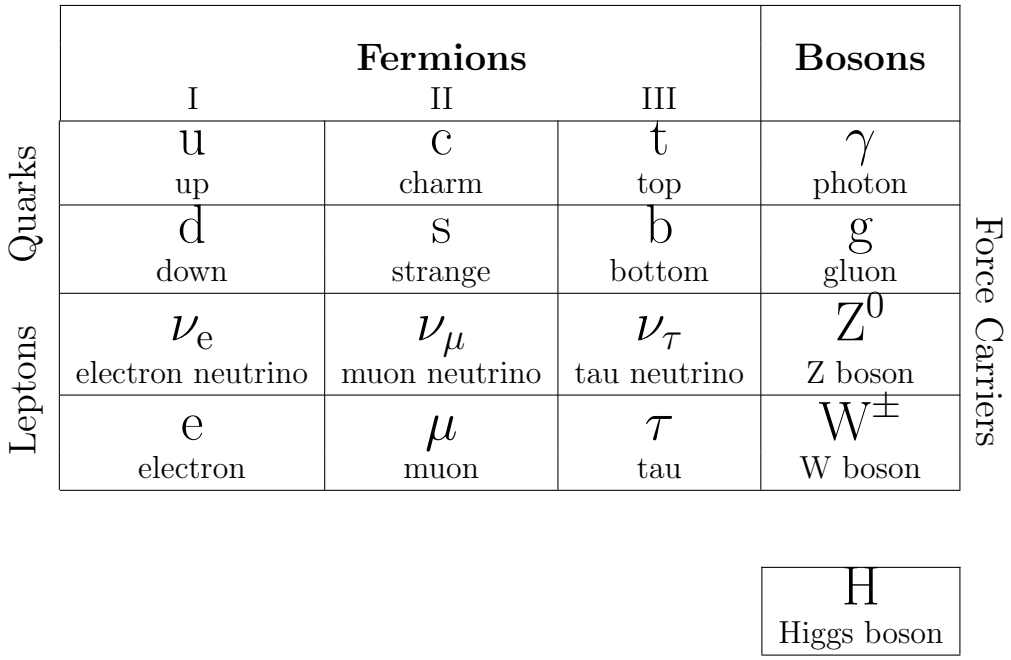

Figure 1.1: Fundamental Particles of the Standard Model

of quarks and 6 varieties of leptons. The 3 generations of quarks identified by $+2/3$ charge are collectively named "up-type" quarks, with 3 flavors: *up*, *charm*, and *top*. The other 3 generations of $-1/3$ charge are "down-type" quarks, with 3 flavors: *down*, *strange*, and *bottom*. Quarks (and gluons) additionally exhibit color charge; this is the strong interaction.

A strong force-bound collection of quarks comprise hadrons. Of the hadrons, baryons are a composition of odd-numbered quarks or antiquarks; 3 being the minimum and most common. The everyday proton contains 2 up-quarks and 1 down-quark, while the neutron consists of 2 down-quarks and 1 up-quark. Even-numbered combinations (2 the minimum and most common) of quarks and antiquarks are mesons; having integer spin, they are not fermions but bosons.

Leptons are likewise classified into 3 generations as e, μ, or τ (with electric charge ± 1), each with an interaction-partner, an electrically-neutral neutrino: ν_e, ν_μ, ν_τ. For every fermion flavor there exists an antiparticle with the same mass, but opposite electric and color charge.

Bosons of the Standard Model include a spin-0 Higgs, mesons, and the spin-1 vector gauge bosons. The vector gauge bosons are the photon, $W^{\pm}$ and Z, and the gluon (mediating the electromagnetic, weak, and strong interactions respectively). The Higgs boson interaction is responsible for the electroweak symmetry breaking phenomenon, resulting in massive $W^{\pm}$ and Z bosons, with a massless photon. The short effective range of the weak interaction is a result of the large $W^{\pm}$ and Z masses.

1.1.2 Electroweak Interactions

Under the fundamental representation of $SU(2)$, fermion fields may be decomposed into "left-handed" doublets

$$\Psi_{Li} = \begin{pmatrix} \nu_i \\ l_i \end{pmatrix} \text{ and } \Psi_{Qi} \begin{pmatrix} u_i \\ d'_i \end{pmatrix} \text{ where } i \text{ runs over the 3 fermion generations} \tag{1.1}$$

and "right-handed" singlet chiral components

$$q_i \text{ where } q = u \text{ or } d \qquad\qquad l_i \text{ where } l = e, \mu, \tau \tag{1.2}$$

Transformations under $SU(2)$ act exclusively on left-handed particles, and the generators of the group are associated with the weak isospin quantum number given by $Q = \frac{1}{2} + T_3$.

Unification of the electromagnetic and weak interactions requires the introduction of a new conserved current called weak hypercharge (Y) to relate the usual electric charge (Q) to the third component of weak isospin

$$T_a = \frac{1}{2}\tau_a \qquad\qquad a = 1, 2, 3 \tag{1.3}$$

where τ_a denotes the 2×2 Pauli matrices

$$\tau_1 = \begin{pmatrix} 0 & 1 \\ 1 & 0 \end{pmatrix} \qquad \tau_2 = \begin{pmatrix} 0 & -i \\ i & 0 \end{pmatrix} \qquad \tau_3 = \begin{pmatrix} 1 & 0 \\ 0 & -1 \end{pmatrix} \tag{1.4}$$

satisfying an algebra

$$[T^a, T^b] = i\epsilon^{abc} T^c \tag{1.5}$$

The use of τ here indicates their action on the $SU(2)_L$ indices, rather than σ which denotes action on the usual spinor indices.

Similar to QED, a massless gauge field singlet lies in the adjoint representation of $U(1)$, denoted B_μ and

$$B_{\mu\nu} = \partial_\mu B_\nu - \partial_\nu B_\mu \tag{1.6}$$

The factors associated with $SU(2)$ form a triplet of massless gauge fields W^a_μ with field tensor $W^a_{\mu\nu} = \partial_\mu W^a_\nu - \partial_\nu W^a_\mu + g_2 \epsilon_{abc} W^b_\mu W^c_\nu$ in the adjoint representation.

The electroweak covariant takes the form

$$D_\mu = \partial_\mu - i g_2 W^a_\mu T_a - \frac{i g_1 Y}{2} B_\mu \tag{1.7}$$

to account for the disparity between left-handed fermions and right-handed fermions in electroweak interactions.

The electroweak Lagrangian (which governs nuclear beta decay), then, is given by

$$\mathcal{L} = \overline{\Psi}_{Qi} i\gamma^\mu D_\mu \Psi_{Qi} + \overline{\Psi}_{Li} i\gamma^{mu} D_{mu} \Psi_{Li} + \overline{q}_i i\gamma^{mu} D_\mu q_i + \bar{l}_i i\gamma^{mu} D_\mu l_i - \frac{1}{4} W^{\mu\nu} W_{\mu\nu} - B^{\mu\nu} B_{\mu\nu}. \tag{1.8}$$

1.2 Beta Decay Phenomenology

1.2.1 The Fermi Theory of Beta Decay

The following section presents a review of the Fermi Theory of Beta Decay and summarizes the parameters necessary to describe the beta spectrum shape.

From Enrico Fermi's seminal paper in 1934 [16], the beta spectrum for an allowed decay is given by:

$$N_\beta(W) = Kp^2 (W - W_0)^2 F(Z, W), \tag{1.9}$$

where $p^2 (W - W_0)^2$ denotes the spectral phase space (which is modified for forbidden transitions), K is the normalization constant, $W = 1 + E/(m_e c^2)$, p is the momentum of the beta particle ($\sqrt{W^2 - 1}$), and W_0 is at the endpoint energy.

In QED, the Fermi function, $F(Z, W)$, provides the leading order correction to beta decay and accounts for the interaction of the outgoing electron with the nucleus's Coulomb field and takes the form

$$F(Z, W) = 2(\gamma + 1)(2pR)^{2(\gamma-1)} e^{\pi\alpha ZW/p} \frac{|\Gamma(\gamma + i\alpha ZW/p)|^2}{\Gamma(2\gamma + 1)^2}$$

$$\text{with } \gamma = \sqrt{1-(\alpha Z)^2}, \text{ and } R, \text{ the nuclear radius.} \tag{1.10}$$

In practice, the Fermi function is difficult to calculate, but values have been tabulated for many isotopes.

If higher-order loop-level interactions are considered, the beta spectrum is modified by several fractional corrections, taking the form

$$\begin{aligned} N_\beta(W) =& Kp^2 (W - W_0)^2 F(Z,W) L_0(Z,W) \\ & \times C(Z,W) S(Z,W) G_\beta(Z,W) (1 + \delta_{\mathrm{WM}} W) \end{aligned} \tag{1.11}$$

The electromagnetic effect of the finite size of the nucleus (that is, when the electric charge distribution in the nucleus is no longer modeled as a point) is described by the term L_0, while $C(Z,W)$ accounts for weak interaction finite-size corrections in Gamow-Teller decays. The term $G_\beta(Z,W)$ represents radiative corrections, introduced by emission of virtual and real photons at the loop-level by charged particles, necessary for renormalization. The screening effect of the nuclear charge from the Coulomb field of the daughter nucleus by the bound electrons is held in $S(Z,W)$.

The weak magnetism correction, δ_{WM}, is the induced current due to interference between the magnetic moment of the daughter nucleus and the outgoing electron. For Fermi transitions, the weak magnetism correction is absent. Neglecting all other corrections (small in

comparison), the weak magnetism term modifies the allowed spectral shape of β decay by a factor of

$$1 + \delta_{\mathrm{WM}} W \tag{1.12}$$

where $\delta_{\mathrm{WM}} = \frac{4}{3}\frac{b}{Mc} m_e$. Here, c is the Gamow-Teller matrix element for the vector and axial currents, and $b = \sqrt{2\mu}$. $M = AM_N$ is the nucleus's mass and μ is the conventional magnetic transition moment. For light nuclei, the leading-order weak magnetism correction may be approximated [24] as

$$\delta_{\mathrm{WM}} = \frac{0.5\% W}{MeV}. \tag{1.13}$$

The antineutrino spectrum may be deduced from the beta spectrum via a conservation of energy replacement $E_{\bar{\nu}} = E_0 - E_e$.

1.2.2 Neutrino Oscillations

Experiments involving solar, atmospheric, and reactor neutrinos have provided extensive evidence for a phenomenon known as neutrino oscillations, whereby a neutrino of one flavor type changes into a neutrino of a different flavor as it propagates. Such flavor mixing emerges in the current formulation of the SM if neutrinos are permitted to carry non-zero mass. One possible way to introduce neutrino masses is to add a non-renormalizable term to the usual electroweak Lagrangian.

The corresponding neutrino mass matrix is given by

$$M_\nu = Y_\nu \frac{v^2}{M_*} \tag{1.14}$$

where M_* is a mass scale much higher than that of the weak interaction.

In the seesaw mechanism description of neutrino masses, the mass scale is on the order of a very heavy (and as of yet unobserved) partner neutrino, specifically the right handed neutrino.

Conveniently, the mass matrix's inverse dependence on the heavy M_* provides an explanation for the apparent suppression of neutrino masses.

The electroweak charged current interaction Lagrangian in the lepton sector is now

$$\mathcal{L} = -\frac{g_2}{\sqrt{2}} \left[\overline{\nu}_i V_{ai} \nu_j\right] W_\mu \tag{1.15}$$

and the unitary transformation relating the neutrino flavor eigenstate to a mass eigenstate is

$$\begin{aligned}
&\nu_a = V_{ai}\nu_i \\
&V_{ai} = \begin{pmatrix} c_{12}c_{13} & s_{12}c_{13} & s_{13}e^{-i\delta} \\ -s_{12}c_{13} - c_{12}s_{23}s_{13}e^{i\delta} & c_{12}c_{23} - s_{12}s_{13}e^{i\delta} & s_{23}c_{13} \\ s_{12}s_{23} - c_{12}c_{23}s_{13}e^{i\delta} & c_{12}s_{23} - s_{12}c_{23}e^{i\delta} & c_{23}c_{13} \end{pmatrix} \\
&c_{ai} = \cos\theta_{ai} \\
&s_{ai} = \cos\theta_{ai}
\end{aligned} \tag{1.16}$$

where a runs over flavor states and i runs over mass states. If neutrinos are taken to be identical to antineutrinos (Majorana particles), then the matrix is diagonal and the first two

non-zero entries are multiplied by an additional phase factor. V_{ai} is the lepton analogue of the CKM matrix describing quark flavor mixing, known as the PMNS matrix.

Evidence of a non-weakly interacting, fourth-generation neutrino would be an important source of new physics beyond the Standard Model and lend support to astrophysical theories postulating sterile neutrinos as a constituent of Dark Matter.

1.2.3 The Reactor Antineutrino Anomaly

First used by Reines and Cowan to detect the antineutrino (1955), nuclear reactors have been instrumental in studying the properties of neutrinos and understanding the weak interaction. Various experiments [12, 13] to determine the mass splitting between the three neutrino flavors have reported excesses of electron antineutrinos relative to predictions. High-statistics reactor antineutrino experiments repeatedly report a deficit in measured antineutrinos relative to calculations based on current models of nuclear reactor antineutrino spectra. This apparent deficit has been termed the "reactor antineutrino anomaly." In 2016, the Daya Bay collaboration reported $0.946 \pm 0.022\%$ in measured reactor antineutrino flux relative to model-based calculations [10].

Several explanations have been put forward to explain this apparent deficit, including extensions to the Standard Model in the form of the addition of a fourth, undetected "sterile neutrino" that does not participate in electroweak interactions (mentioned in Section 1.2.2). Accounting for the discrepancy would require a mass-squared difference of 1 eV^2/c^4 or greater—much larger than any currently measured differences in the three neutrino flavor model. IceCube [1] and Daya Bay [4, 11] have further constrained the sterile neutrino phase space, but the deficit persists.

An alternative explanation for the antineutrino deficit suggests existing mathematical models of reactor beta spectra do not accurately characterize the beta spectra of several major fission fragments. Currently, there are two approaches to model the reactor antineutrino spectrum: the "summation" approach and the "conversion" approach.

The conversion approach utilizes measurements of aggregate beta spectra from ^{235}U, ^{239}Pu, and ^{241}Pu following fission at the Institut Laue-Langevin (ILL) reactor. This total spectrum is fit with a set of "virtual endpoint" energies of individual beta branches having assumed amplitude and spectral corrections based on existing information from nuclear databases as

$$\frac{dN_i}{dE_e} = \sum_i a_i P\left(E_e, E_0^i, Z\right), \tag{1.17}$$

where i runs over the individual fissile beta branches, a_i is the amplitude of that branch's endpoint energy from the fit to the measured aggregate spectrum, and $P\left(E, E_0^i, Z\right)$ denotes the assumed spectral shape of the branch.

This spectrum is then converted to the total corresponding antineutrino spectrum by the replacement of E_e with $E_0^i - E_{\bar{\nu}}^i$ [24]. However, assumptions must be made about the spectral shape of each branch and the endpoint energies used for the fit are informed by existing nuclear data, which may be uncertain (or unmeasured) for some branches.

In the summation approach, tabulated information from nuclear structure databases, such as measured branching ratios and endpoint energies, are used to determine the beta spectrum

of an individual fission fragment. These discrete beta spectra are summed together and weighted by their individual yield in fission as

$$\frac{dN_i}{dE_{\bar{\nu}}} = \sum_n Y_n\left(Z, A, t\right) \sum_{n,i} b_{n,i}\left(E_0^i\right) P_{\bar{\nu}}\left(E_{\bar{\nu}}, E_0^i, Z\right), \tag{1.18}$$

with $Y_n\left(Z, A, t\right)$ representing the number of beta decays of a fission fragment and $b_{n,i}$ is the branching ratio [21].

As such, the summation approach suffers from uncertainties in existing fission fragment decay data (e.g., total fission product yields and branching ratios).

Regardless of the approach, both methods rely on accurate nuclear data of the fission fragments and a good understanding of the individual branch spectral shape. Even small corrections to this data can significantly impact predictions of the antineutrino spectrum [35].

1.2.4 The Reactor Neutrino Shoulder

Increased precision at reactor experiments has pointed to yet another discrepancy between model-based calculations and measurements concerning the shape of the overall reactor spectrum. Consistently, measurements at Daya Bay [6], RENO [34] and Double Chooz [3] find an excess in the region of 4 to 6 MeV (or 5 to 7 MeV in the antineutrino spectrum) relative to prediction from the conversion approach. While over 800 different fission fragments contribute to the total antineutrino spectrum, the overall spectral shape is dominated by a relatively small number of isotopes. The distortion induced by these fission fragments of note is more apparent at higher energies. Examining the aggregate ^{235}U thermal spectrum

from 5 to 7 MeV (Figure 1.2), one isotope in particular stands out: ^{92}Rb. Taken alone, ^{92}Rb contributes 21.6% to the ^{235}U antineutrino spectrum around 5.5 MeV [35, Figure 1].

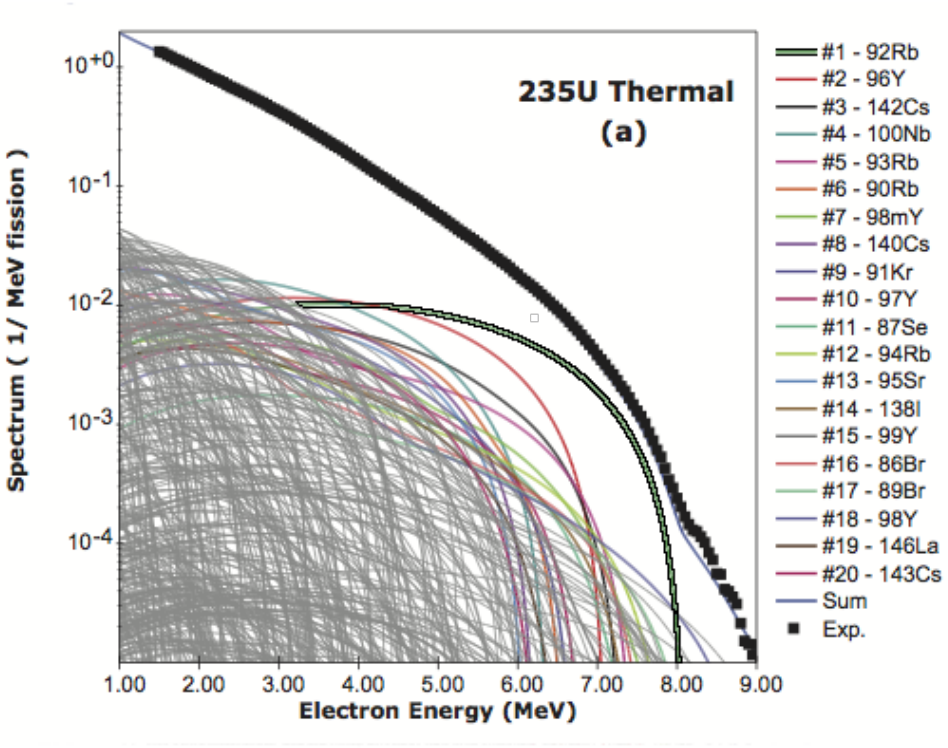

Figure 1.2: The calculated ^{235}U spectrum. The bold, green line represents the calculated ^{92}Rb beta spectrum used in the summation method calculation of the aggregate ^{235}U spectrum. The black data points are the total ^{235}U spectrum measured at ILL. (adapted from [35, Figure 1])

Present calculations of the ^{92}Rb beta spectrum assume an allowed shape and neglect additional corrections from weak magnetism and other shape factor contributions related to the forbidden-ness of the decay. However, recent studies [20] considering larger weak magnetism corrections and the omission of forbidden shape corrections (the form of which are uncertain for approximately 30% of the flux arising from forbidden beta-decay transitions) suggest a possible additional 4% uncertainty in the predicted antineutrino spectrum shape. If fission product beta spectra show these corrections to be larger than previously thought, their inclusion may eliminate the apparent reactor antineutrino deficit altogether.

1.3 Outline of the Dissertation

This work describes an effort to directly measure the beta spectrum of ^{92}Rb and estimate the contribution of a weak magnetism correction to the spectrum shape.

Chapter 2 provides an overview of the CARIBU facility and the fission products experiment methods, as well as the detector array equipment and layout. A brief description of Argonne National Laboratory's ATLAS User Facility and capabilities of the CARIBU facility is presented. The various components of the detector array experimental apparatus, including the source tape transport and data acquisition systems, are detailed. The chapter concludes with a summary of detector characteristics and a discussion of the detector technology employed for the fission products experiment.

Chapter 3 presents Monte Carlo simulations work used in the design of the detector array and pre-experimental run feasibility studies. The chapter begins with an overview of Geant4, the software toolkit used for those simulations. Experimental design studies using the simulations, as well as the results of an initial investigation of experimental systematic uncertainties are discussed.

Chapter 4 details the use of beta spectrum data from a ^{8}Li ion trap experiment in characterizing the new plastic scintillator detectors described in Chapter 2. A brief discussion of the Beta Paul Trap equipment and its design similarities with the fission products experiment pseudo-trap is provided. Results of studies to evaluate the plastic scintillator detectors' performance using data from the ^{8}Li measurement are presented.

Chapter 5 discusses the analysis of the ^{92}Rb data collected at the fission products detector array. A final simulation study concerning a design change is presented, as well as an updated simulations model of the detector array as configured during the data collection run. The calibration of the plastic scintillator detectors at CARIBU and the analysis of the ^{92}Rb beta

spectrum is described. A preliminary limit on the weak magnetism correction is placed by comparing simulated data using the updated model of the detector array to the measured data at CARIBU. The systematic uncertainties are evaluated.

Finally, Chapter 6 provides a summary of the conclusions presented in Chapter 5 with an outlook and recommendations for continuing study.

Chapter 2

Equipment Overview

This chapter provides an overview of the CARIBU facility and the fission products experimental equipment.

2.1 The Argonne National Laboratory ATLAS User Facility and CARIBU

Located at Argonne National Laboratory's ATLAS user facility (Figure 2.1), CARIBU (*CA*lifornium *R*are *I*sotope *B*reeder *U*pgrade) provides beams of radioactive, neutron-rich nuclei for use in low-energy experiments. Over 500 isotopes are available for delivery to various experimental beamlines via spontaneous fission (spontaneous fission branch of approximately 3.1%) of a 1.7 Ci ^{252}Cf source, originally produced at Oak Ridge National Laboratory's High Flux Isotope Reactor.

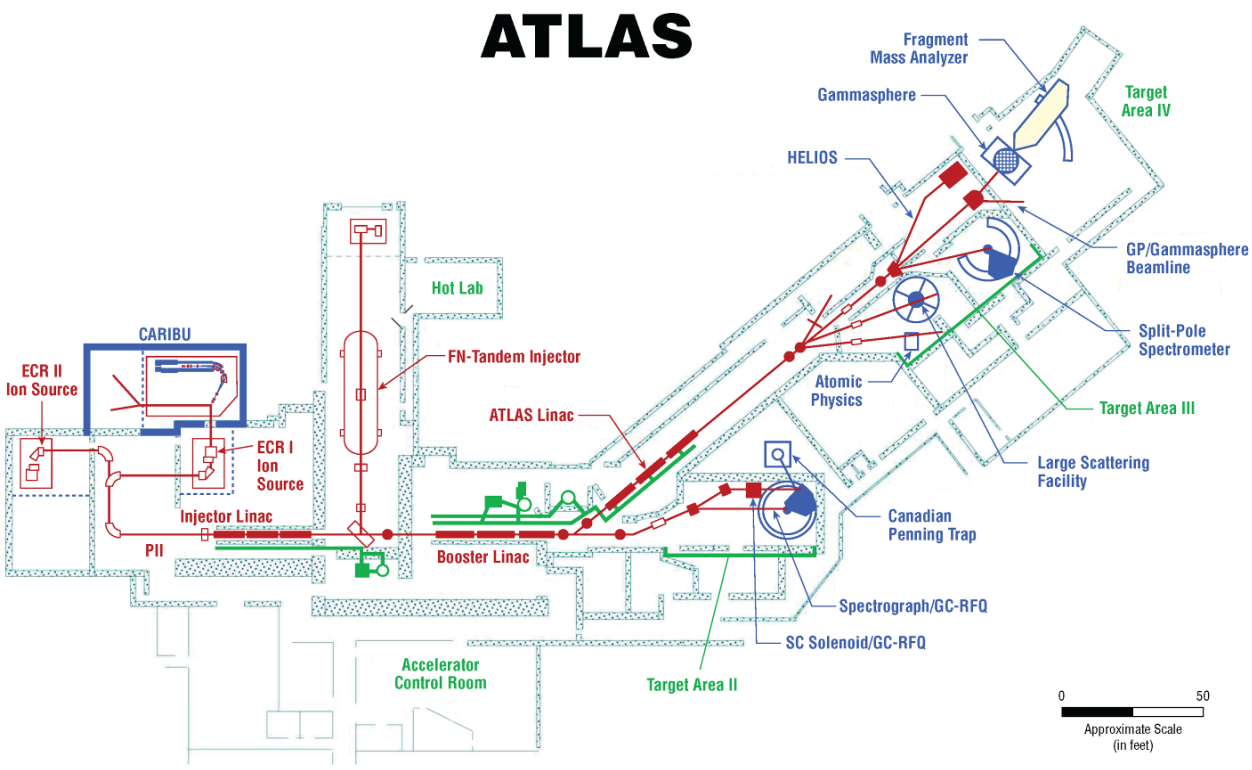

Figure 2.1: Argonne National Laboratory's ATLAS facility.

At CARIBU, the ^{252}Cf source and a high-purity helium gas catcher are positioned within a heavily-shielded cask. The source fission fragments are first thermalized in the gas catcher to inhibit ion recoils. These ions are then extracted from the gas catcher, using DC and RF fields, and transported through two radio-frequency quadrupoles (RFQs). After sufficient cooling in the RFQ section, the ions are accelerated via a 50 kV electrostatic potential to produce a beam. The beam is passed to an isobar separator, capable of mass resolution up to 1:20000, for isotope selection and purification. The isobar separator utilizes an electrostatic doublet and two magnetic dipoles to magnify and deflect the beam. After mass selection, the beam enters a "switchyard," where the ions can be directed to a low-energy experimental area located within the CARIBU hall, or diverted to different regions of the ATLAS facility for re-acceleration, charge breeding, or diagnostics. Beam bunching prior to delivery at the low-energy beamlines allows for pulsing (100 ms interval), increased beam intensity (about 10^5), and energy tuning between 0.1 to 50 keV.

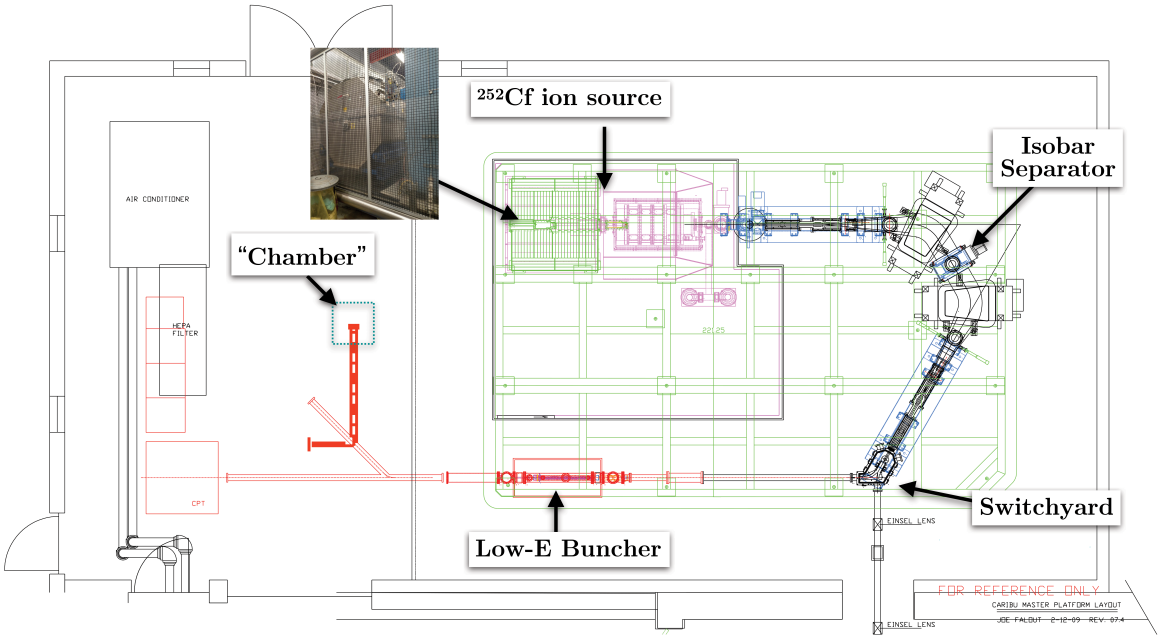

Figure 2.2: The CARIBU experimental hall and source cask [inset]. Adapted from [31].

A simplified layout of the CARIBU experimental hall is shown in Figure 2.2 with "Chamber" denoting the location of the fission products experiment on the 90° low-energy beamline.

CARIBU provides intensities on the order of 10^4 to 10^5 particles/second and can deliver isobarically pure beams of ^{92}Rb (1.0×10^4 ions/second).

2.2 Experimental Apparatus

Four silicon detectors and four plastic scintillator detectors are arranged in a ΔE - E telescope configuration (Figures 2.3 and 2.4). Two High Purity Germanium (HPGe) detectors mounted perpendicularly relative to the ΔE - E telescopes will be used to measure β - γ coincidences in future studies of beta-feeding to excited states.

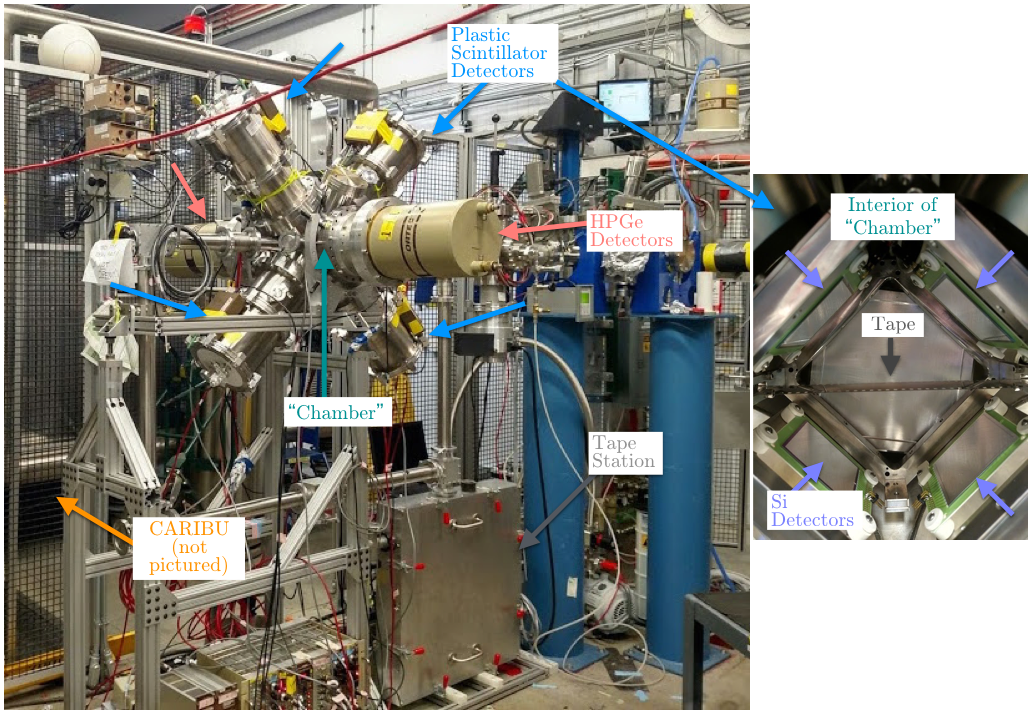

Figure 2.3: The fission products experiment equipment layout (left) and interior of the chamber (right).

2.2.1 The Tape Station

Post-bunching, ions are directed to the low-energy experimental area, where the activity is collected on 35 mm aluminized-mylar tape. The tape passes through the chamber via a tape station and the activity is delivered to the center of the detector array at timed intervals set using a logic controller. The logic controller outputs a TTL signal, passed through a Phillips Scientific Model 7126 logic level translator to the digital data acquisition system front end (DAQ), to record the tape-timing traces for use in offline analysis.

Figure 2.5 shows the general path of the tape (red arrows), as well as the location of the implantation station.

The tape station system, designed and constructed by ANL's ATLAS Physics Division Detector Support Group, is comprised of a "cassette" capable of storing up to 100 m of tape.

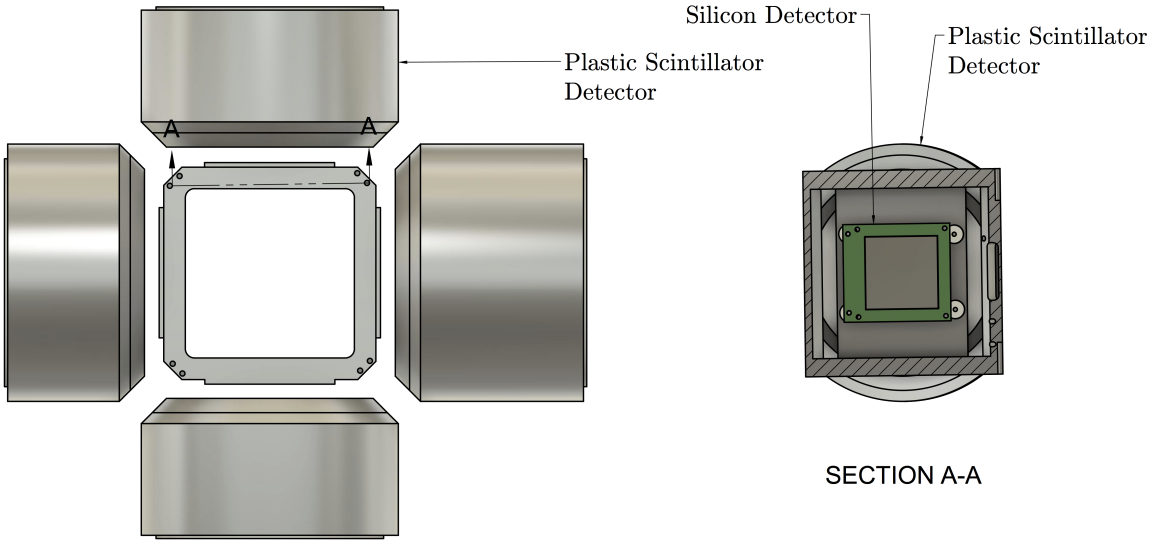

Figure 2.4: A technical drawing illustrating the ΔE - E telescope configuration inside the chamber (left). Section A-A (right) shows a cross-section of the telescope and relative positioning of the silicon detector to the plastic scintillator detector.

A stepper-motor drives a pulley system that feeds the tape through the cassette and moves it upward to an implantation station between the beamline and the chamber. There, the tape pauses to collect the activity. This newly implanted source loops over a spool and continues moving through the chamber, stopping at the center for counting by the detector array. While the tape is stopped, new activity is implanted on a different region of the tape within the box. The tape exits the chamber parallel to the beamline where a spool passes it downward for return to the cassette. The cassette is held at less than 10^{-5} Torr during operation.

2.2.2 Chamber and Pseudo-trap

The stainless steel chamber, connected to the tape pass-through, houses the activity during counting and provides a means to mount the plastic scintillators and HPGe detectors for near-4π coverage. Within the chamber, a stainless steel "pseudo-trap" holds the four silicon

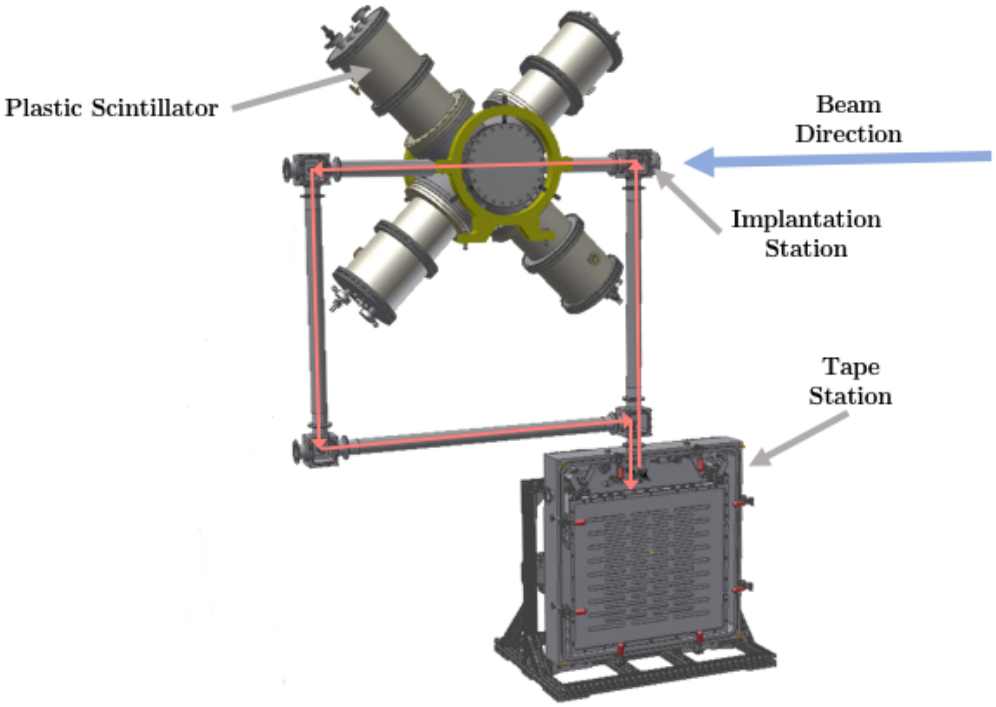

Figure 2.5: The tape station system and chamber.

detectors in front of their respective plastic scintillators to form the ΔE - E telescope. An open view of the interior of the chamber and Pseudo-trap are visible in Figure 2.6.

The pseudo-trap design is modeled after a Beta Paul Trap (BPT) experiment designed to measure α-β-ν angular correlations. Mimicking the general geometry of the BPT allows for high-statistics calibration of the fission products' plastic scintillators. An overview of the Beta Paul Trap design and this calibration work is described further in Chapter 4.

2.2.3 Data Acquisition System (DAQ)

The analog tape station and detector signals are processed and recorded by a digital data aquisition system used at CARIBU for X-Array gamma spectroscopy experiments (originally developed for Gammasphere). The digitizer module is comprised of 10 front-end input channels and a digital signal processor, which buffers the incoming data waveform and digitizes it using a 14-bit/channel analog-to-digital converter (ADC) at a rate of 100 Ms/s.

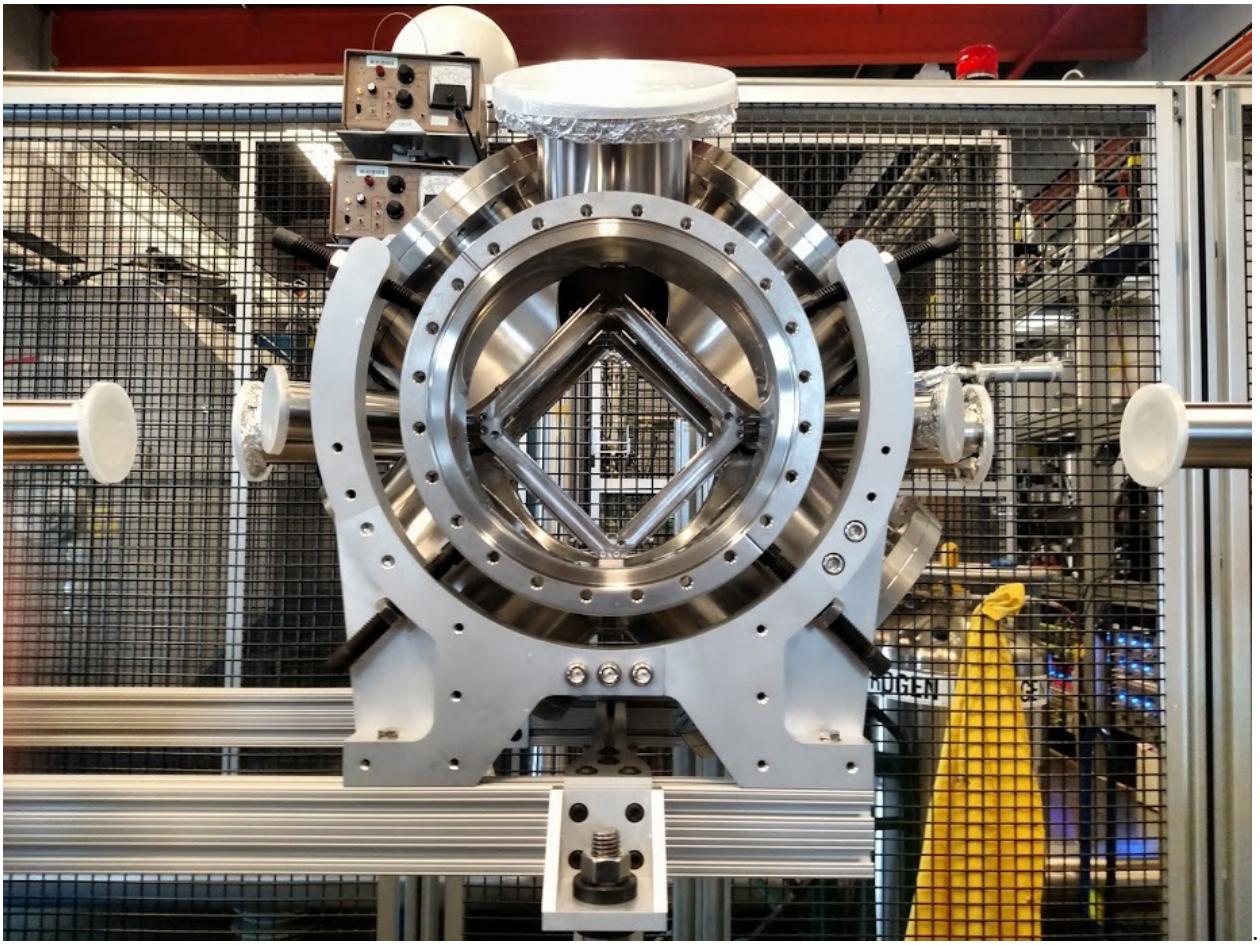

Figure 2.6: The Pseudo-trap and chamber.

All channels are digitized simultaneously in 20 ns intervals at 200 MB/s per channel by a field-programmable gate array (FPGA).

The FPGA logic applies Gaussian filters to a leading edge discrimination (LED) algorithm and compares the digitized input signal to a user-specified threshold. If the signal exceeds the threshold, the discriminator triggers and the buffers are sampled ("pre-rise"). A running sum is kept until the signal falls below the threshold, at which point the buffers are again sampled ("post-rise"). The overall signal pulse height (of course, related to the energy recorded by a detector) is given by the post-rise and pre-rise difference. Full traces of all input signals are recorded (i.e., coincident signals are not required). The digitized data is written to the disk at a rate of approximately 1 MB/s. Further discussion of the DAQ system is outside the scope of this work, but may be found in [17] and [27]. C++ code was developed to sort recorded buffer information into CERN's ROOT framework format for online monitoring and subsequent offline data processing and analysis (see Appendix A).

Figure 2.7 shows the general layout of the detector electronics and DAQ front end.

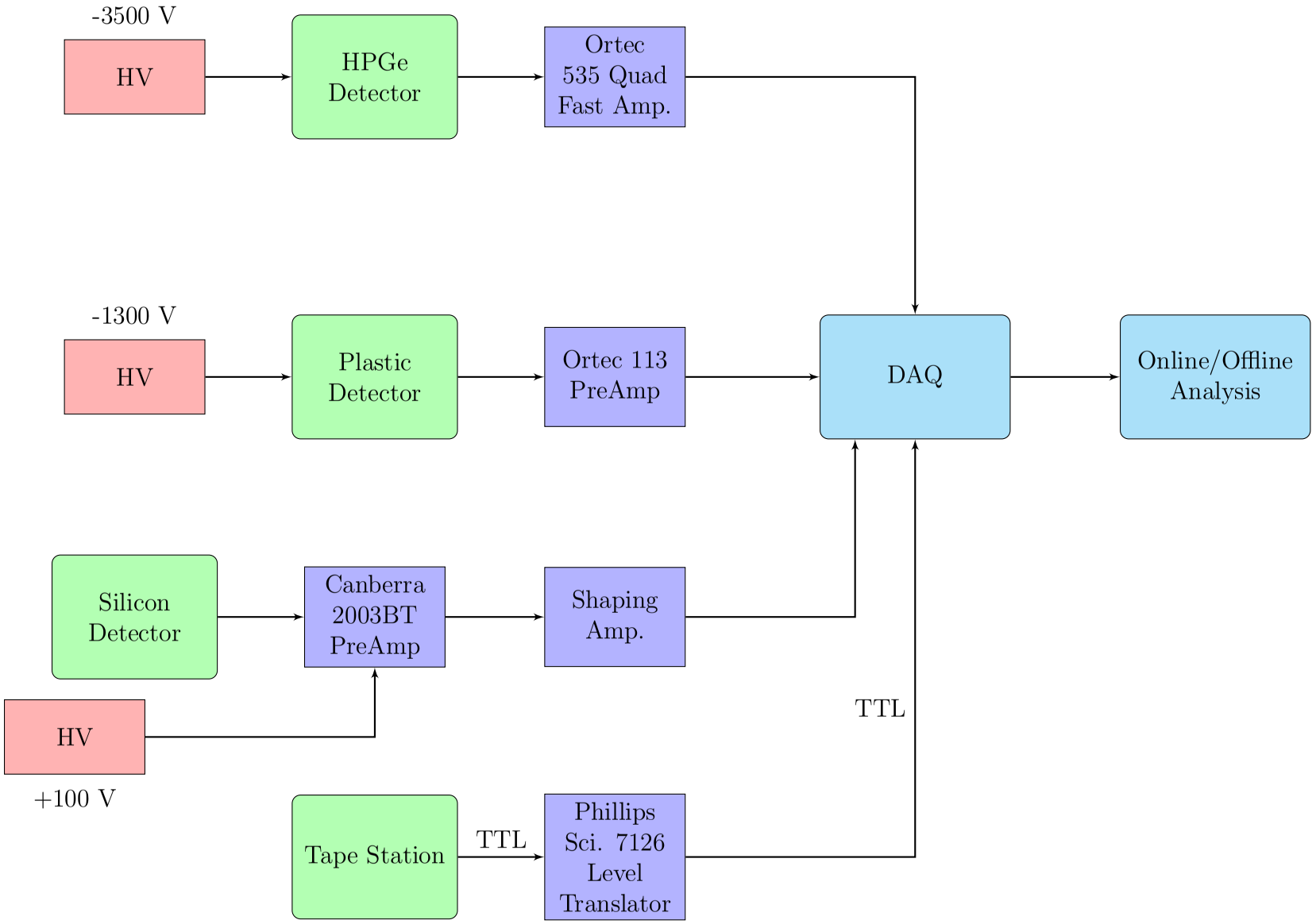

Figure 2.7: A simple block diagram of the detector array electronics.

2.3 Detectors

Particle detectors vary widely in performance, size, cost, and mode of operation. Common varieties used in high energy and nuclear physics experiments include semiconductor (e.g., silicon or germanium) and scintillation detectors[1].

Semiconductor detectors are useful for time-of-flight particle identification and in the case of strip/segmented detectors, can provide valuable event tracking information. However, they are often expensive and their performance may depend heavily on the operating environment (such as ambient temperature).

Scintillation detectors have been a mainstay of high-energy and nuclear physics since the earliest experiments. Scintillators are available in numerous forms (organic and inorganic, gaseous, liquid, or crystal, etc.) and the choice of material depends on the specific application as well as desired performance properties, cost, and required detection parameters.

A photodetector's performance is often described in terms of its *efficiency* (the ratio of the number of events registered by the detector to the number of events incident on the detector), *timing resolution* (describing the detector signal's pulse width, rise time, decay time, and response time), *gain* (in photodectors, the number of collected electrons relative to the generated photoelectrons), and *leakage/dark current* (signals generated in the absence of an event).

For the fission products experiment, four Eljen Technology Model EJ-200 plastic scintillators (Figures 2.8 and 2.9) are positioned behind each silicon detector, situated 90° relative to one another, parallel to the tape. A high-quantum efficiency Hamamatsu R877-100 photomultiplier tube, operated at -1300 V, collects the light. The signal pulse is sent to an Ortec 113 preamp (1000 pF input capacitance) and passed to the DAQ. The scintillation crystal,

[1]This is by no means a comprehensive list, but subsequent discussion of detector technology will be limited to that used in the fission products experiment.

Figure 2.8: An unmounted EJ-200 Plastic Scintillator detector. The scintillating material is located near the bottom of the stainless steel enclosure "can" and the PMT is located near the middle.

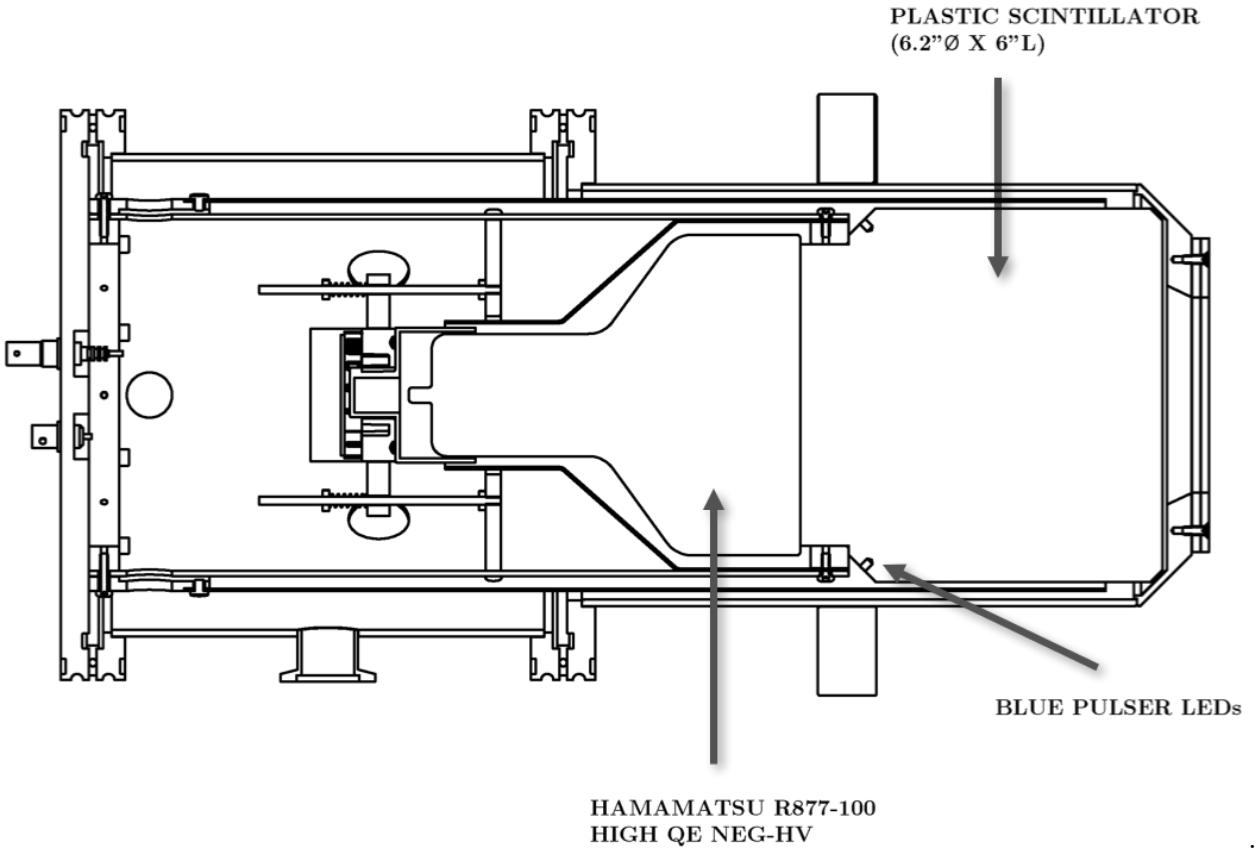

Figure 2.9: A diagram of the interior of an EJ-200 Plastic Scintillator detector used in the fission products experiment.

comprised of a polyvinyltoluene base, is sufficiently large (6.2" R, 6" L) to stop incident betas for a full energy measurement. The EJ-200 design is ideal for the desired detection coverage, in addition to its fast-timing (quoted rise time of less than 1 ns, decay time of $\approx$ 2 ns, and pulse width at FWHM around 2.5 ns) and high light output. In particular, the wavelength of maximum scintillation photon emission (425 nm) is well-matched to the maximal response wavelength of the PMT (420 nm) [15, 14, 18]. Two blue LEDs embedded in the scintillator allow for gain change monitoring over the course of the experiment.

2.3.1 Silicon Detectors

Silicon detectors are a class of semiconductor detector, operated as reverse bias p-n diodes. This junction forms a depletion region comprised of mobile charge carriers. As charged particles pass through the detector, they excite or ionize the electrons on the silicon crystal lattice sites, creating electrons in the semiconductor's conduction band and corresponding holes in the valance band (e-h pairs) proportional to the intensity of the ionizing radiation. If a bias is applied to the detector, these charge carriers will drift through the semiconductor material, in turn inducing a current on the electrical contacts to produce an event signal.

Four Micron Semiconductor [23] (UK) MSX25 model silicon detectors record the ΔE of through-going particles. Each of the silicon detectors are mounted on the pseudo-trap directly in front of a corresponding plastic scintillator. The detectors are comprised of a 0.64 mm-thick, 50.5 mm $\times$ 50.5 mm silicon wafer on a PCB-style SHV ceramic. A +100 V bias is applied on one of four Berg-style pins situated on the edge of the ceramic, with another pin carrying the signal output and 2 others tied to a grounding ring around the silicon wafer (Figure 2.10). The silicon detector signal is passed to the DAQ 2.2.3 through a Canberra 2003BT preamplifier and Ortec 572A amplifier for signal shaping.

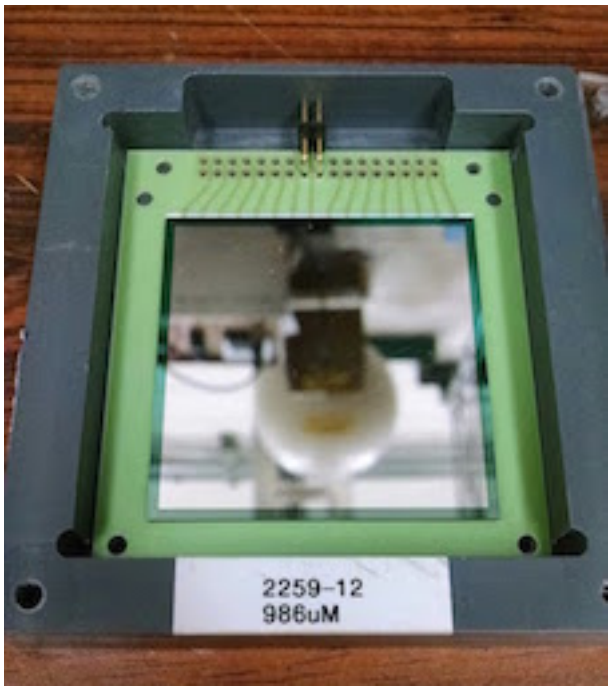

Figure 2.10: An unmounted silicon ΔE detector. The active area is located in the center of the green ceramic mount. The pins for signal output and biasing are visible at the top edge.

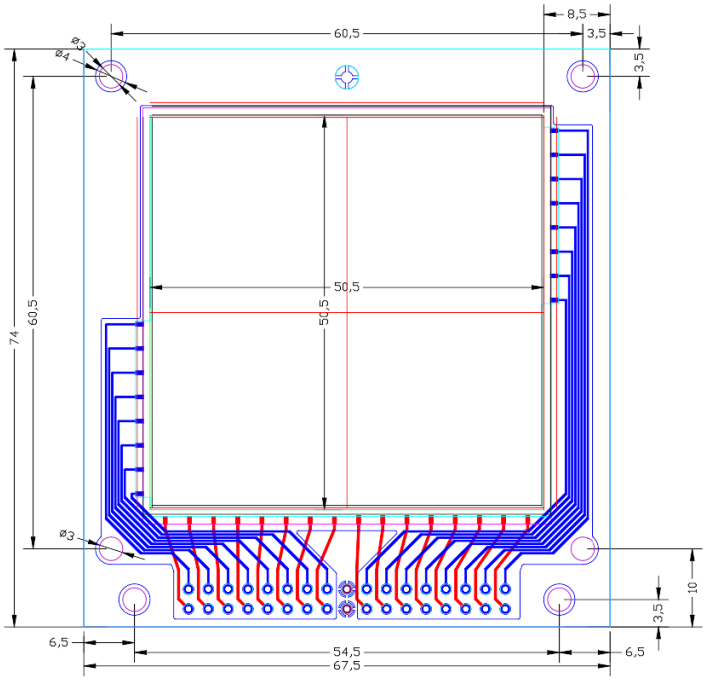

Figure 2.11: A diagram of the silicon detector with dimensions.

2.3.2 High-Purity Germanium Detectors

High-purity Germanium (HPGe) detectors comprise another type of semiconductor detector, mostly used for gamma detection and spectroscopy, and operate on the same general principle as other reverse bias diodes. HPGe's are available in two primary configurations, *planar* or *coaxial* (p or n-type). Typically, for gamma spectroscopy, a coaxial configuration is preferred as it allows for a larger active volume of germanium crystal.

In a p-type coaxial HPGe, a thick, lithium contact is diffused on the outer surface of the cylindrically-shaped germanium crystal to form the n+ contact. A coaxial bulk of the crystal is removed, creating a hollow core and a thin, ion-implanted boron contact is placed on the inner surface, creating the p+ contact. A reverse bias applied to the electrodes generates an electric field and incident gamma photons move valence electrons to the conduction band, creating the e-h pairs that drift through the germanium crystal, producing a signal pulse proportional to the incident gamma ray's energy for read-out to the front-end electronics. The susceptibility of HPGe detectors to signal obscuring, thermally-induced leakage current requires they be cooled to LN_2 temperature via contact with insulated dewars that must be periodically refilled for the duration of the detector's operation.

For the fission products experiment, Ortec Model GEM80 ("HPGe 1") and Ortec Model GEM140 ("HPGe 2") HPGe detectors (Figure 2.12), previously used in other ATLAS-based gamma spectroscopy experiments (Gammasphere and X-ARRAY), to be employed in future beta-feeding studies, are mounted on the chamber perpendicular to the ΔE - E telescopes. The HPGe detector signals are passed to an Ortec 535 Fast Amplifier and sent to the DAQ.

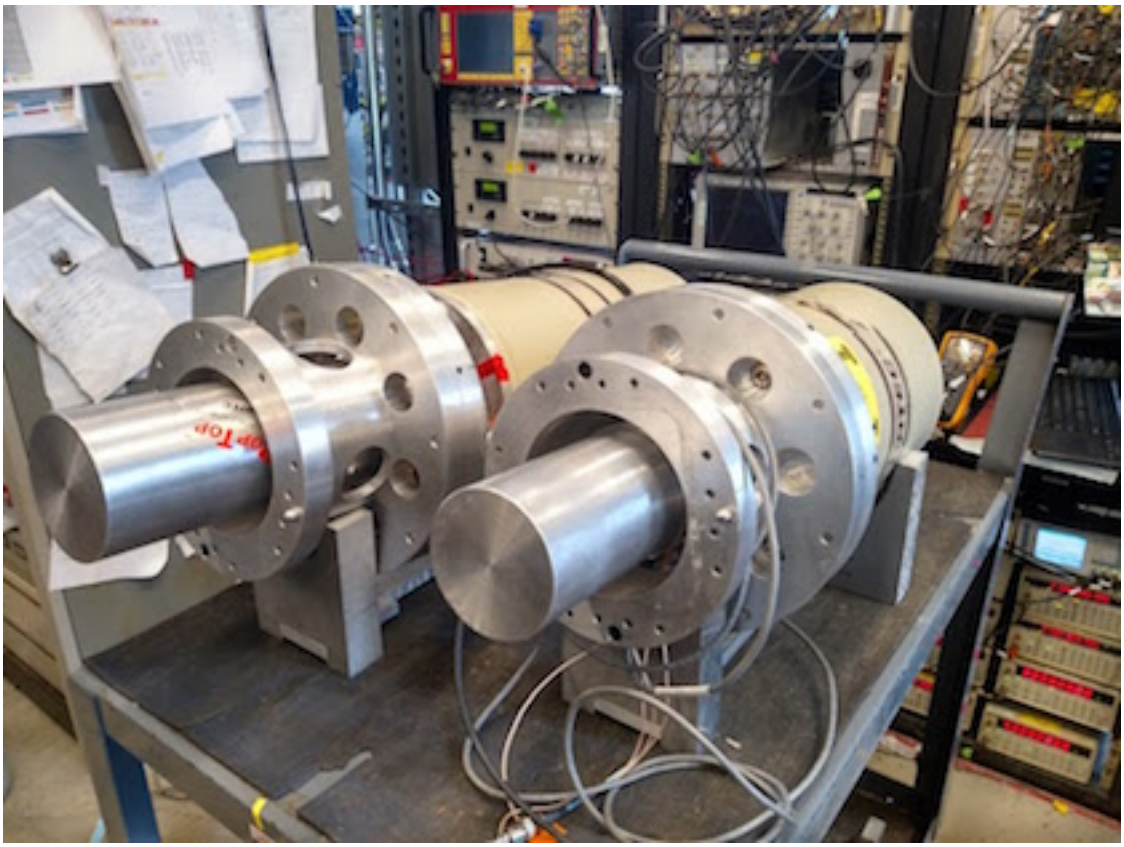

Figure 2.12: The unmounted Ortec GEM80 (right) and Ortec GEM140 (left) HPGe detectors.

2.3.3 Plastic Scintillation Detectors

Regardless of their specific design, all scintillation detectors operate on the same basic principle. In a scintillator, incident ionizing radiation excites the scintillation medium. The scintillator material absorbs the energy deposited by the particle and re-emits it via luminescent processes as visible radiation. A photodetector, such as a photodiode (i.e., silicon photomultipliers, multipixel photon counters, pixelized photodetectors) or photomultiplier tube (PMT) collects the light and converts it to an electric signal proportional to the initial energy deposited.

One class of organic scintillators, plastic, are characterized by fast response time, low noise, large area coverage, and relatively high light output, making them ideal for time-of-flight and direct energy measurements. In a plastic scintillator, an organic compound is dissolved in a solvent base (commonly styrene or polyvinyltoluene) and polymerized to create a solid, plastic bulk for subsequent machining into a shape suitable for the desired detector geometry.

Photomultiplier tubes are commonly employed in radiation detection and spectroscopy experiments. In a PMT, photons created via the scintillation mechanism are absorbed by a photocathode-type semiconductor, converting the visible light into low-energy electrons. Generally, the number of low-energy electrons through this photoemission is much too small for use as an electric output signal, directly. In order to create a usable pulse, the electrons first pass through a vacuum tube, accelerated by electric fields induced by the application of high voltage to the detector electrodes. The accelerated electrons are focused and deposit their energy on dynodes, leading to the emission of multiple so-called "secondary" electrons, which in turn, create more secondary electrons as they cascade over several dynode stages. The creation of these secondary electrons effectively multiplies the signal corresponding to the original incident signal electron produced in the initial photoemission stage (hence,

photo*multiplier* tube). Finally, the secondary electrons are collected at the end of the tube for counting and output as a signal pulse [26].

Chapter 3

Monte Carlo Simulations for Fission Product Experiment Feasibility and Sensitivity Studies

Both the ^{8}Li (Chapter 4) and fission products experiments utilize simulations to ensure they will meet the design goals required for each study and understanding the operating parameters of the equipment and later, in the post-run analysis of the collected data. Geant4 has been a mainstay for simulation of particle-matter interactions in the high energy, nuclear, and space science fields for decades [8, 5, 9].

The following sections describe the simulations development, workflow, and pre-run feasibility studies performed in preparation for the CARIBU fission products experiment.

3.1 Simulations and Event Generation

Comprehensive, detailed simulations are essential for any comparison of experimentally measured decay spectra to existing models (standard or otherwise) used in theoretical descriptions of the spectra and decay behavior. As such, it is important to develop simulations that accurately describe the actual experimental environment, including detector geometries, fundamental physical processes, and interactions. For instance, a poor understanding of scattering effects within the detector array can obscure legitimate physics or introduce substantial error in the analysis. Preliminary simulations can provide insight as to the feasibility of an experiment, help identify problems during the design of an experiment, and evaluate the impact of later design changes on experimental sensitivity. This section provides an overview of the Geant4 simulations toolkit and describes the event generation framework.

3.1.1 A Brief Overview of the Geant4 Simulations Toolkit

At its core, Geant4 simulations are built from specified geometries, materials, and "sensitive" volumes to model detectors and ancillary equipment, as well as event generation to describe the physical processes and interactions of interest by tracking particle propagation, and writing of the simulated data (often as ROOT files, though other formats are not uncommon).

A detector in Geant4 is built of volumes specified by various geometric parameters, including size and shape. These parameters are grouped into a *logical volume* class and combined with information of relative position within the World of the simulated experiment, comprises a *physical volume*. Physical volumes assigned a material are termed *solids*. The Geant4 framework maintains an extensive library of commonly-used materials, like stainless steel or plastics, though more exotic, user-defined compounds may also be constructed by specifying a material's chemical composition. Solids may be combined via Boolean addition or sub-

traction of simple shapes (like spheres or Platonic solids) to create non-standard, composite volumes. Many experiments have complicated geometries that make such a definition impractical. This difficulty may be somewhat circumvented by first modeling the geometry in external design and drafting software and then importing it to the larger Geant4 simulation in a framework-supported format.

A Geant4 event is defined as the full simulation of a particle, including its propagation through the World and subsequent interactions with the defined physical volumes. The behavior of an event particle is dictated by choice of runtime parameters (like geometries), initial conditions, and simulation physics. The physics is contained within a physics list, or a set of models to describe various processes like scattering, hadronic, or electromagnetic interactions. The choice of physics list depends on the level of detail necessary to model an experiment's interactions of interest. A nuclear physics experiment may be inclined to employ a physics list focused on low-energy models of radioactive decay and scattering processes, while a collider experiment might be better served by a physics list designed for TeV-scale hadronic interactions. Ultimately, choice of a physics list is a compromise between computation time (simulations of complicated experiments with comprehensive, high-precision lists and long-tracking of a particle may take weeks and require expensive, state-of-the-art computing clusters) and the desired level of accuracy. Regardless, careful consideration must be given in selecting a list and the limitations of certain models taken into account when specifying error. The simulations in this work use the *G4EmStandardPhysics_option4* physics list, which is a collection of the most accurate physics models for low-energy electron transport. For electrons below 100 MeV, multiple scattering is modeled by the Goudsmit-Saunderson theory, as opposed to the default Urban multi-scattering model [39]. A model for multiple scattering in Geant4 favored by high-energy experiments. An in-depth discussion of these models and implimentation in the Geant4 framework is beyond the scope of this dissertation, but may be found in [25].

A Geant4 *run* is a series of events following the generation of a primary particle (a radioactive decay, a fundamental particle launched "gun-style" at a detector, etc.) and mimics a real-world experimental run. An event is built from a *track* describing the propagation of the initial particle and any secondary particles generated through physical processes or interactions. A particle's instantaneous properties (such as momentum, event identification number, or energy), is held in a *step* that is evaluated periodically and used to update the track information used in the particle's subsequent propagation. An event is terminated when the particle stops propagating within the World volume, or when it meets a user-specified criteria (like hitting a particular volume). A hit is the interaction of a particle with a sensitive detector volume and provides the track/step information for processing or data writing.

3.1.2 Event Generation

In this work, simulated events were generated by either utilizing Geant4's built-in radioactive decay module (RDM) or internally-developed beta decay event generation code (hereafter abbreviated as "BD code"). The radioactive decay module was used in the detector characterization studies using standard test sources (and later, calibrations), while the events from the beta decay of ^{8}Li and the fission products experiment isotopes were generated using the BD code.

Beginning with Geant4 v. 2 (released 2015), an event generator for radioactive decays has come standard with all releases of the Geant4 toolkit. The RDM generates radioactive decay events using evaluated Evaluated Nuclear Structure Data Files (ENSDF) from the National Nuclear Data Center [41]. "Direct" secondary particle emissions (alpha particles, beta particles, or neutrinos) are generated via a nuclear process class, while the subsequent production of particles from atomic de-excitations or florescence emissions and are defined

by their own classes. Together these processes form a data-driven, comprehensive model of radioactive decay.

While useful in direct comparisons of library data to measured spectra, the RDM lacks the capability to factor in user-introduced changes to established spectral models (for instance, the addition of a shape factor or weak magnetism correction) in its event generation. To allow for comparison to non-standard models and probe for spectral distortions, simulated beta decay events were generated using the BD code. The BD code was adapted from code originally developed for earlier correlation studies [33]. The current iteration of the BD code applies various corrections and correlation terms and descriptions for decays to excited states, all of which are user-editable. Decay events are generated using a so-called rejection method whereby unit momentum vectors for beta particles and neutrinos (and additionally alpha particles in the case of ^{8}Li) are randomly selected and the beta particle's energy is set by choosing a random value between 0 and the endpoint energy. The energy of the neutrino is calculated using energy and momentum conservation. The likelihood of that particular event is determined by comparing the amplitude of the phase space for those parameters to the amplitude of that event taken over the entire parameter phase space. An event lying outside that phase space probability is rejected as non-physical. These parameters are then applied to the coordinates within the Beta Paul Trap/pseudo-trap corresponding to the physical location of the decay vertex.

In the case of the Beta Paul Trap, the position of ions at the center of the trap may be approximated by a three dimensional Gaussian distribution and the decay vertex is assigned to a randomly-selected point on the distribution, with parameters informed by effects on the ion cloud shape arising from real experimental conditions. This crude model of ion placement near the center neglects any influence of time-dependence on decay position introduced by the (nearly) harmonic potential generated by the trap electrodes. The impact of such a correction has been shown to be well-within attainable experimental precision [36] and thus,

for our larger purpose, may be considered sufficient. In the case of the fission chamber experiment's pseudo-trap, a decay vertex is similarly assigned. As the activity is directly deposited on the tape, no "smearing" or position characteristic of trapped ions is considered in decay vertex placement.

These parameters (momentum, energy, and decay vertex position) are output as a macro file in human-readable format (.txt) and flown as input to the Geant4 simulation. Each event generated is defined by a series of Geant4 particle gun commands specifying the particle type, energy, direction, and position:

```
# 1
/gun/particle e-
/gun/energy 3.832404 MeV
/gun/direction -2.143894 -2.464449 -7.783139
/gun/position 0.343308 0.886674 -0.164622 mm
/run/beamOn 1
# 2
/gun/particle e-
/gun/energy 4.970431 MeV
/gun/direction 5.888187 8.194468 -3.499442
/gun/position -1.406385 -3.422694 -1.604184 mm
/run/beamOn 1

...
```

3.2 Preliminary Detector Array Modeling and Design

As mentioned briefly in Chapter 2, the fission products' detector array design was motivated by the general geometry of the Argonne Beta-Decay Paul Trap. The particulars of the Beta Paul Trap and its use in pre-run detector calibration is discussed in Chapter 4. However, the differences between the Beta Paul Trap and pseudo-trap (for example, the inclusion of the aluminized mylar tape in latter), require an evaluation of systematic effects introduced

by variation in the detector array's design if the Beta Paul Trap is to be used in initial calibration. Additionally, as the fission products array was not used in prior experiments, it was useful to study the impact of any changes to the pseudo-trap geometry, as inevitable technical difficulties emerging during the array's manufacturing, construction, and deployment would require some deviation from the original design.

Initially, the pseudo-trap was modeled as a simplified Beta Paul Trap (BPT) design (Figure 3.1). Small changes from the design were imposed to better reflect the anticipated final pseudo-trap geometry. The plastic scintillator bulk, housing, and window materials were modeled by generating a composite solid using standard Geant4 volumes and placed against the sides of the trap, directly behind the Double Sided Strip Detectors (DSSDs). The DSSDs were changed to an unsegmented, planar design. However, the general DSSD shape, trap frame dimensions, and relative positioning of the geometric elements remained unchanged from the BPT design. A thin strip for the aluminized mylar source tape was added across two opposite electrodes to represent their new roll as a passive "tape collimator" system. Figure 3.2 shows a Geant4 rendering of this altered geometry.

3.2.1 Design Finalization and Geometry Change Studies

If removing different elements of the BPT significantly impacts beta spectra measurements, the detectors will not be properly calibrated for use in the new pseudo-trap housing. To study these systematic effects, the BPT design shown in Figure 3.1, or "default geometry" was altered in various ways to mimic the conditions of the new housing. Two kinds of input beta decay files were generated by the BD code. One input file assumed the beta spectrum as having a purely allowed shape without any corrections arising from higher order terms. The second input instead used a phase space taking the form of a purely weak magnetism term. The resulting Geant4 output spectra are shown in Figure 3.3.

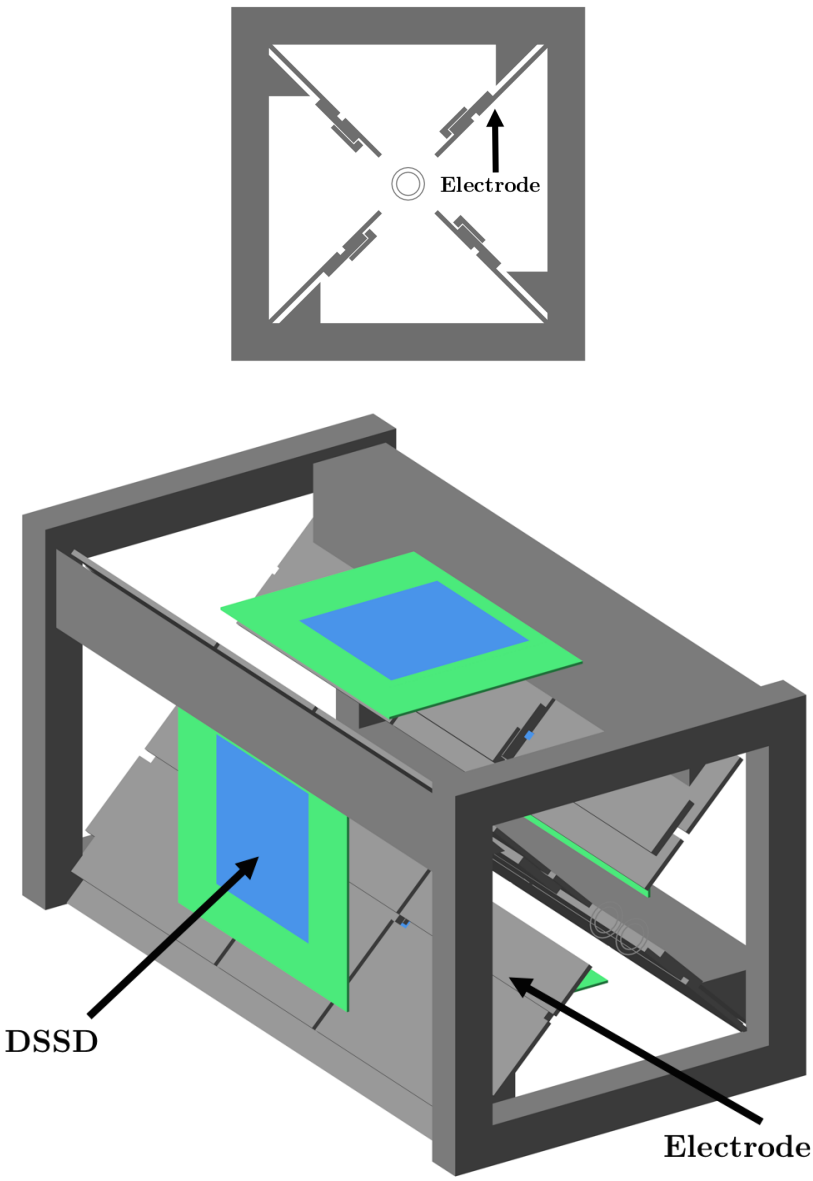

Figure 3.1: The initial Geant4 model of the Beta Paul Trap (the strip segmentation of the Double Sided Strip Detectors is not shown)

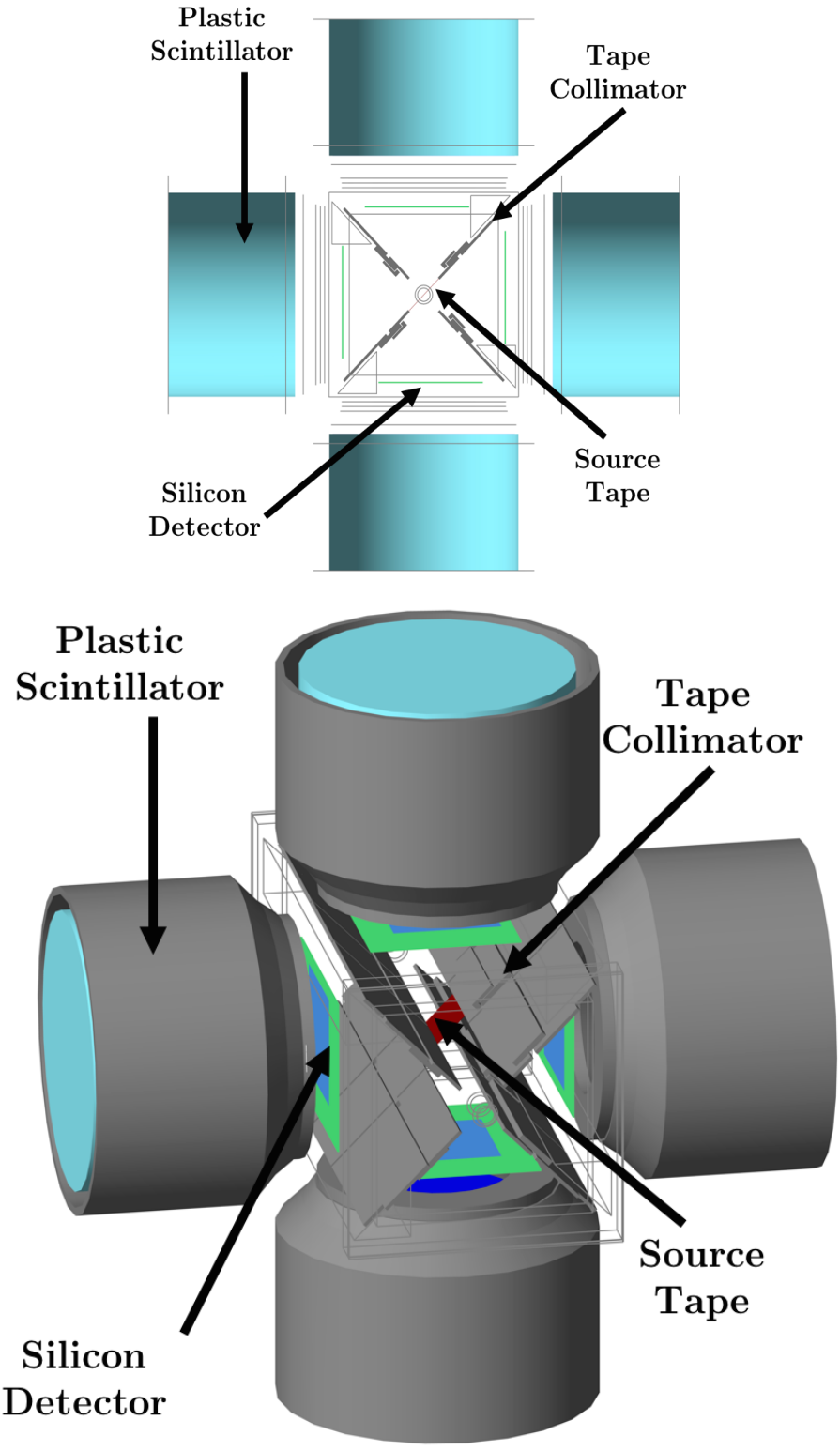

Figure 3.2: The preliminary Geant4 model of the fission products experiment (*v.1*)

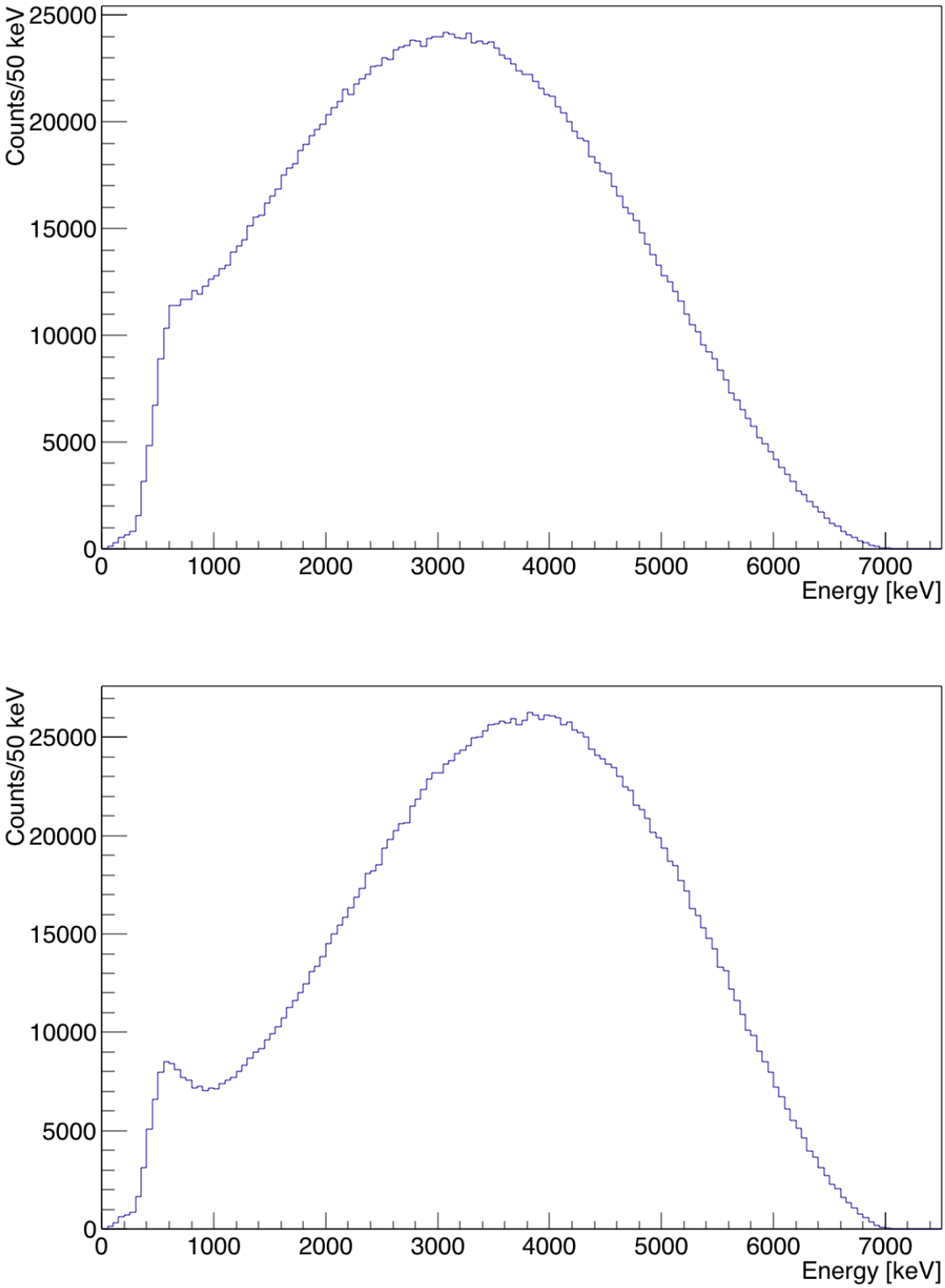

Figure 3.3: Simulated ^{96}Y spectra assuming purely allowed (top) and purely weak magnetism (bottom) shapes.

While several modifications were considered, two scenarios are of particular importance: the addition of the aluminized mylar source tape (otherwise absent in the "default" geometry) and changes in the location of the deposited source on the tape (to account for possible small fluctuations in the CARIBU beam's alignment during the run or varation in calibration source placement). In the first case, the tape was added as a new volume to the Geant4 geometry. The second implements the transport tape volume in addition to shifting the source decay vertex by 5 mm in all directions along the tape within the BD code.

Location shifts in the

1. +YZ direction (closer to the top right electrode)
2. -YZ direction (closer to the bottom left electrode)
3. +X direction
4. -X direction

were considered.

All spectra were convolved with a Gaussian detector response model:

$$\begin{aligned} k &= \text{Resolution scaling factor} \\ \text{Energy}[bin_i] &= \frac{bw}{2} + bin_i \times bw \\ \sigma[bin_i] &= k \times \sqrt{\text{Energy}[bin_i]} \\ \text{Counts}_{\,conv.}\,[bin_j] &= \frac{\text{Counts}_{\,unconv.}\,[bin_i] \times bw}{\sqrt{2\pi\sigma^2[bin_i]}\, e^{\frac{1}{2}\left(\frac{\text{Energy}[bin_j] \text{ - } \text{Energy}[bin_i]}{\sigma[bin_i]}\right)^2}} \end{aligned} \tag{3.1}$$

where the resolution scaling factor, k, was set near values close to that reported in mass-8 α-β-ν angular correlation experiments using similar detectors [38]. As the ^{8}Li experiment described in Chapter 4 will be used for initial calibrations and simulations validation, this choice of k provides consistency in analysis between this particular study and the work described in subsequent chapters.

The default geometry spectrum is fit to the spectra from the changed geometries/source positions. The fit function is chosen to be a linear combination of the convolved default allowed and weak magnetism spectra to assess the impact of the design changes on the weak magnetism contribution in particular. The parameters p_0 and p_1 measure the allowed and weak spectrum contributions to the fit, respectively.

Figure 3.4 shows the fit when the transport tape is included in the geometry and normalized residuals. The small $p_1 < 0$ is attributable to the lower energy deposited in the detectors from interactions with the transport tape and higher average energies of a purely weak magnetism spectrum due to the modification of the shape factor by $1 + \delta_{\mathrm{WM}}$.

The fit yields a $\chi^2 \approx 0.778$ and the normalized residuals are within 5% over the majority of the energy region (200 keV - 5.8 MeV) and less than 2% between approximately 1 MeV - 5.2 MeV.

Figure 3.5 shows the effect of source position relative to the electrodes ("up" or "down" the tape) and gives insight into the possible effects of scattering on the spectral shape. The p_1 contribution is comparable with that in Figure 3.4, varying by less than .01 for both translation directions. Again, the normalized residuals stay between $\pm$ 5% for most of the spectrum, and the behavior at the high energy tail is similar to the case with the source activity centered on the transport tape. Below $\approx$ 200 keV, the disagreement is less gradual than in Figure 3.4, suggesting scattering effects from the electrodes will have some (small) effect on the strength of the weak magnetism term in the lower energy region.

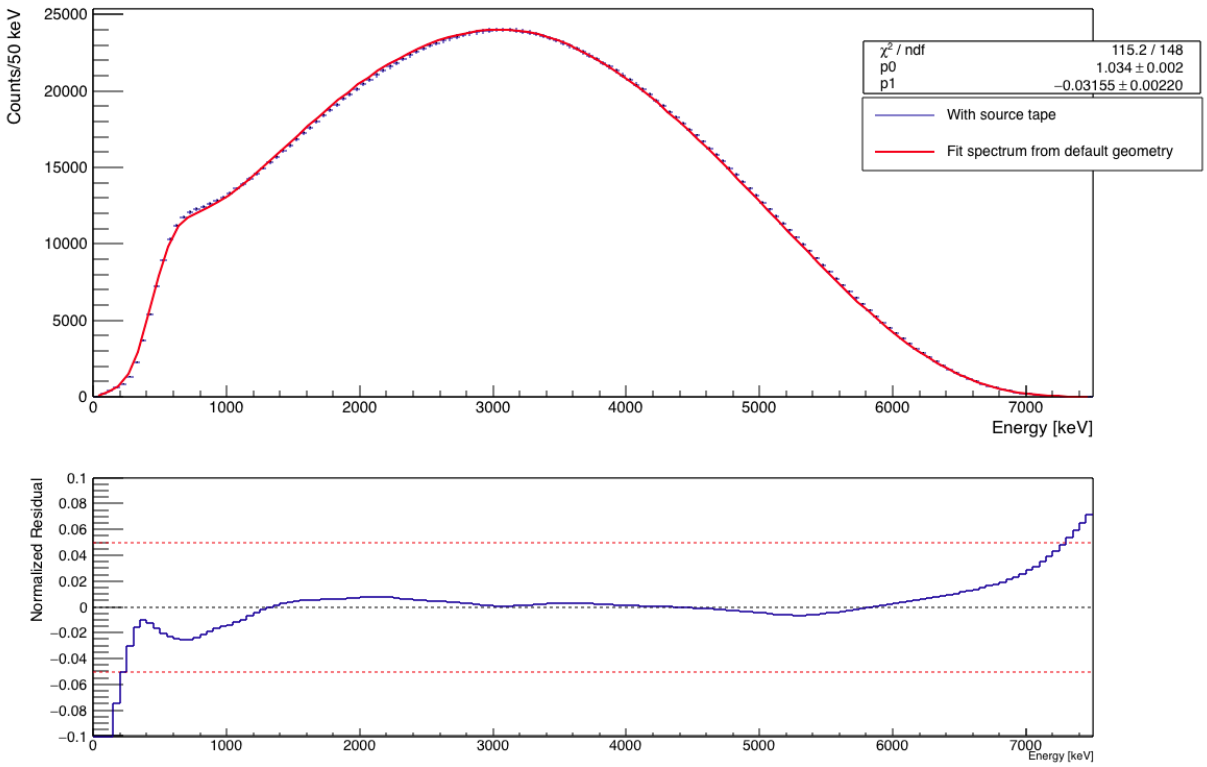

Figure 3.4: Simulated ^{96}Y spectra with the inclusion of the transport tape in the default geometry and the residual. The red line is the fit from the geometry without the transport tape, while the blue represents the spectrum without the tape.

The source position translations in Figure 3.6 demonstrate the impact of horizontal beam displacement at the source implantation station due to instability or slight misalignment. Here, the scattering cross section from the electrodes varies much less from the default case, but the amount by which the activity is "off axis" relative to the telescopes is greater as compared to Figure 3.5. Similar high energy behavior is observed between this scenario and the case in Figure 3.5 and the fit is in agreement with the default geometry within 5% over the 200 keV to 7.2 MeV energy range as previously. The differences at low energies also appear here, but is less precipitous than in Figure 3.5. The magnitude of the weak magnetism contribution varies by $\sigma_{\text{misalign.}} = 0.0014$ between changes.

3.3 Discussion and Conclusion

Initial Geant4 simulations indicate little variation in detector response between design changes from the default geometry, such as the addition of the transport tape, with less than 5% variation near the energy region of the anomalous reactor antineutrino shoulder. The results of Figure 3.4 show resilience to these changes over the 1-7 MeV region of interest, as evidenced by the magnitude of the p_1 fit parameter, which remains small compared to the p_0 fit parameter (representing the contribution from the allowed spectral shape).

Extreme imprecision in source placement at the implantation station was also considered (5 mm is larger than the typical beam spot variation at CARIBU, or anticipated shift in calibration source placement). Design changes and variation in source position do not overly obscure distortions of the beta spectra introduced by the weak magnetism term (i.e., the variation in the p_1 fit parameter shown in Figures 3.5 and 3.6). Uncertainty in the correction arising from source misalignment is set at $\sigma_{\text{misalign.}} = 0.0014$, which will be included in the final error budget of the weak magnetism correction estimate given in Chapter 5.

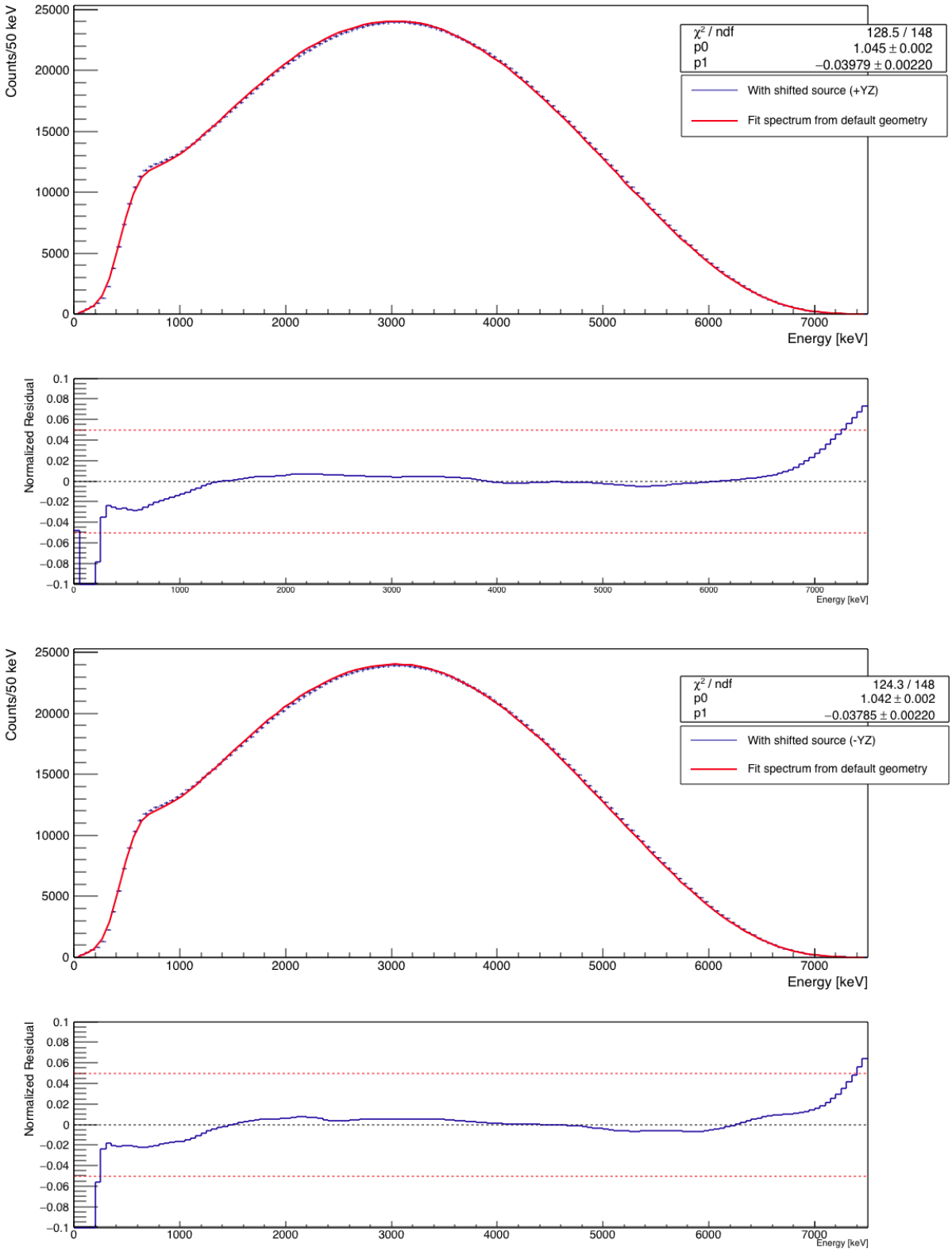

Figure 3.5: Simulated ^{96}Y spectra with the inclusion of the transport tape and source translations in +YZ (top) and -YZ (bottom) and their residuals. The red line is the fit from the default location, while the blue represents the spectrum with the shifted source.

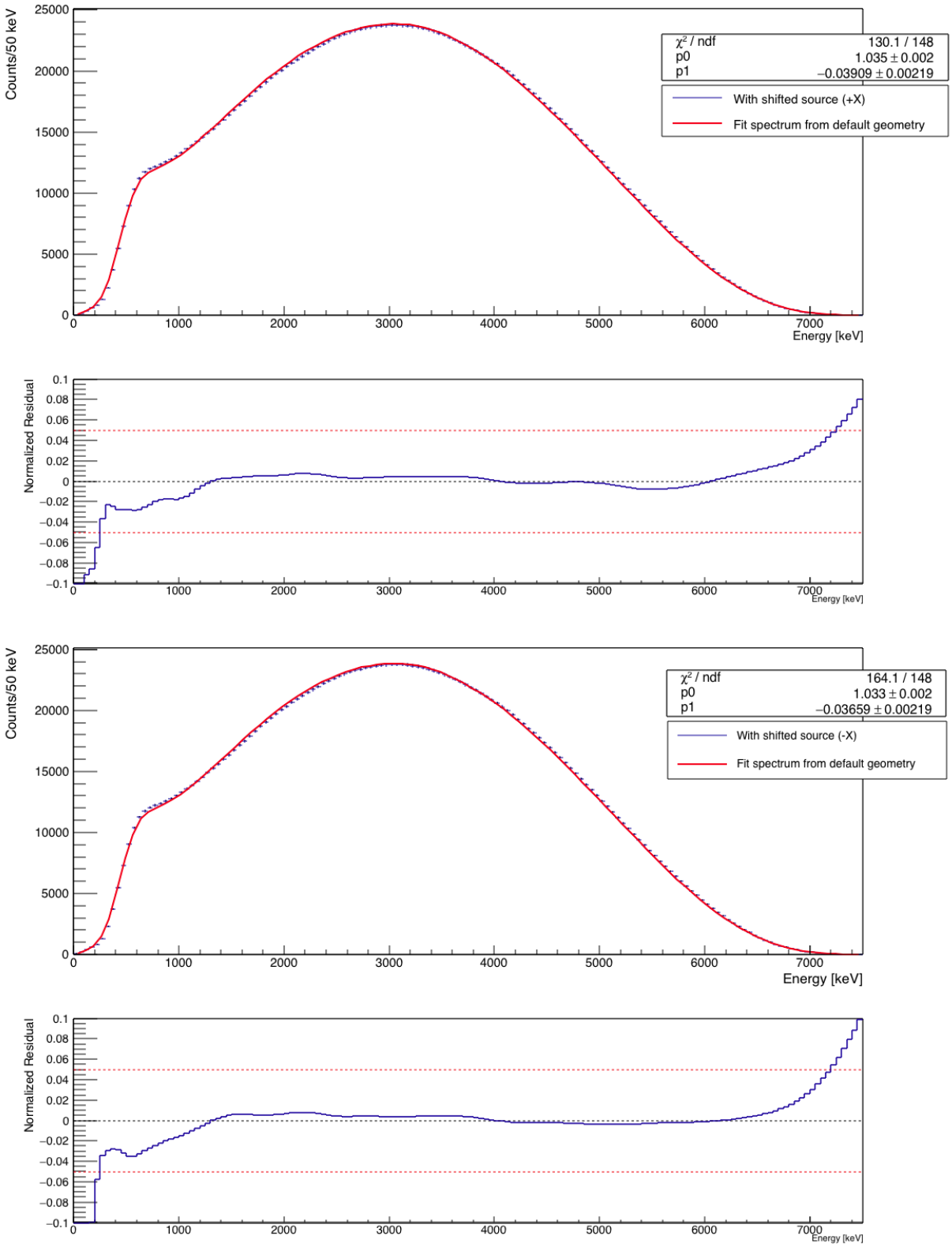

Figure 3.6: Simulated ^{96}Y spectra with the inclusion of the transport tape and source translations in +X (top) and -X (bottom) and their residuals. The red line is the fit from the default location, while the blue represents the spectrum with the shifted source.

Chapter 4

Detector Characterization and Calibration

As mentioned briefly in Chapter 2, the fission products' detector array design was motivated by the general geometry of an ion trap at the ATLAS facility. These design similarities aided in the validation of the Monte Carlo simulations used in the analysis described in Chapter 5, as well as preliminary characterization and calibration of the new plastic scintillator detectors using data from high-statistics ^{8}Li beta decay measurements.

4.1 Electroweak Interaction Studies at ATLAS

4.1.1 The Argonne Beta-Decay Paul Trap

At ANL, the ATLAS Beta-Decay Paul Trap (BPT) has provided a novel means to test the electroweak interaction and probe nuclear structure through ^{8}Li α-β-ν angular correlation measurements [37] and β-delayed neutron spectroscopy [32].

For years, ion traps have been a staple of mass spectrometry and basic physics measurements of isotopic properties. Ion traps utilize electric fields, magnetic fields, or a combination thereof, to hold gaseous ions within a potential well. The BPT falls into a class of ion traps known as quadrupole ion traps. Specifically, the BPT is a kind of linear Paul trap, so named after its inventor, Wolfgang Paul (not to be confused with prolific quantum mechanic Wolfgang Pauli). In a Paul trap, static DC and oscillatory RF electric fields are used to confine the ions axially and radially, respectively. Four hyperbolic electrode "rods" generate a quadrupole vector field. An oscillatory RF electric field potential is applied to the electrodes for radial confinement of the ions at the center of the trap, while a static DC potential is applied to lenses at either end of trap to confine the ions axially [29].

The BPT design deviates from the typical Paul trap geometry and utilizes four plate-shaped electrodes instead of the usual hyperbolic electrodes. This difference allows for good detection coverage of the trap center and permits several kinds of detector geometries, making it quite versatile and easily adaptable for use in a variety of experiments. The development and design particulars of the BPT may be found in [36]. Figure 4.1 shows an external views of the BPT prior to its installation and a simplified diagram of its electrode configuration (Figure 4.2).

4.1.2 The ^{8}Li Beta-Decay Paul Trap Experiment

At ANL, the BPT is utilized for precision α-β-ν angular correlation coefficient measurements to search for weak interaction tensor couplings beyond what is predicted by the Standard Model. ^{8}Li ($t_{1/2}$ = 0.84 s, Q $\approx$ 16 MeV), a Gamow-Teller decay, is particularly useful in these types of studies. In ^{8}Li, the 2^+ ground state ion decays to a ^{8}Be 2^+ excited state. Immediately after ($\approx 10^{-21}$), the ^{8}Be daughter breaks up into two α particles, emitted 180° from each other in the rest frame of the daughter. The nuclear recoil information, along

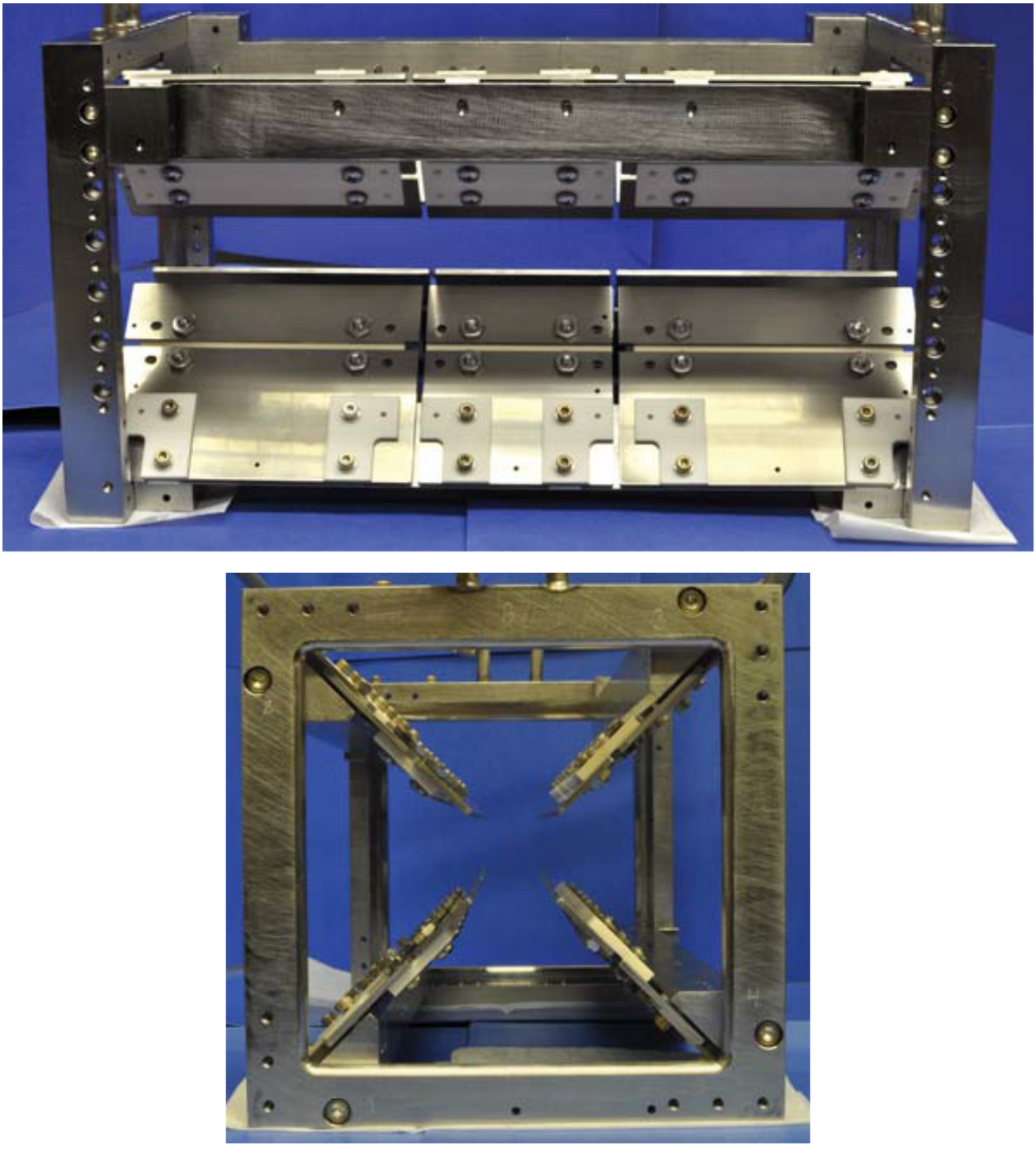

Figure 4.1: The Argonne Beta-Decay Paul trap prior to installation at ATLAS (top) and its cross-section (bottom)

with the detected kinematics of the β can be used to calculate the β-ν correlation coefficient and ascertain values for the associated coupling constants. Improved experimental limits

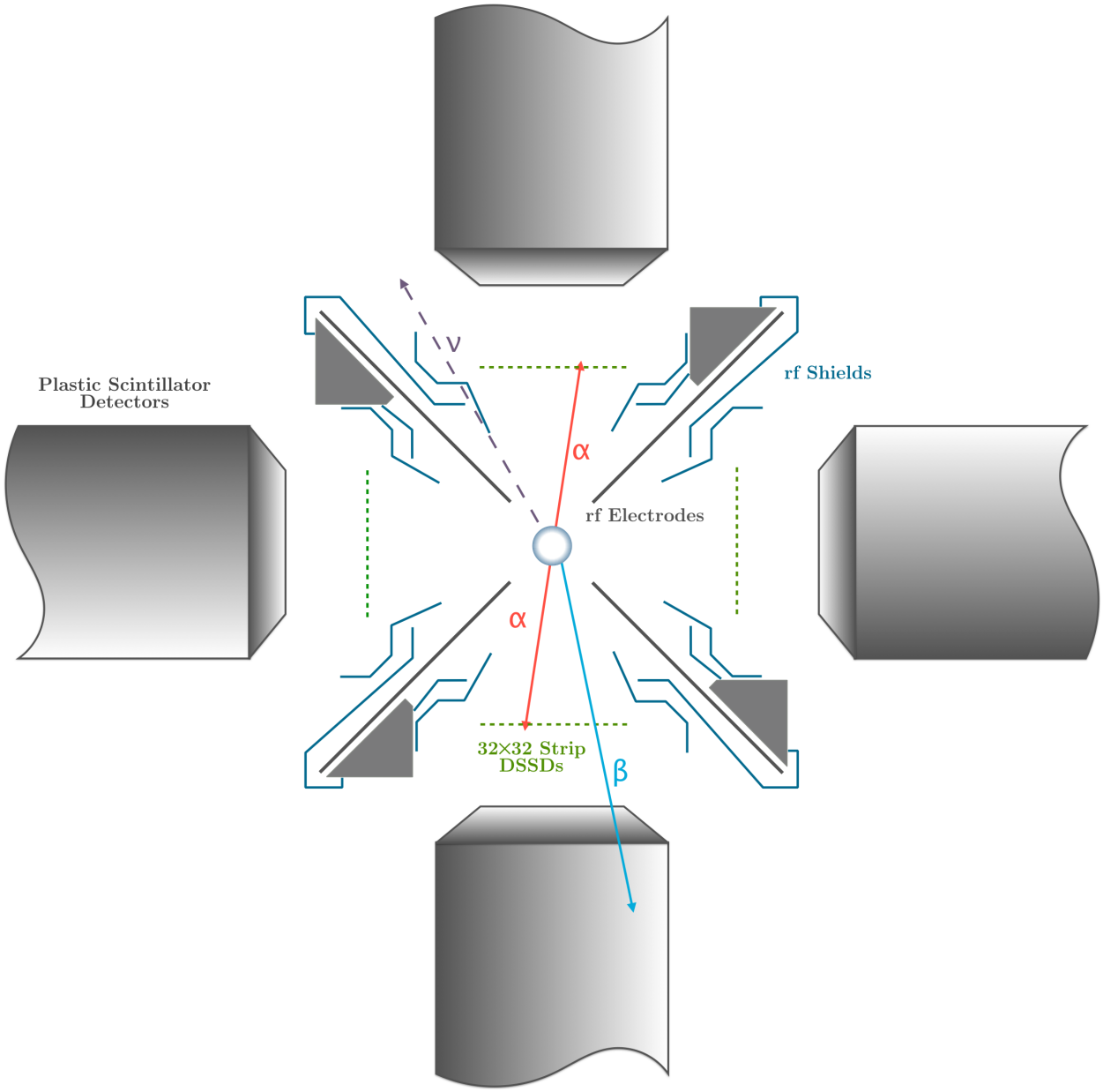

Figure 4.2: Simplified diagram of the Argonne Beta-Decay Paul Trap cross-section

on these tensor currents provide an effective means to probe for possible parity violation in weak decays.

At the ATLAS user facility, a beam of ^{7}Li bombards a neutron-rich D_2 gas target held at liquid-nitrogen temperature. The ions are then injected into a series of systems to transport, cool (to energies less than 1 eV using a He gas buffer), bunch (up to 1 million ions), filter, concentrate, and ultimately store $^{8}Li^{+}$ in the Beta Paul Trap (BPT). While trapped, the ^{8}Li ground state ion beta decays to a first excited state in ^{8}Be that breaks up into two α particles.

The BPT detector system consists of four silicon double sided strip detectors (DSSDs) manufactured by Micron Semiconductor. Each DSSD is comprised of two stacked silicon wafers measuring 1 mm thick and mounted on a thin ceramic plate. Both the so-called junction (front) and ohmic (back) sides are segmented into 32, 2 mm wide strips, providing 256 individual data readout channels. A 100 μm SiO_2 layer along the edges of each strip insulate adjacent strips from one another (Figure 4.3). The DSSDs are mounted perpendicular to the beamline, approximately 65 mm from the center of the trap.

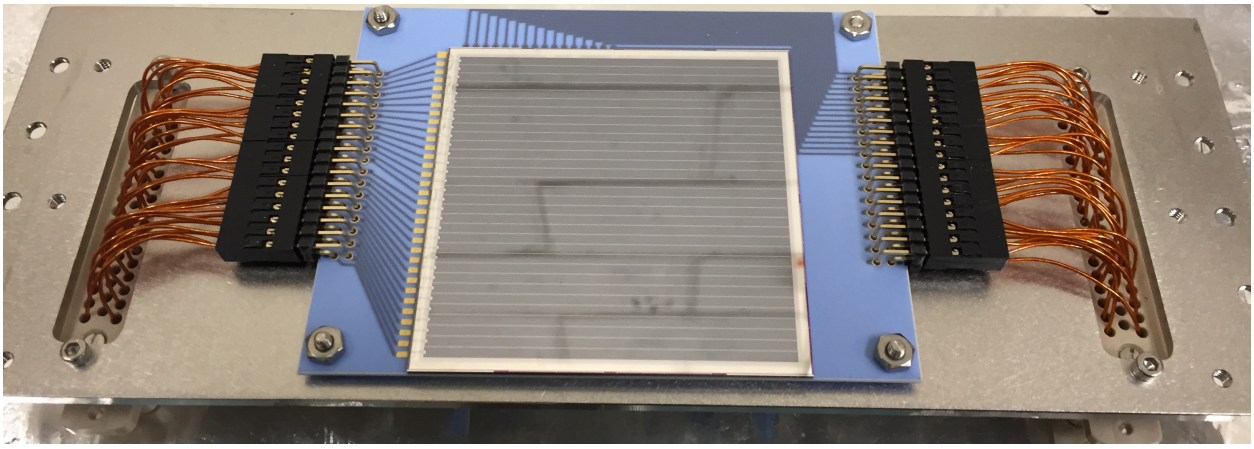

Figure 4.3: A DSSD. The white lines are the insulating edges separating the strips.

Each DSSD records the energies and momenta of the emitted α's and direction of the β. The silicon wafers are sufficiently thin that the β will not fully stop within the material and,

as such, cannot provide a meaningful, high-resolution measurement of the beta spectrum through energy deposited in the strips alone. However, since the α's emitted from a decay at the center of the trap are emitted nearly back-to-back, each will hit a DSSD opposite of the other. When used with the direction information of the β, this information fully constrains the kinematics of the decay products, and the β energies may be reconstructed. This provides a measurement of the beta spectrum independent of the data recorded by the plastic scintillators. Thus, the ^{8}Li BPT experiment provides a novel means by which to characterize and validate the untested plastic scintillator detectors prior to the fission products experiment.

4.2 Preliminary Plastic Scintillator Characterization and Testing

The plastic scintillator detectors have been specially commissioned for the fission products experiment and are designed for high-resolution spectroscopy studies. These detectors had not been previously characterized outside of the manufacturer's initial testing, so their behavior is not fully known. The robustness of the plastic detectors, as well as a good understanding of their characteristic signals was critical to preempt problems that could crop up in the fission experiments themselves.

Numerous experiments have made use of the BPT and, as such, its operating parameters and the peculiarities of its instrumentation are well-studied and understood. The BPT's post-run analysis workflow has been built over the years to the point where there is an established procedure to curate the data to account for known imperfections in the entire measurement scheme, such as broken (or noisy) DSSD strips and dead layer effects. The ^{8}Li BPT experiment provides high-statistics data that is reliable and necessary to ensure that

the plastic detectors operate correctly and capture all the events of interest. Further, the position information from the DSSDs can be used to study any impact of hit position on the plastic scintillator response and further flesh out how well the Geant4 simulations model the data.

To prepare for the ^{8}Li experimental run, the four plastic scintillators were installed on the sides of the BPT perpendicular to the beamline (Figure 4.4). For the remainder of this chapter, the plastic scintillators will be identified by their location relative to the beamline when looking "upstream" as "top," "bottom," "left," (opposite the experimental hall wall) and "right" (closest to the experimental hall wall).

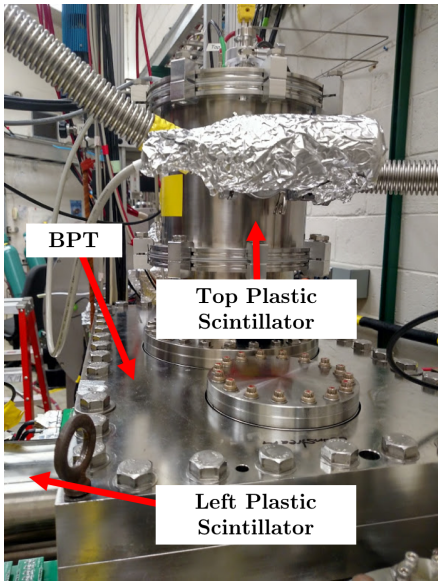

Figure 4.4: The top plastic scintillator mounted on the BPT, facing "upstream."

The Geant4 model of the BPT was updated from the design described in Chapter 3 to more accurately reflect the real BPT geometry by importing a GDML file generated from a CAD rendering used in [36]. Plastic scintillators were added to this new rendering of the BPT in the Geant4 framework, modeled as in Chapter 3. Figure 4.5 shows the more detailed BPT Geant4 geometry and the plastic volumes.

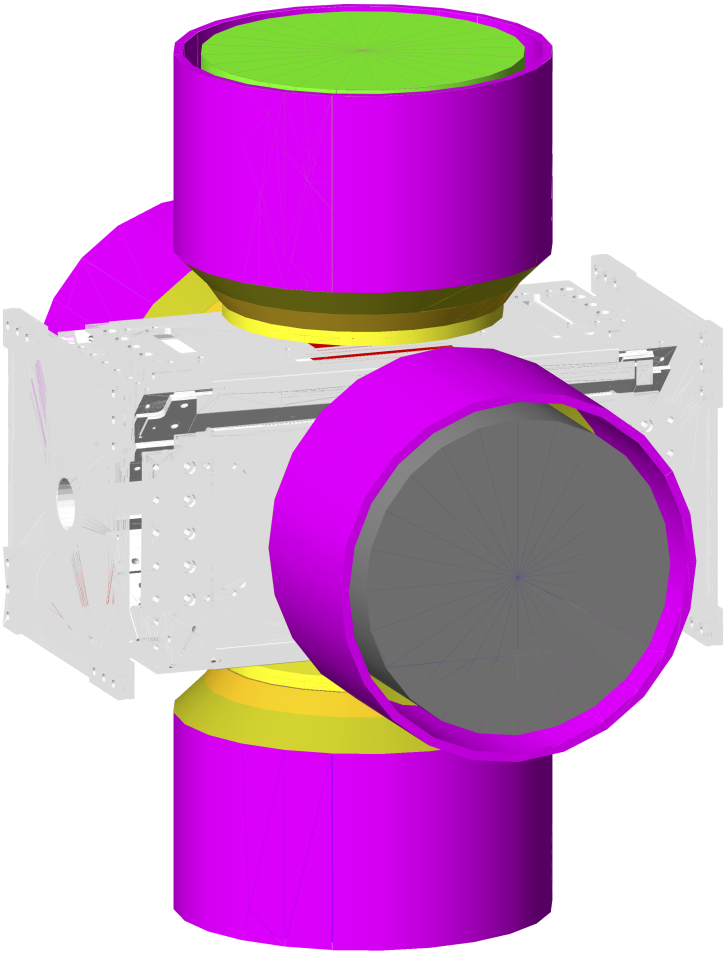

Figure 4.5: The updated BPT Geant4 model.

As described in Chapter 2, a detector output signal is a voltage that is binned in a channel by the data acquisition system. The number of channels and their corresponding voltage assignment range depends on the particulars of the acquisition system hardware and digitization process. Consequently, no single detector calibration is applicable across setups. Detector performance, including efficiency, resolution, and signal gain may depend heavily on the operating environment. Data collection runs may span several hours, or even days, during which time temperature, lighting conditions, and ambient noise may vary. Gain, in particular, is affected not only by temperature, but also by the amount of voltage applied to the PMT. Two blue light-emitting diodes were embedded in the plastic scintillator to serve as reference light sources to allow for gain stabilization during the run. By analyzing the pulse shape of the pulsed LED signals, any gain variation of the PMT over the run may be corrected as described in [30]. Figure 4.6 shows 15, 17, and 20 ns LED pulses recorded with an external ^{137}Cs source, at $\times 20$ gain.

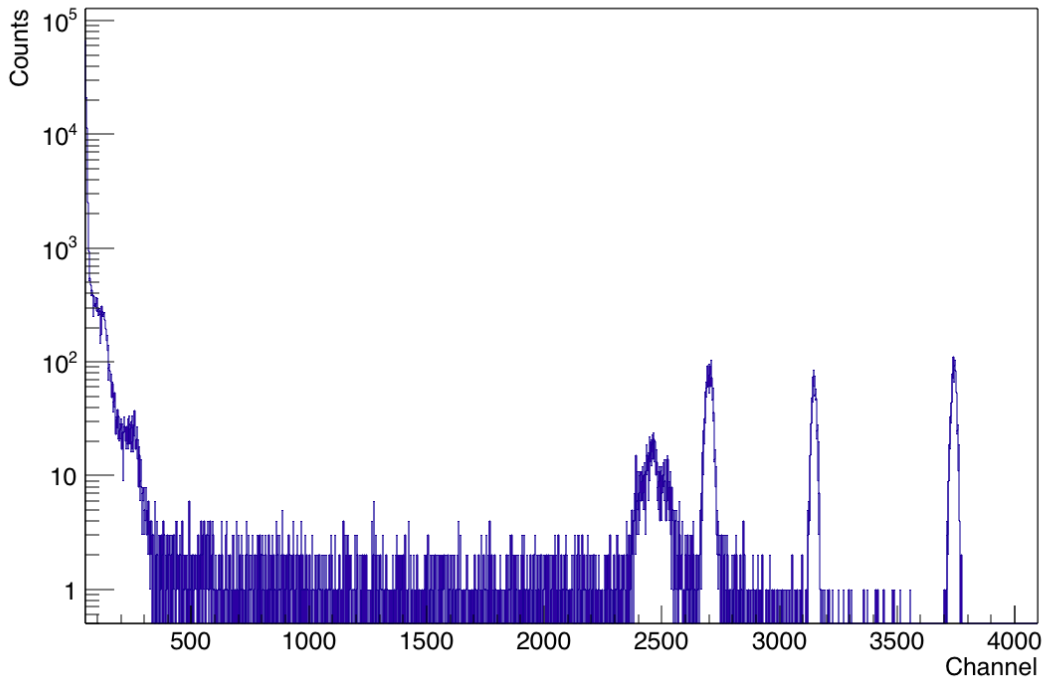

Figure 4.6: Pulsed LED signals with ^{137}Cs reference spectrum.

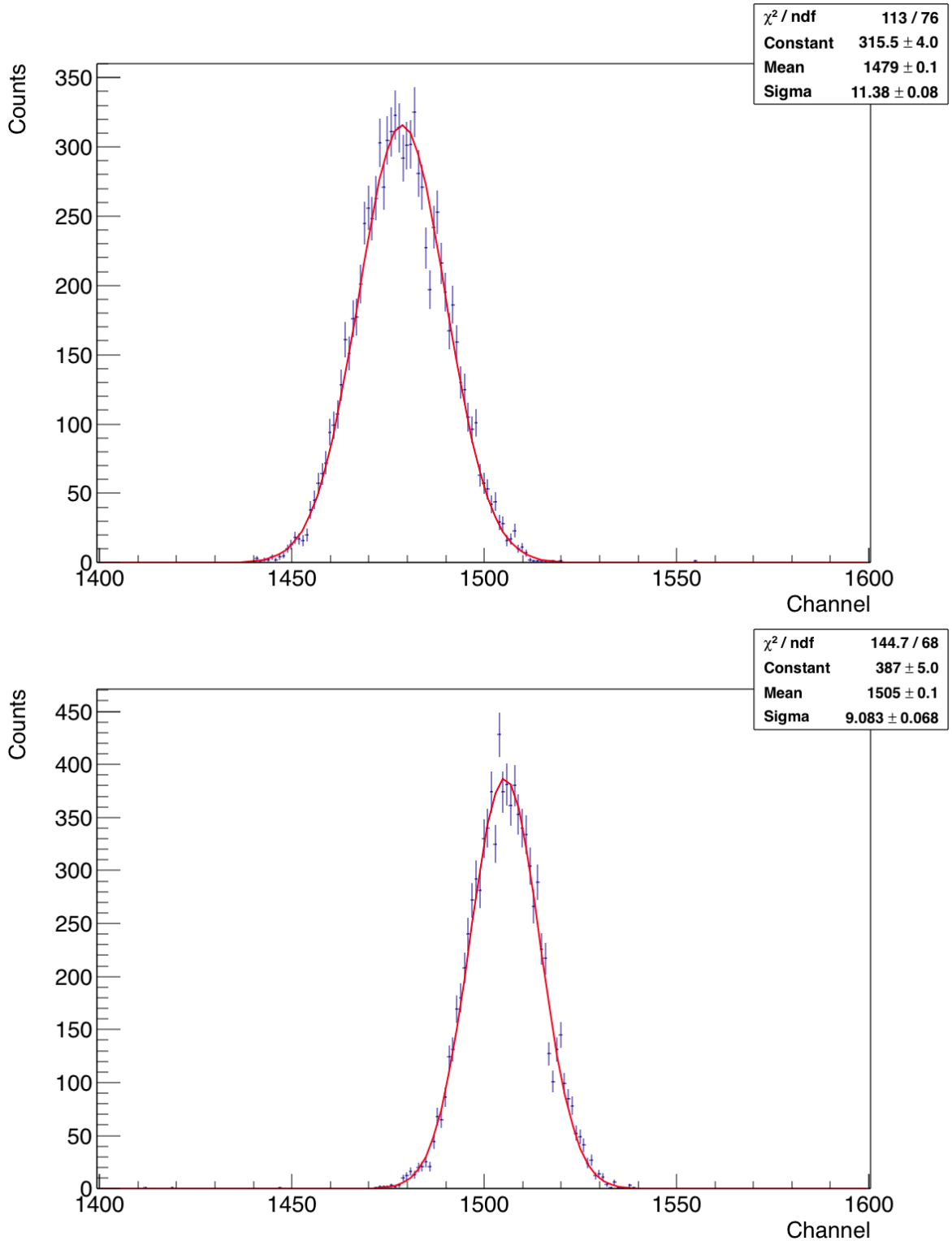

Figure 4.7: Fitted LED pulse signal after 1 hour (top) and 4 hours, 30 minutes (bottom)

In preliminary testing of the plastic scintillators, the LEDs were pulsed using a function generator for 20 ns every 50 ms at $\times 5$ gain. The PMTs were biased at 900 V and the LED was driven at 1.4 V. Data was recorded for eight hours and 20 minutes to allow for changes in external conditions. After the data was collected, the pulses were fit to a Gaussian functional form, with the distribution's μ serving as a reference to evaluate drift of the pulse over time. Figure 4.7 shows example fitted pulses after one hour and four and a half hours. The average mean across the run, $\bar{\mu}$, was 1491.71, with a $\mathrm{Var}(\mu) = 402.18$ and $\bar{\sigma} = 16.63$. The percent difference from each pulse μ from $\bar{\mu}$ is shown in Figure 4.8. The larger difference at the beginning of the run is a consequence of the PMT "warming up" after the bias is first applied and is to be expected. For the remainder of the run, the differences remain within a few percent and within 1σ. This small variation suggests PMT gain will be fairly stable over the duration of most runs (typically lasting between 6 to 10 hours). Unfortunately, LED failure before the fission products experiment prevented similar online monitoring during the data collection run. Nevertheless, these initial tests imply minimal impact of environmental effects on PMT gain and may be absorbed in the overall calibration error.

For spectral analysis, the channel number of the raw data signal must be converted, offline, to an energy scale comparable to that of the simulated spectra. ^{137}Cs (1.168 μCi) and ^{60}Co (1.157 μCi) test sources, manufactured by Eckert & Ziegler [22], were individually placed on the side of the plastic scintillator outer can. Figure 4.9 shows the ^{60}Co source in its storage container.

A rough channel-to-energy scaling is calibrated by examining key features of the measured spectra, such as Compton edges and backscatter peaks, and matching them to the simulated data from the updated BPT simulation. The test sources were modeled as isotropic point sources, placed at roughly the same position on the can, with events generated by Geant4's built-in radioactive decay module (Chapter 3).

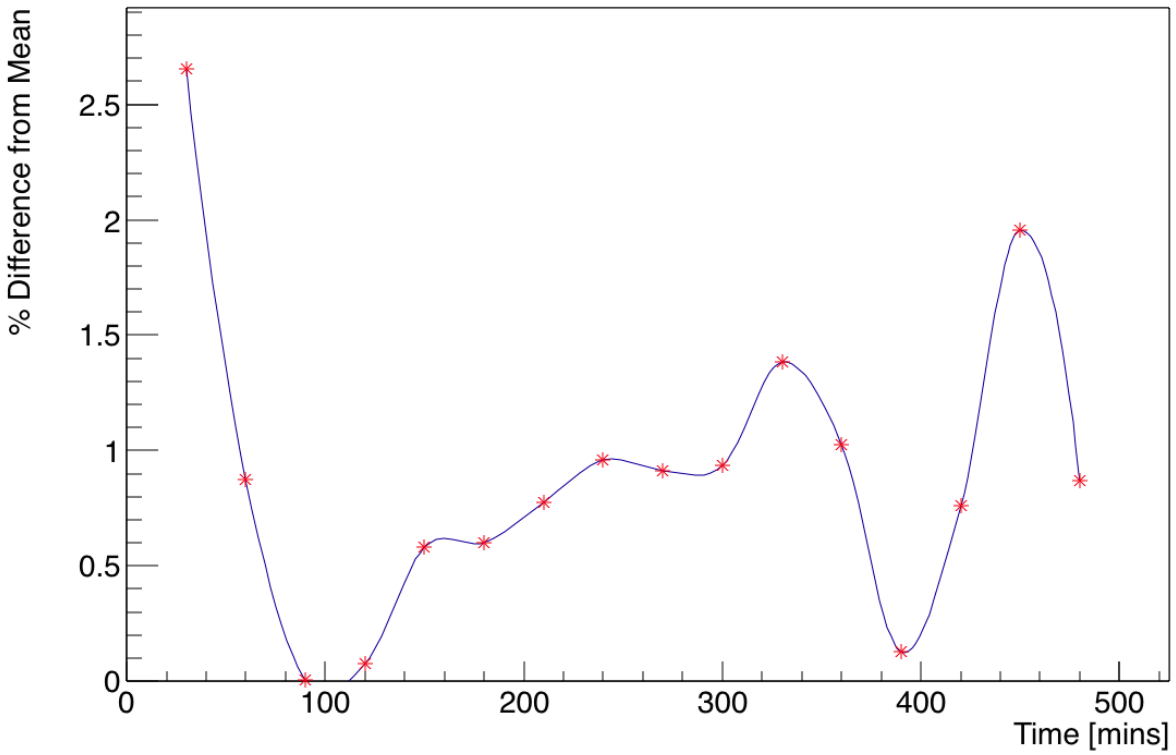

Figure 4.8: Percent difference of pulse μ's from the run's $\bar{\mu}$

Figure 4.9: An example calibration test source.

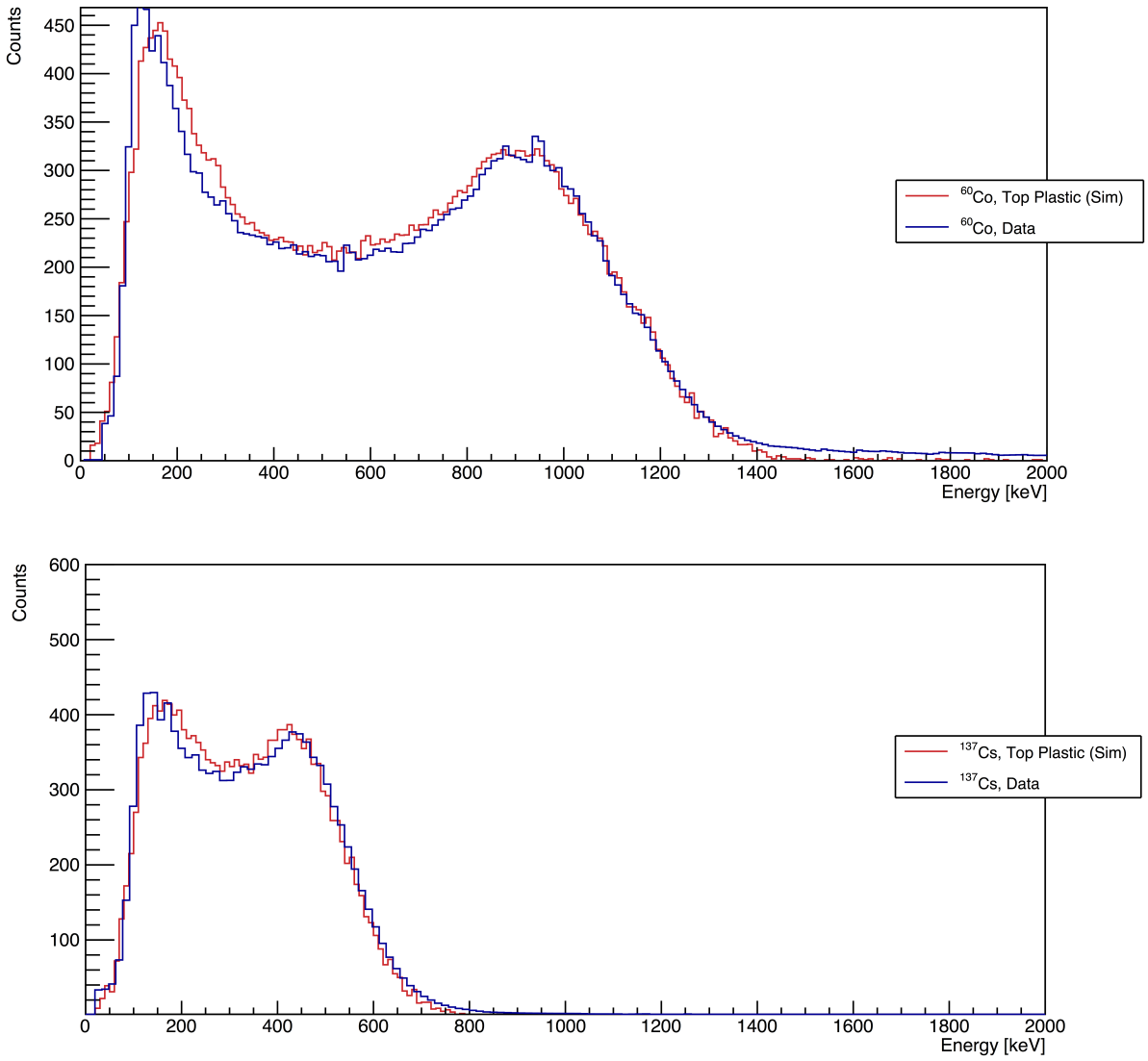

Figure 4.10: Calibrated test source spectra for the top plastic scintillator.

The detector's resolution is determined by adjusting the response function's k value (Chapter 3) incrementally until the simulated spectra features best align with the channel-to-energy scaled data. Figure 4.10 show simulated spectra ($k = .0858\ \sqrt{\text{MeV}}$) overlaid with the scaled ^{137}Cs and ^{60}Co data recorded at the BPT.

4.3 ^{8}Li Plastic Scintillator Calibration

A run of the ^{8}Li BPT experiment was carried out in June 2016, yielding approximately 700000 raw α-β-ν triple events. These high-statistics data were used to better pin down the plastic scintillators' resolution, as well as explore scattering effects modeling in the Geant4 simulation, and investigate possible position dependence of energy deposited in the plastic scintillators.

4.3.1 Plastic Detector Resolution and Scaling Refinement

The β spectrum of ^{92}Rb extends out to energies as high as 8095 keV which is further than the energy region calibrated using the test sources alone. As such, the ^{8}Li spectrum's high-energy tail provides another means to evaluate the calibration in the energy region of interest for the fission products experiment.

The calibration parameters determined in the previous section were applied to the larger ^{8}Li data set and the resolution further refined to match the high-energy tail in preparation for the fission products experimental run. The simulated ^{8}Li events were generated using the BD code, with the BPT and beam parameters set to those observed at the time of the experiment.

The simulated ^{8}Li spectrum for each plastic detector was convolved with the initial estimate for the detector response model and compared to the measurements from the high-statistics run. Using the ^{8}Li high-energy tail information, the channel-to-energy scaling and detector resolution value were refined by following the iterative procedure described in the previous section.

4.3.2 Simulation Validation and Plastic Scintillator Response

The position dependence of the plastic scintillators' response was also evaluated using the DSSD information. The simulation's plastic scintillators are, effectively, ideal in terms of their ability to register hits. In reality, the detector will respond differently depending where the beta particle enters. As the DSSDs are located closely to the front face of the plastic scintillators, the strips provide a good approximation as to where a particle enters front face of the scintillator. Examining smaller regions for significant or unusual variation between data and simulation helps pinpoint areas within the detector where the scintillator's response varies.

Figure 4.11 shows the number of hits on the DSSD per pixel (the overlap region between a front strip and a back strip) gated on the plastic scintillator. Under-performing (e.g., larger-than-average dead layer, loose cabling) or faulty strips are immediately identifiable and will be excluded from both simulations and data in subsequent analysis (Figure 4.11, *bottom*). Examining the strip-hit overlays, the left detector immediately stands out. While this seems to suggest the left plastic scintillator exhibits a more uniform response, the difference is attributable to the detector's mounting location nearest the RF feed-through, apparently increasing the baseline noise level in the DSSD. Similar behavior, albeit less extreme, is apparent in the bottom plastic scintillator, as well. While a center "hot spot" of hits is

visible (effectively the contour of the plastic scintillator face), it is more diffuse than the top and right detectors, which clearly show fewer hits along the edges.

Each DSSD was broken into a grid of 1024 pixels (Figure 4.12). Comparing such a large number of "sub-spectra" across all four detectors is untenable from an analysis standpoint and would result in low statistics for each pixel, making it difficult to identify any obvious problems.

Instead, the DSSDs were remapped to a coarser pixel sampling of groups of 4 strips on each side, providing a total of 64 sub-spectra for each detector (Figures 4.14). 256 sub-spectra were generated for the ^{8}Li data, as well as the simulated spectra. Figure 4.15 and Figure 4.16 show a subset of these spectra.

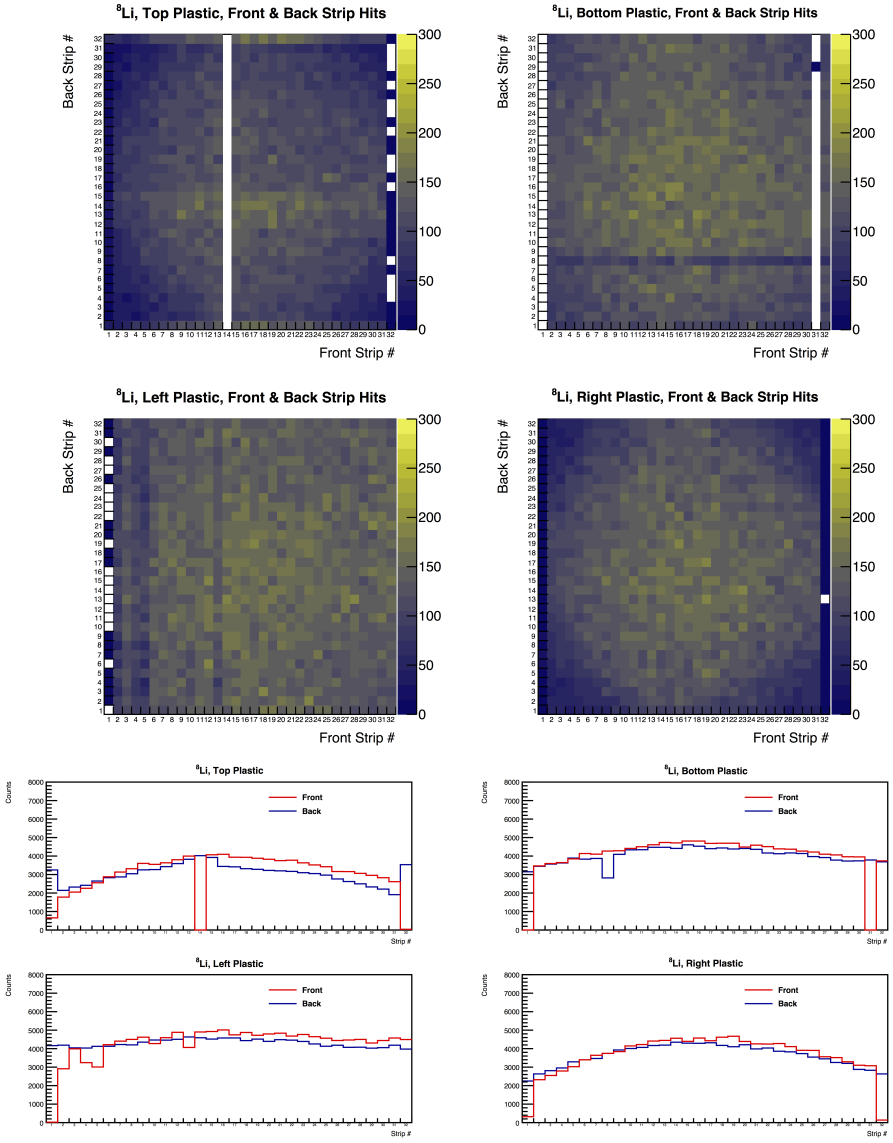

Figure 4.11: Plastic-gated DSSD hits per strip

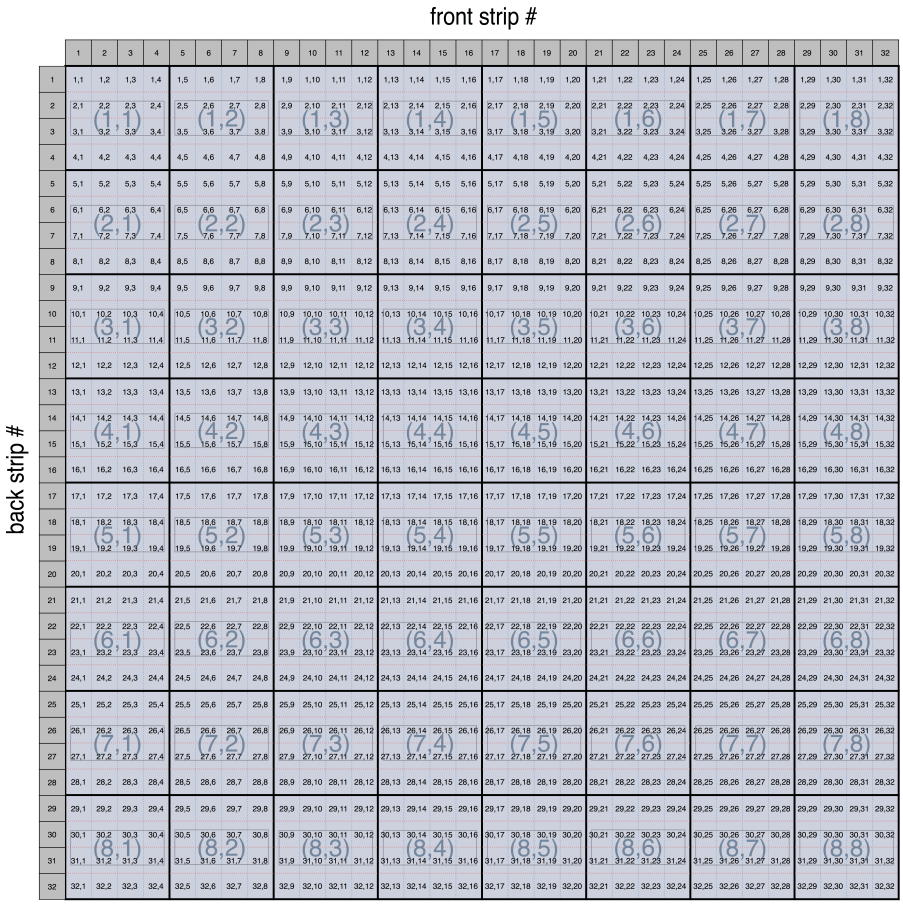

Figure 4.12: The mapping of DSSD pixels

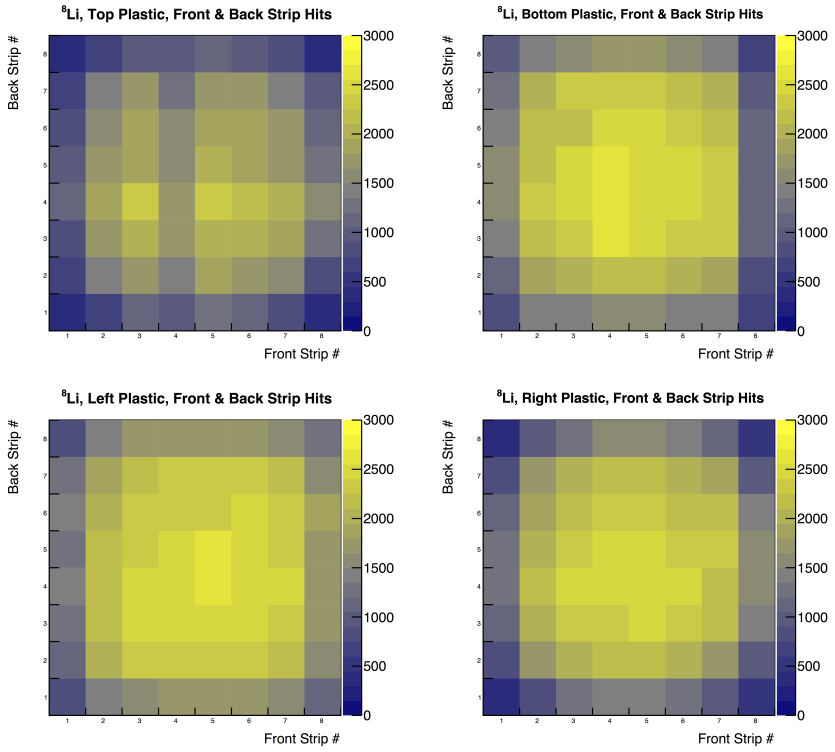

Figure 4.13: Plastic-gated DSSD hits per strip, coarser pixels, with cuts on bad strips

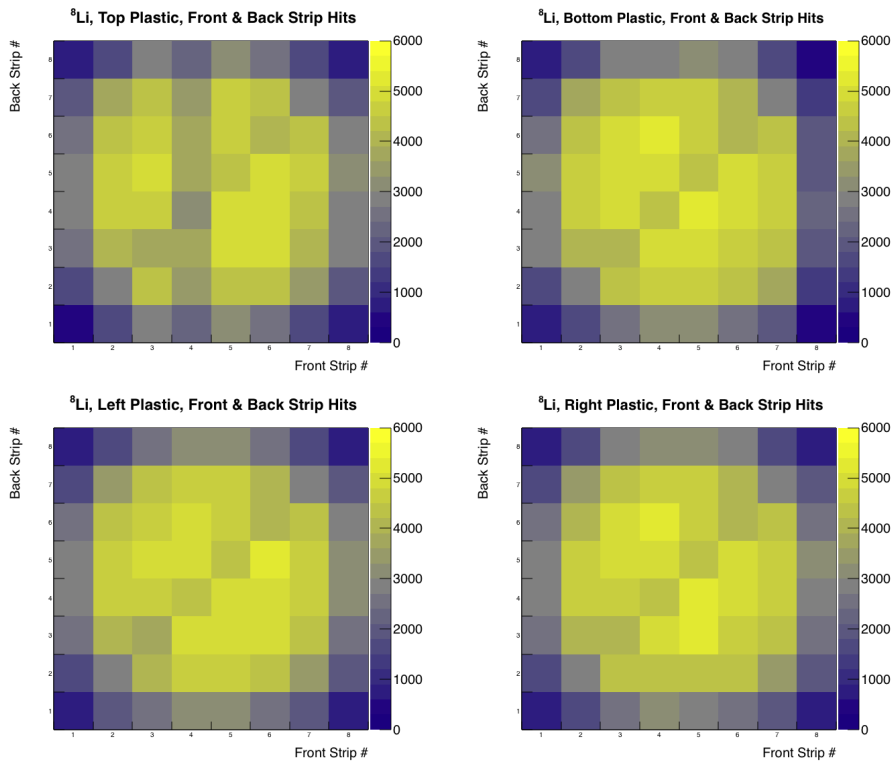

Figure 4.14: Simulated plastic-gated DSSD hits per strip, coarser pixels, with cuts on bad strips

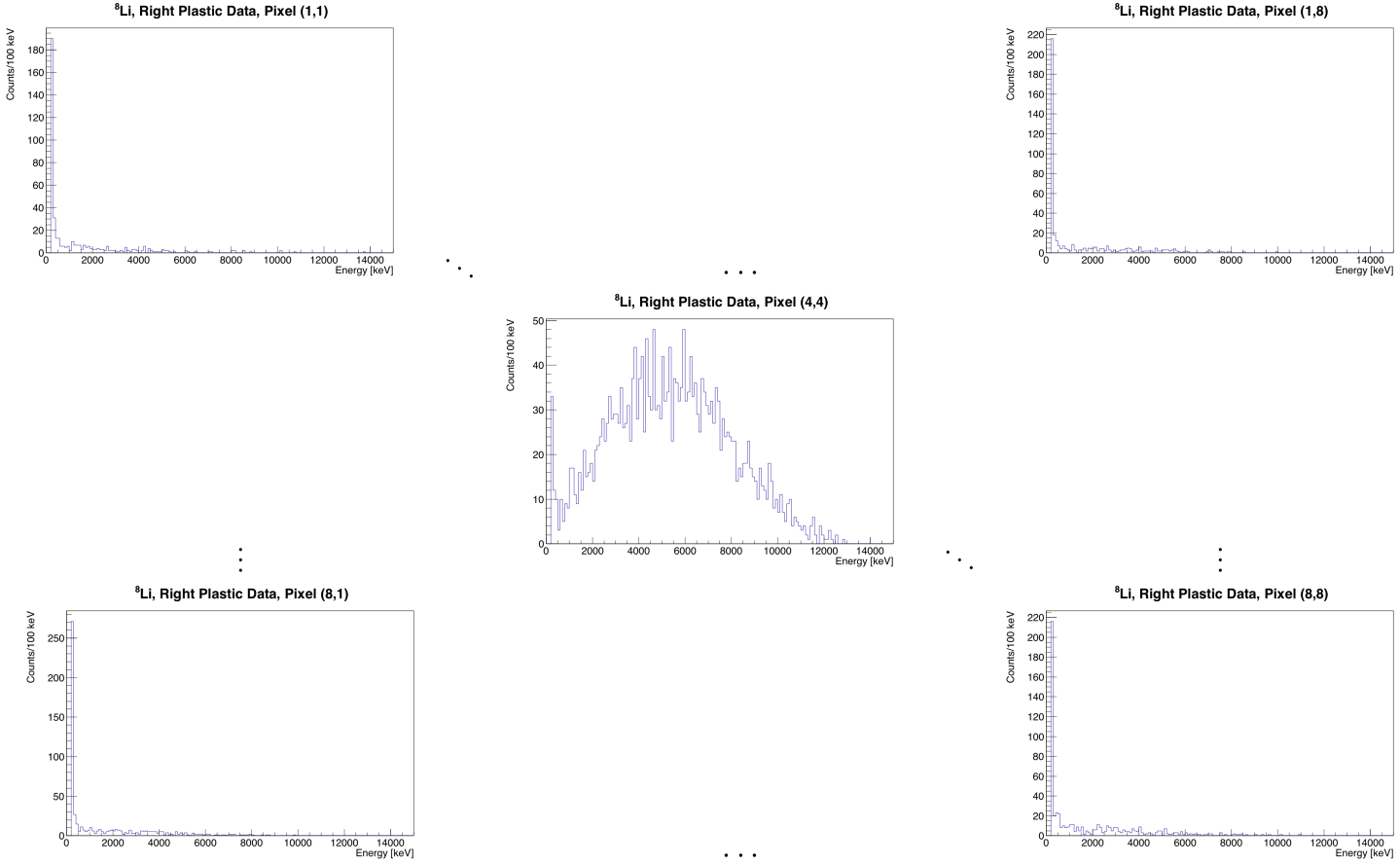

Figure 4.15: Sub-spectra for the right plastic scintillator.

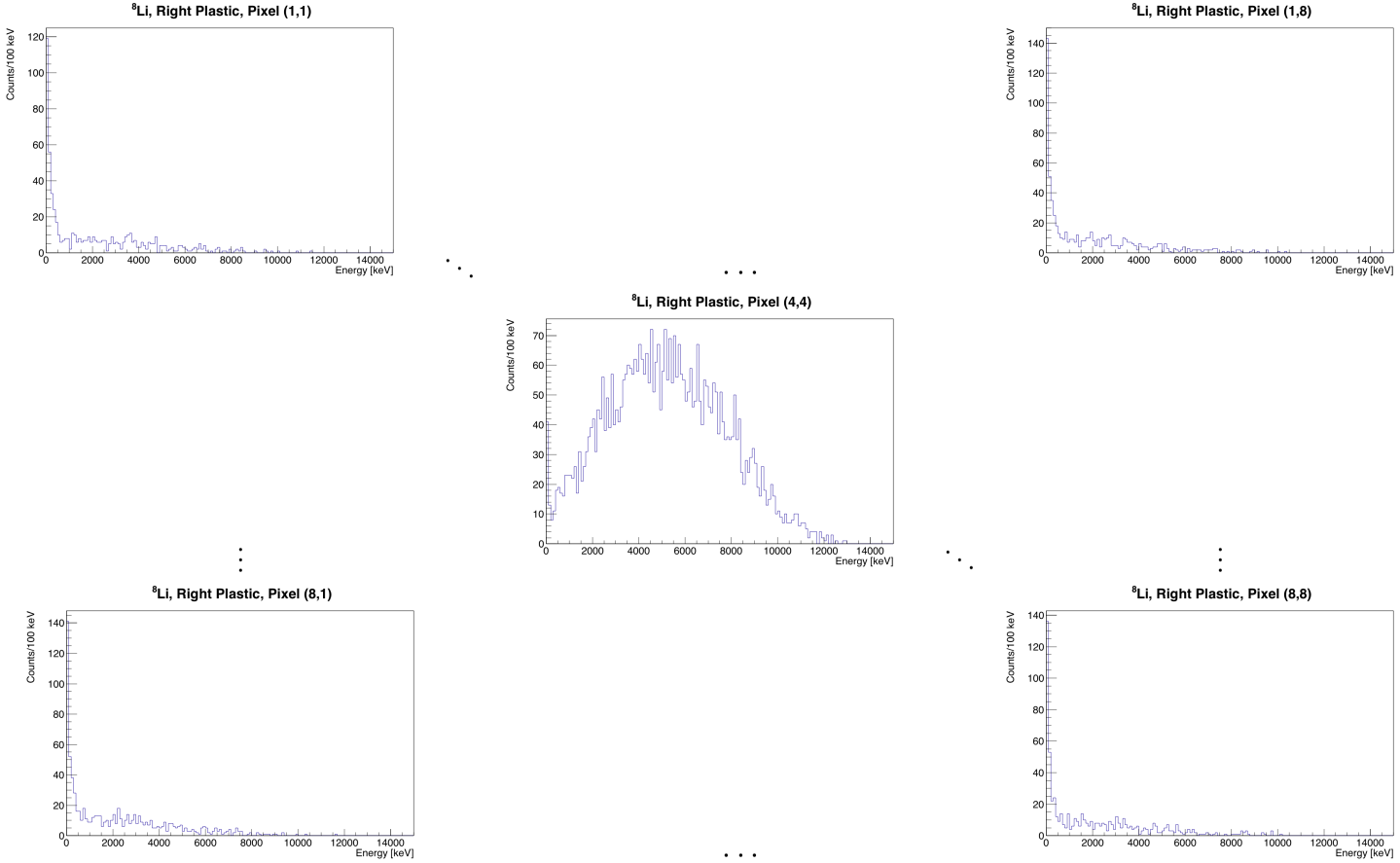

Figure 4.16: Simulated sub-spectra for the right plastic scintillator.

As one might expect, spectra near the edges appear the most distorted and contain significantly fewer counts when compared to the cumulative spectrum. It is less likely that hits in those strips will be in coincidence with the plastic scintillators and lower energies will dominate as the incident particles scatter within the BPT. Closer to the center of the DSSD (and thus, the BPT), where interactions are less likely and more energy is deposited in the plastic scintillator, the sub-spectra begin to more closely resemble the cumulative spectrum. No substantial differences between data and simulation are immediately apparent by eye, and, qualitatively, both exhibit this similar pattern.

To better assess any subtleties, the residuals for each pixel were computed. Figures 4.17 and 4.18 show an example of these plots. The average residual for each pixel was computed to give a sense of the overall agreement between the data and simulated spectra (Figure 4.19). The average residuals are generally quite small and uniform across the majority of the detector face, particularly in the top plastic detector, suggesting the detector response is adequately modeled in the simulation. The right plastic detector shows some variation near the edges.

The left and bottom plastic detectors are less consistent. This is less surprising in the case of the left detector, for the reasons described previously. However, the bottom plastic is not subject to any excessive RF noise and symmetry implies it should behave more or less like the top detector. The benefit of hindsight yields one possible explanation. Immediately before the fission products experimental run, the bottom plastic detector no longer produced a signal. Reduced performance, manifesting as the spot diffuseness, may have been symptomatic of eventual PMT failure. The amount of time necessary to return the detector to the manufacturer for repair would have greatly exceeded the scheduled duration of the experimental run and, as such, this detector was ultimately excluded from the fission products experiment, resulting in the loss of one telescope.

4.4 Discussion and Conclusion

The simulations model of the experiment was modified to better reflect the nuances of the BPT design. Embedded LEDs, intended for monitoring gain changes in the plastic scintillator detectors over the fission products experimental run, were tested. Using the LEDs, the plastic scintillator detectors' PMT gain changes were found to be small (Figure 4.8) over durations larger than the intended fission products experimental run.

Overall, data from the high-statistics ^{8}Li data collection run appear to be well-modeled by the updated BPT Geant4 simulations (Figures 4.15 and 4.16). The plastic scintillator response of each detector was evaluated by examining DSSD-gated spectra on a strip-by-strip basis and was found to be mostly uniform (Figure 4.19) when compared to the simulated data. Each detector's response was largely in agreement with the others, though deviation in the bottom detector possibly indicated eventual PMT failure. The estimated detector resolution used to model the detector response is consistent with that reported in similar mass-8 experiments measuring α-β-ν angular correlations and weak magnitism corrections, as indicated by the small differences between the simulated and measured ^{8}Li spectra examined in this chapter. These detector characterization studies provide confidence in the ability of the Geant4 simulations to accurately replicate the experiment and give insight into the performance of the previously untested plastic scintillator detectors.

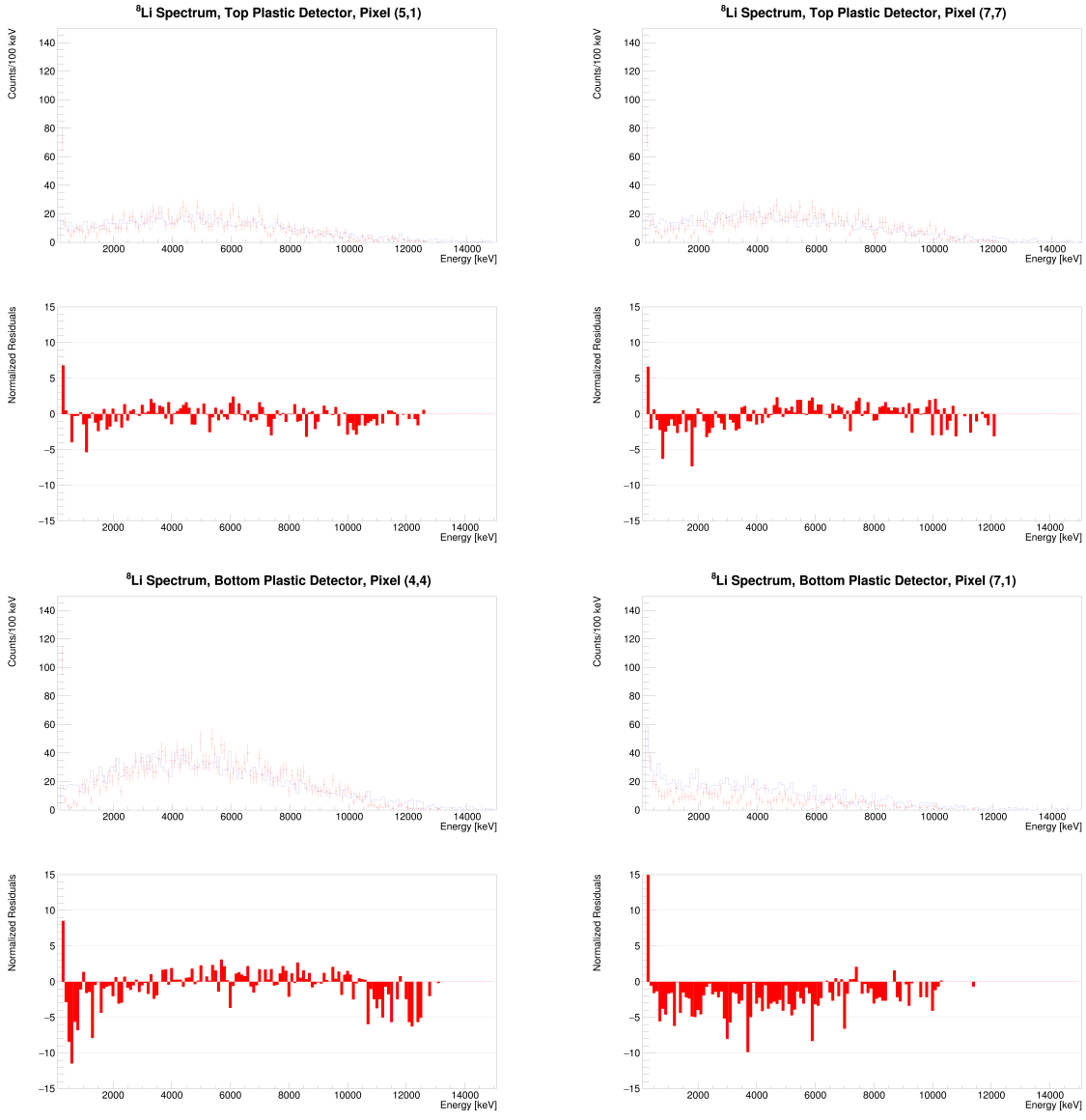

Figure 4.17: Overlaid simulation (blue) and data (red) sub-spectra and residuals (Top and Bottom).

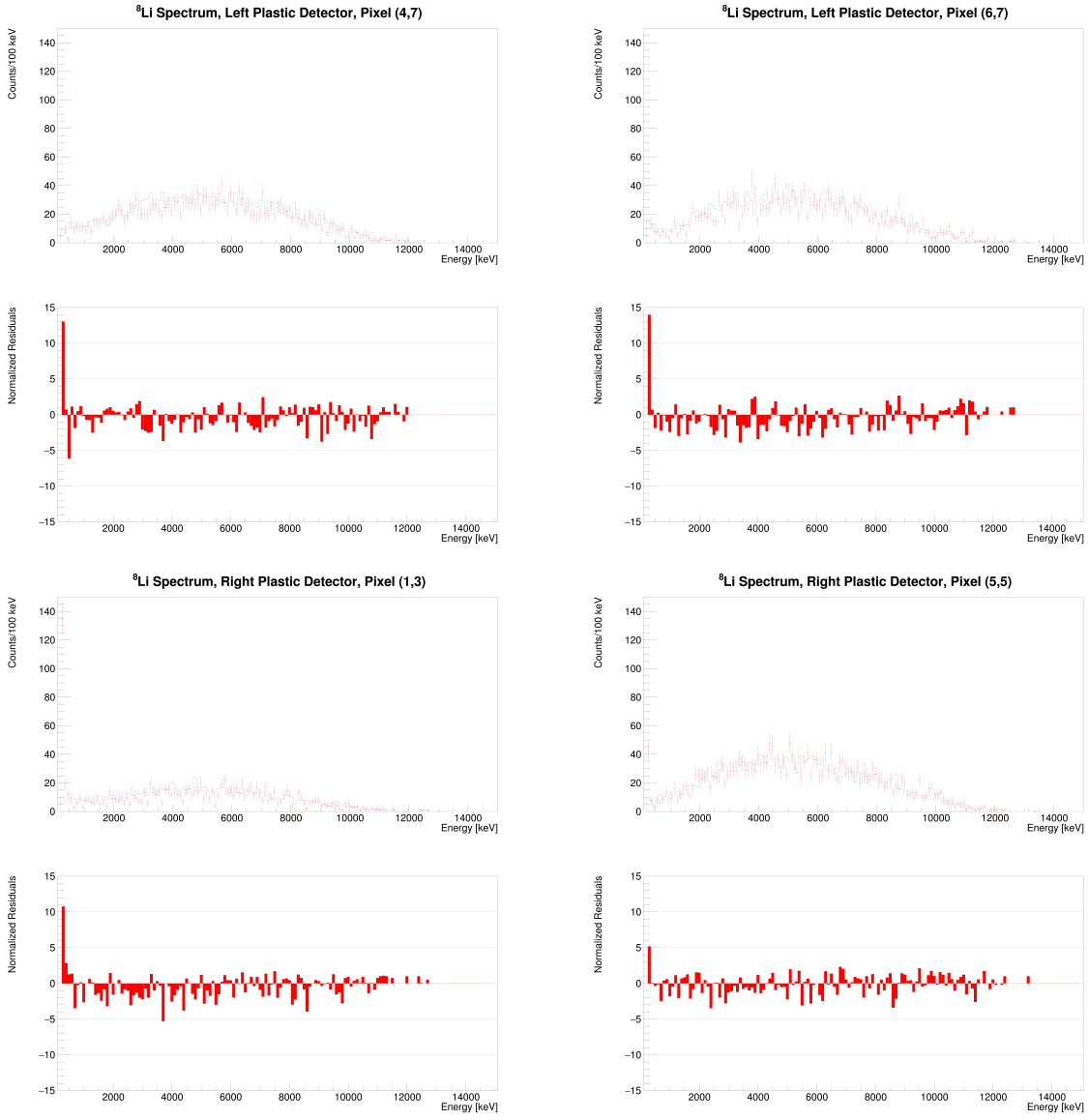

Figure 4.18: Overlaid simulation (blue) and data (red) sub-spectra and residuals (Left and Right).

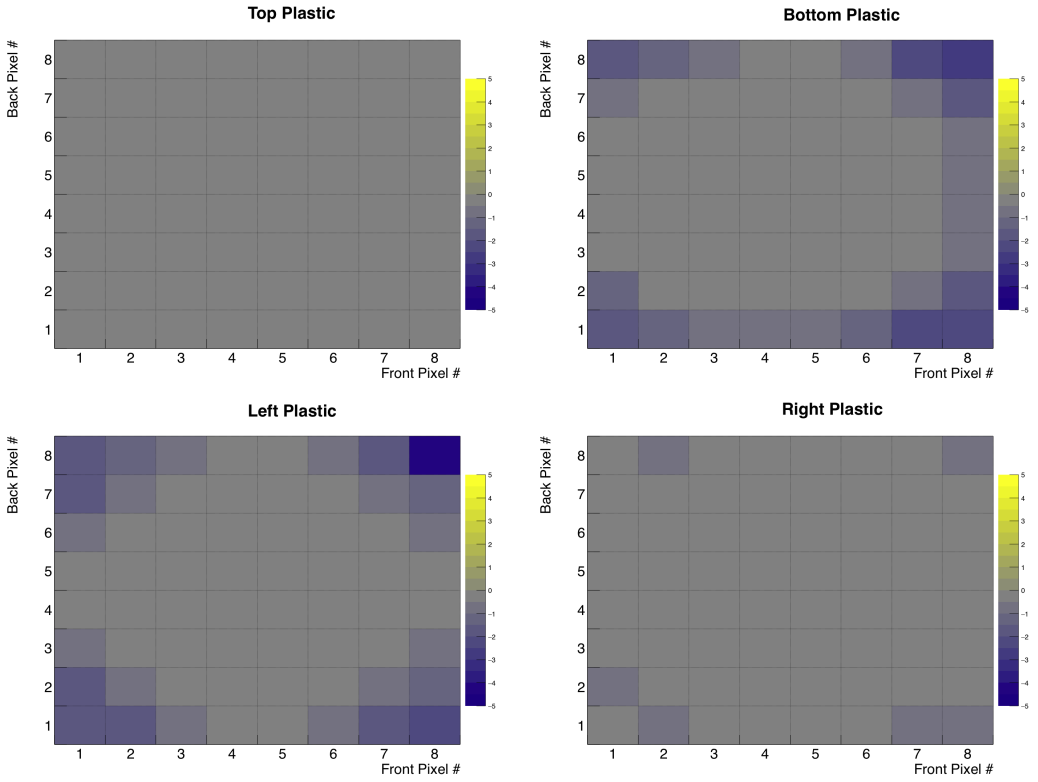

Figure 4.19: Average residuals for each pixel.

Chapter 5

Analysis

5.1 Detector Array Design Finalization Simulations

Originally, "tape collimators" were used to replicate BPT geometry's electrodes as well as to focus beta particles originating from the implanted source to reduce scattering off other surfaces inside the pseudo-trap. After the pseudo-trap frame was constructed, it was observed that the aluminized mylar tape would likely scrape against the collimator tape channel, producing a fine, pervasive aluminum dust throughout the chamber that might short or otherwise damage the sensitive detector equipment.

The fission products pseudo-trap was re-modeled with updated dimensions and additional relatively small changes to the geometry in Geant4 (Figure 5.1) to evaluate if removing the collimator would significantly impact statistics in the telescopes, or inappropriately distort the spectra and obfuscate any weak magnetism correction.

Simulations with and without the tape collimators were run in Geant4 using isotropic, monoenergetic electron sources of 2, 4, and 6 MeV placed at the center of the pseudo-trap to

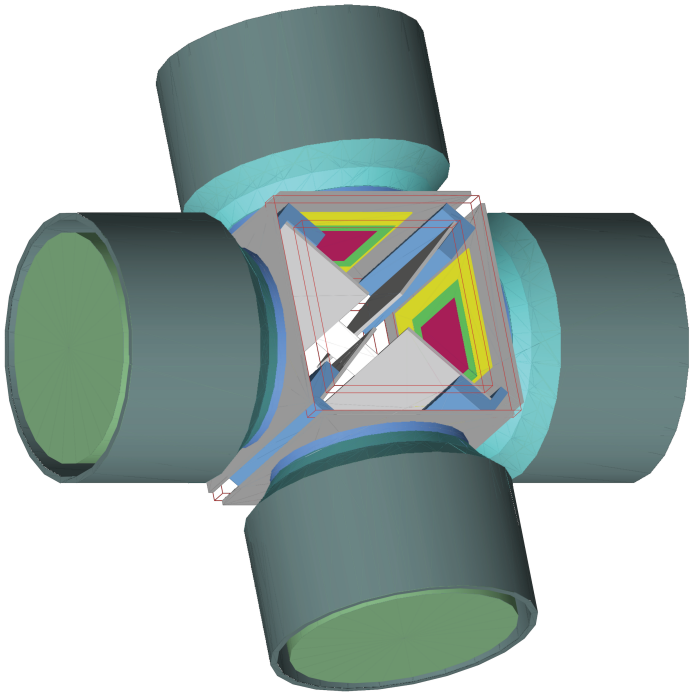

Figure 5.1: A Geant4 rendering of the fission products experiment's pseudo-trap (*v.2*).

test the net effect of changing the geometry. Figures 5.2 show the aggragate telescope spectra for a 2 MeV electron source in the "with collimators" and "without collimators" scenarios. The low-energy tail, arising from scattering within the chamber, is smaller than in the "with collimators" configuration by approximately 2 eV.

The resulting spectra for the three energies were convolved assuming a "worst-case-scenario" k (as defined in 3) value equal to 0.1 $\sqrt{\text{MeV}}$ observed in similar plastic scintillator detectors and fit with a Gaussian function to examine the "smearing" and amount of distortion induced by scattering (Figures 5.3 and 5.4).

Energy	With Col.	Without Col
2 MeV	0.106	0.105
4 MeV	0.107	0.107
6 MeV	0.109	0.110

Table 5.1: Calculated k ($\sqrt{\text{MeV}}$) from fit.

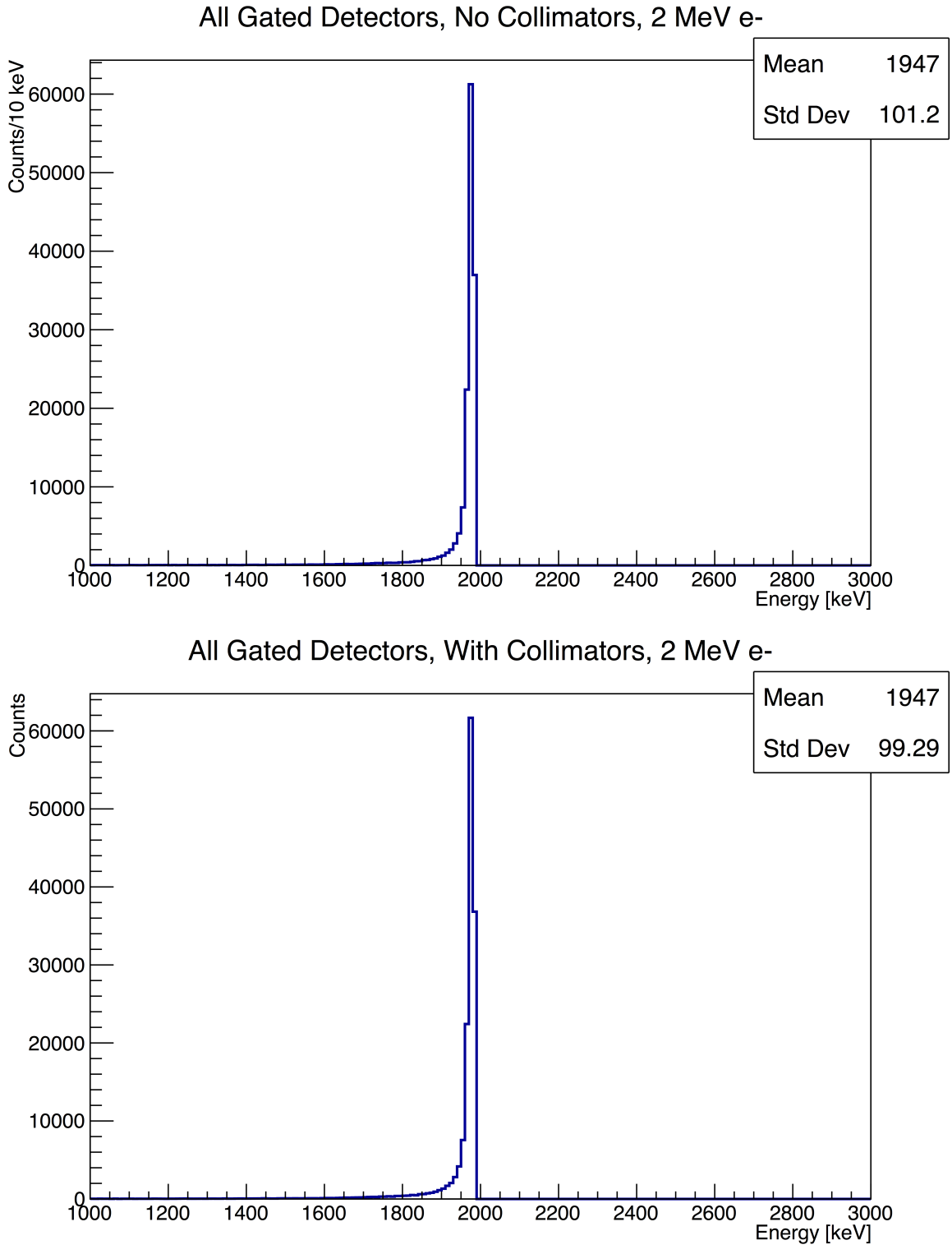

Figure 5.2: Total spectra for a 2 MeV electron source with (top) and without (bottom) tape collimators.

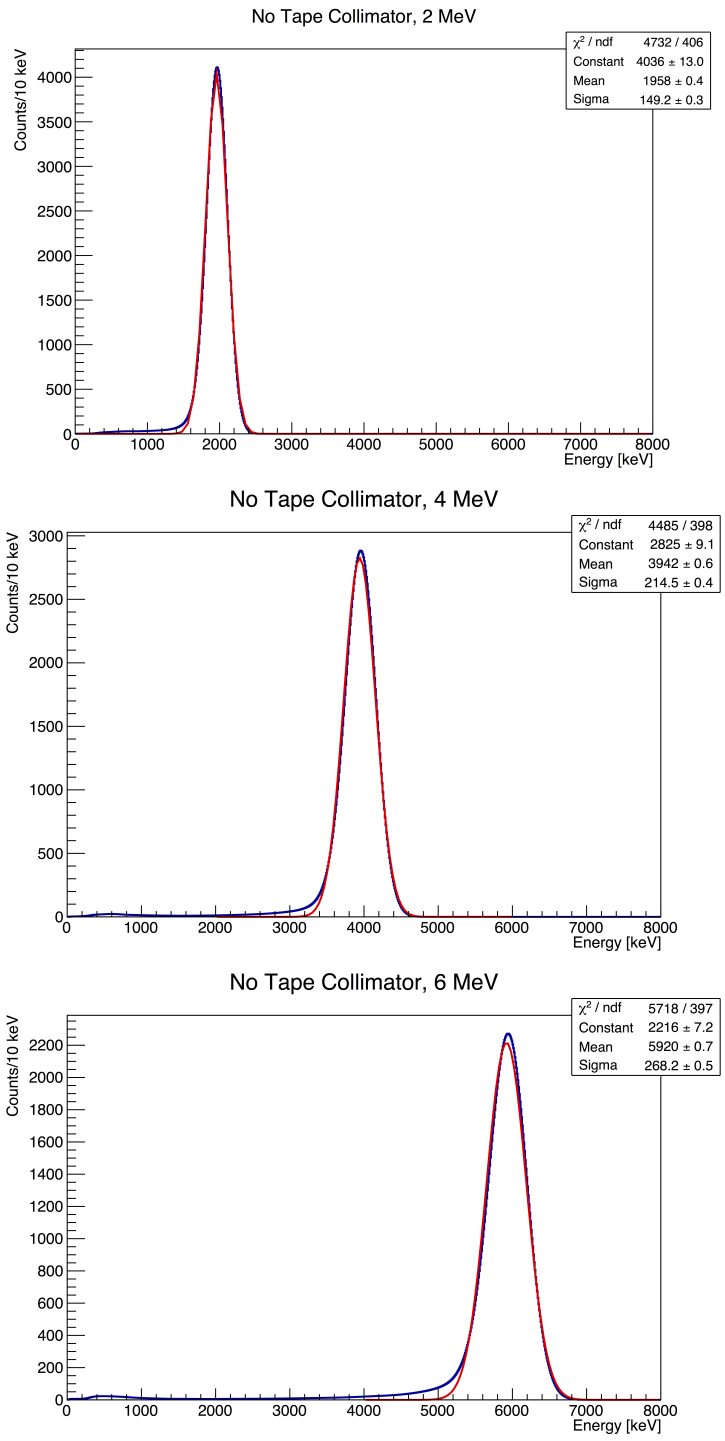

Figure 5.3: Fitted spectra for 2, 4, and 6 MeV electron sources without tape collimators.

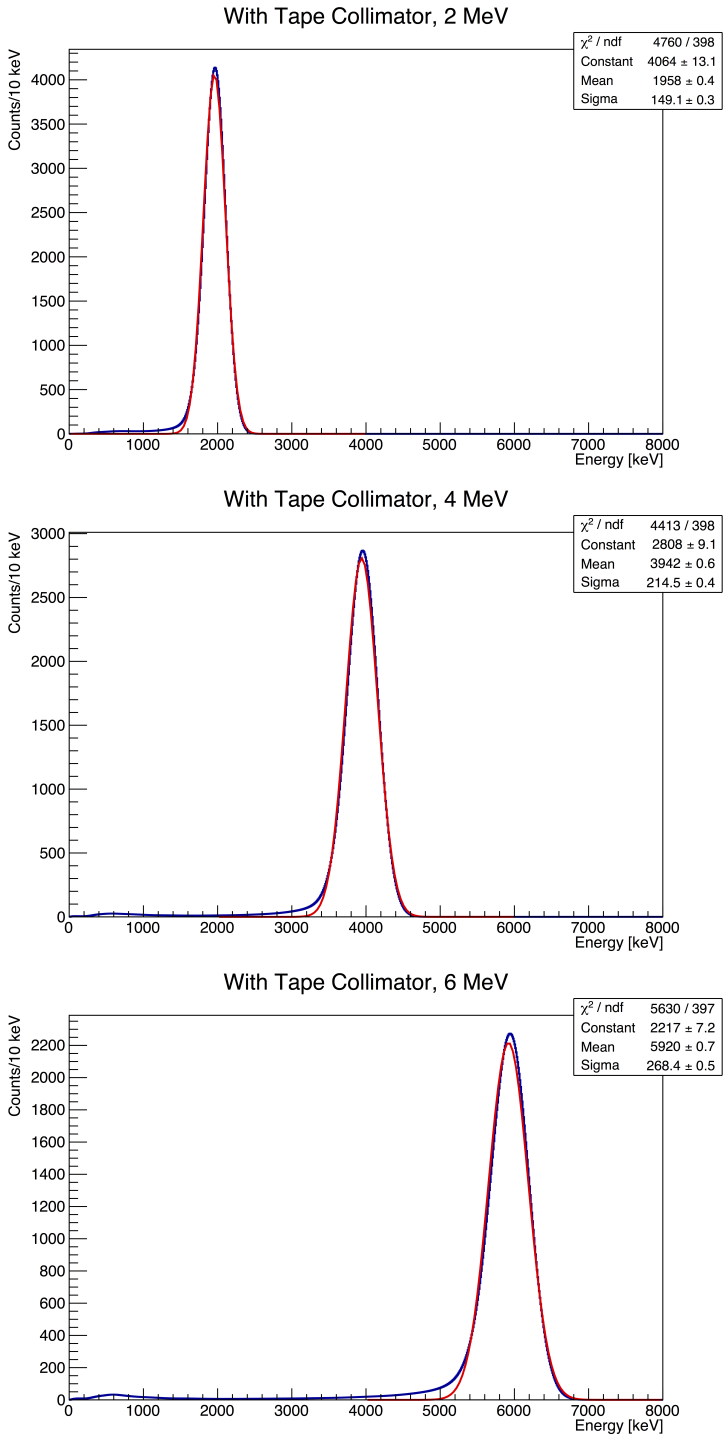

Figure 5.4: Fitted spectra for 2, 4, and 6 MeV electron sources with tape collimators.

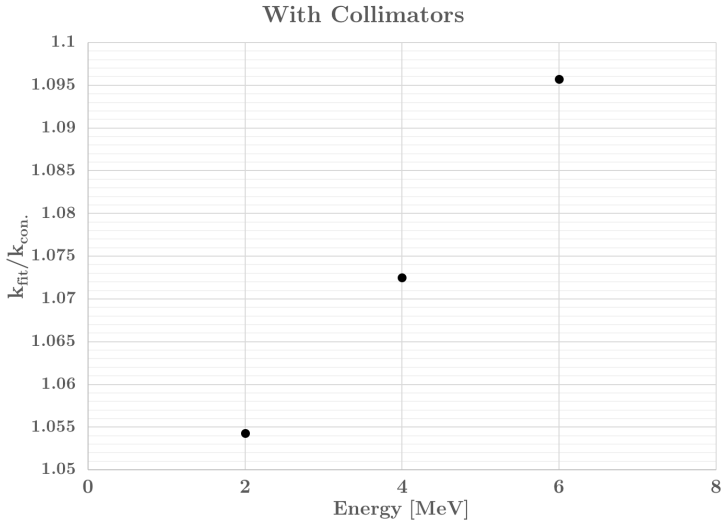

Figure 5.5: $k_{fit}/k_{convolved}$ values for the "with collimators" case.

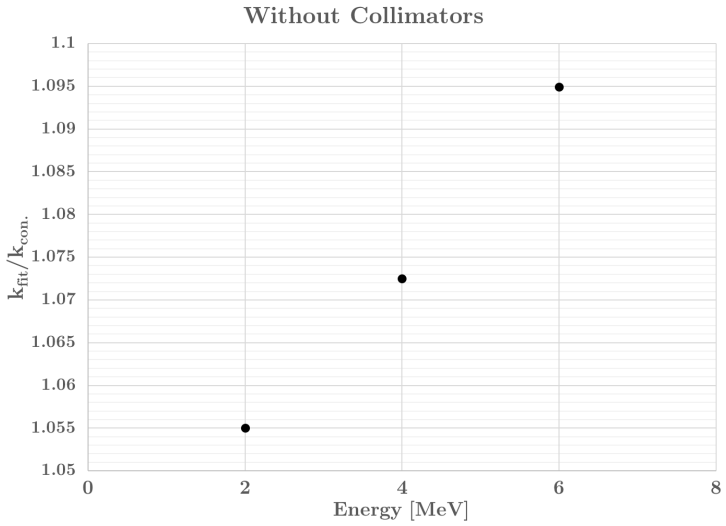

Figure 5.6: $k_{fit}/k_{convolved}$ values for the "without collimators" case.

The σ of the fit was used to determine the k value at each energy (Table 5.1). The calculated k values for each configuration differs from the other by less than 0.001 $\sqrt{\text{MeV}}$. In both cases, the k value remains quite close to the 0.1 $\sqrt{\text{MeV}}$ value, and over all three energies varies by no more than 0.01 $\sqrt{\text{MeV}}$ from the assumed value. Figures 5.5 and 5.6 plot the values of $k_{fit}/k_{convolved}$ for each geometry. Distortions to the spectra from additional scattering surfaces appear to be well-modeled by the simulation and do not vary significantly in either case.

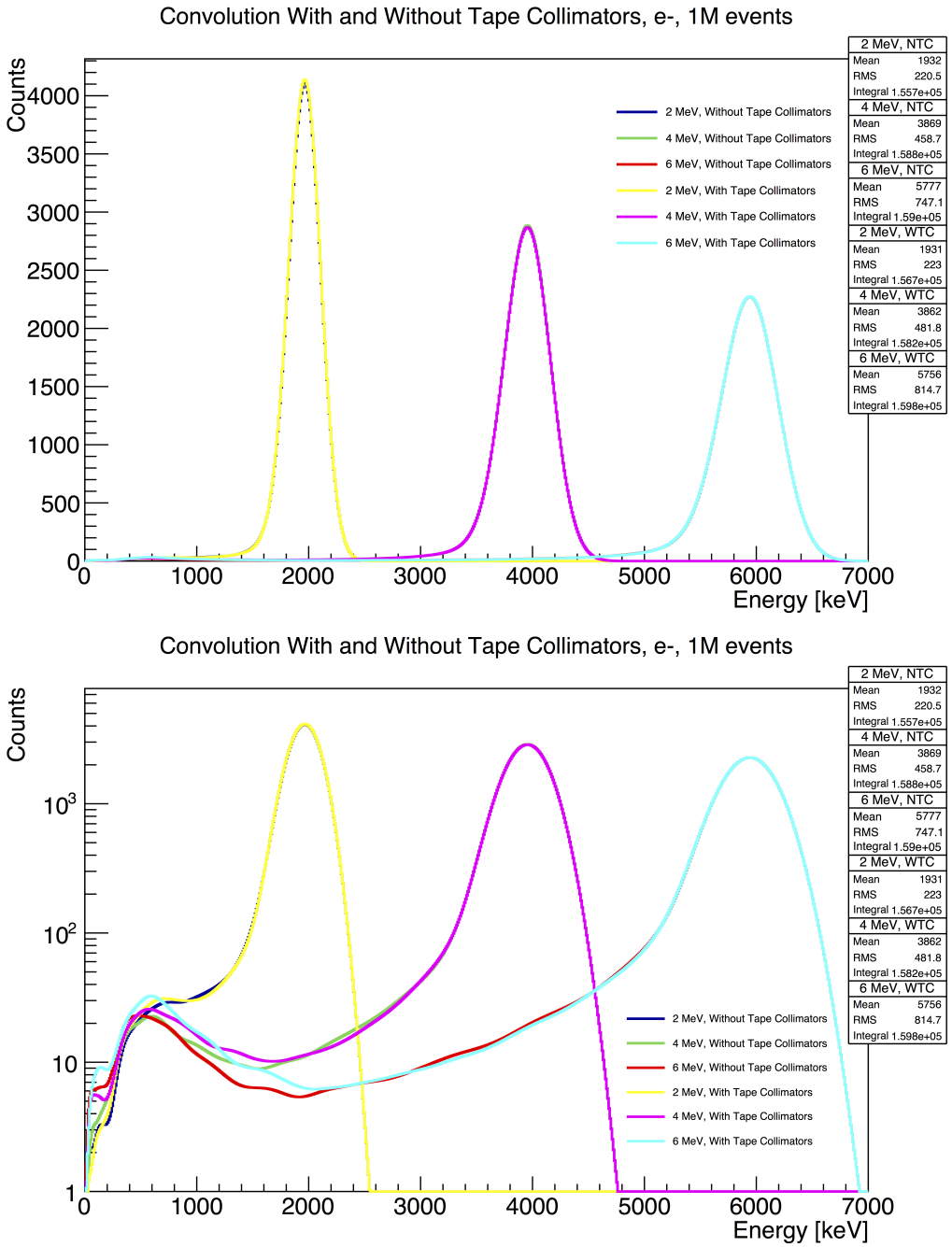

Figure 5.7: Overlaid monoenergetic electron spectra with and without the tape collimators on linear (top) and logarithmic scales (bottom).

The loss of beta particle collimation induced by the ersatz electrodes will necessarily decrease the statistics in real coincident events from the source. Figure 5.7 (*top*) shows an overlay of convolved electron source spectra. Above 1 MeV, any difference in the two scenarios is virtually imperceptible, with the "without collimators" case spectra mostly obscured by the

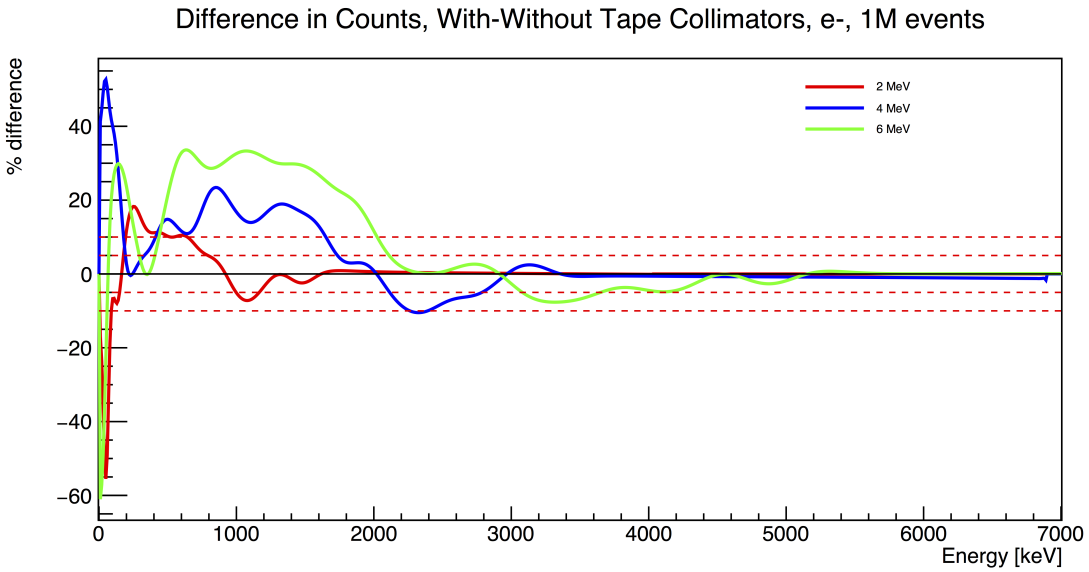

Figure 5.8: Percent difference in detected events between the "with collimators" and "without collimators" geometries. The red dashed lines denote differences of 5% and 10%.

overlaid "with collimators" case. The exact variation in counts is revealed by examining the same spectra on a logarithmic scale (Figure 5.7, *bottom*), with the most obvious changes in counts appearing in the low energy region. The percent-difference in event counts between the two scenarios (Figure 5.8) illustrates the most problematic energy regions. Counts of particles at higher energies remain within 10% between the cases over the majority of the energy region, with the count rate suffering most noticeably below 1 MeV.

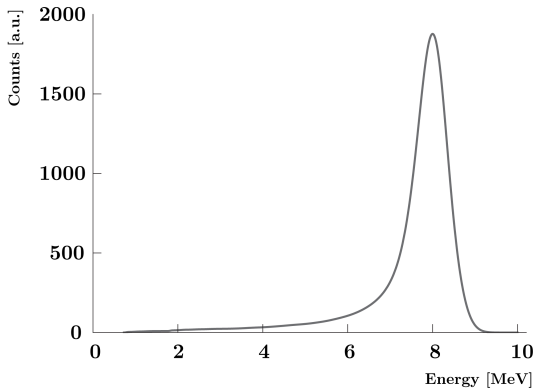

Figure 5.9: Response function of an E detector used in a mass-8 weak magnetism term study (adapted from [38]).

While removing the tape collimators from the pseudo-trap reduces the number of events recorded on the silicon-gated plastics, particularly at energies above 2 MeV, the difference in the 4 MeV to 6 MeV region of interest for examining deviations from predicted spectral shape is smaller than approximately 5%. Moreover, as the maximum energy of ^{8}Li is ca. 13 MeV, removing the collimators should not pose a problem when comparing the results from the ^{8}Li plastics endpoint calibration to that measured at the fission products experiment's calibration during the data collection run. Additionally, the size of the low energy tail is consistent (with the collimators removed) with a monoenergetic beta particle spectrum reported by Sumikama, et al. (Figure 5.9)[38].

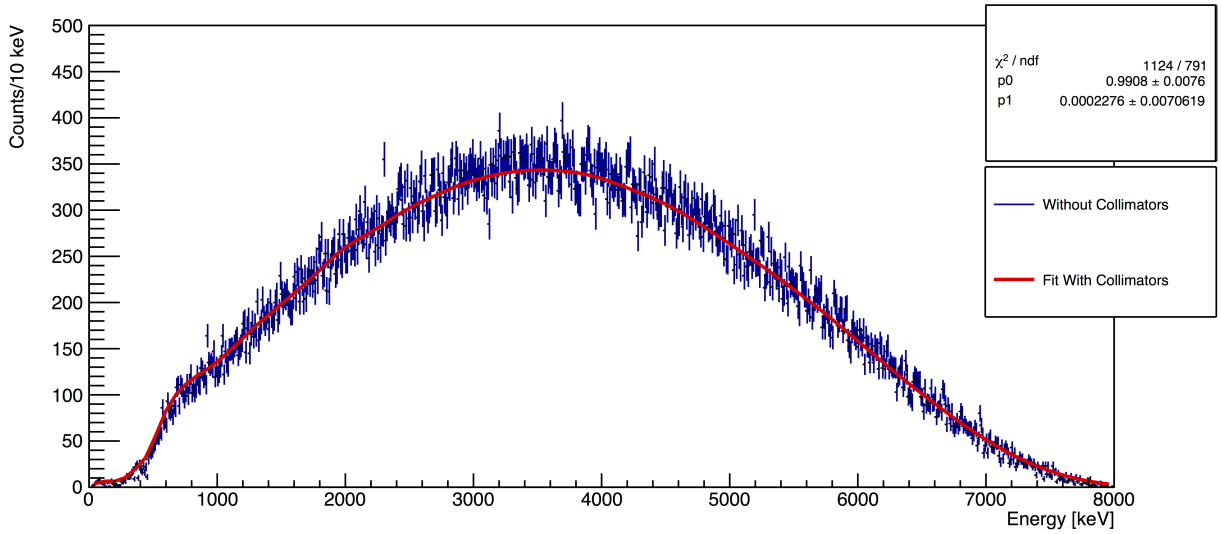

Figure 5.10: The fitted simulated ^{92}Rb spectrum with tape collimators removed.

The effect of removing the tape collimators on the weak magnetism slope parameter was also evaluated. A ^{92}Rb spectrum was generated by the BD code and flown into the Geant4 simulation of the updated pseudo-trap (Section 5.1) for the "with collimators" case assuming a purely-allowed spectral shape and a purely-weak magnetism spectral shape. The linear combination of these two spectra were fit to a convolved purely-allowed spectrum simulated with the collimators removed (Figure 5.10). The artificial weak magnetism contribution introduced by removing the tape collimators is several orders of magnitude smaller than

thought (and of comparable uncertainty to the allowed contribution–also quite small) to be detectable at the fission products experiment and will not significantly contribute to the overall error in the measured weak magnetism parameter.

5.2 Further Simulation Refinement

For the offline data analysis, the geometry of the fission products experiment was modeled in considerably greater detail using Autodesk Fusion 360$^{\text{TM}}$ (Figure 5.11). The geometry was updated to include the spherical chamber, the pseudo-trap without the tape collimators, HPGe reentrant ports, the silicon detector, with true-to-life dimensions for the ceramic and silicon (oriented to reflect their placement during the run), the silicon detector ceramic standoffs from the edges, and the plastic detectors. This model was then exported as a .STEP file and converted to GDML format using FastRad® [40]. Figure 5.12 shows the chamber as visualized in Geant4.

All subsequent simulations were run using the *emstandard_opt4* physics list constructor for electromagnetic interactions, which is designed for high-accuracy electron tracking by using low-energy models. In particular, the emstandard_opt4 constructor utilizes the Goudsmit-Saunderson model for multiple scattering (as opposed to the *UrbanMSCModel*) which employs the most accurate algorithm for scattering at geometry boundaries below 100 MeV. Prior ^{8}Li studies used an older standard physics list constructor and implemented the Goudsmit-Saunderson model, specified deliberately in the physics list file, for simulations. The Goudsmit-Saunderson model is well-validated and has been shown to model backscattered electrons to within 10% or better, with optimized parameters for range cut (which governs the threshold for secondary particle production) and range factor (which restricts the step size of a transported particle within geometry materials).

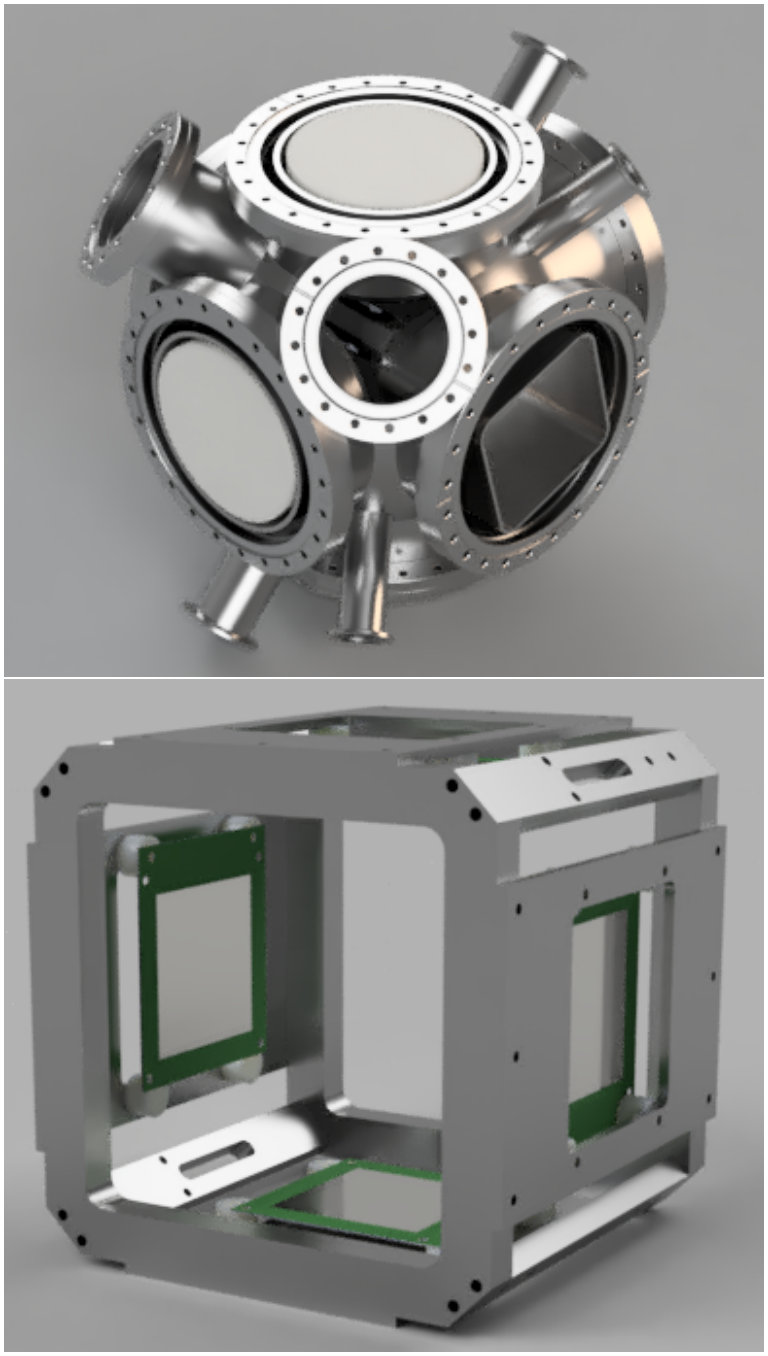

Figure 5.11: Autodesk Fusion 360$^{\text{TM}}$ renderings of the fission products chamber (top) and pseudo-trap (bottom).

Figure 5.12: Geant4 visualization of the fission products chamber/pseudo-trap (*v.3*) with (top) and without (bottom) the HPGe reentrant ports.

5.3 Fission Products Experiment Data Collection Run

5.3.1 *In Situ* Plastic Calibrations

Calibrations were performed *in situ* at the time of the run by placing test sources on the tape in the center of the chamber (Figure 5.13). Two test sources, ^{207}Bi and ^{106}Ru, were used to calibrate the detectors. To calibrate the bottom telescopes, the test sources were turned upside down, with the activity pointed at the tape, to minimize the amount of material between the source and telescope.

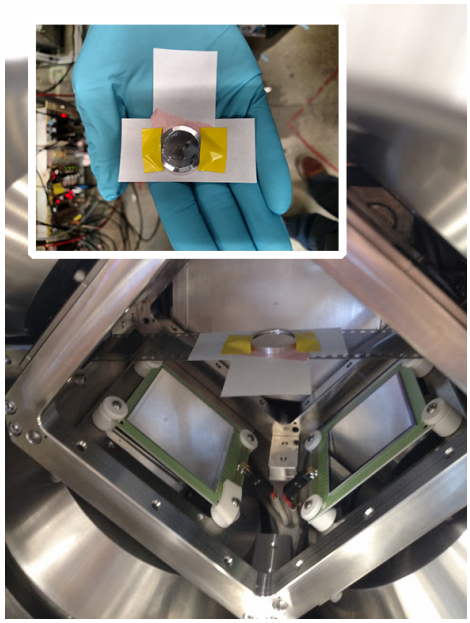

Figure 5.13: The placement of the ^{106}Ru calibration source in the chamber. The active element is approximately 20 mm in diameter, under the aluminized mylar foil window (inset).

Timing cuts were applied to the test sources to clean the spectroscopic data for comparison to the simulated test source spectra. Coincidences across all times are shown in Figure 5.14. Since each detector exhibits unique behavior, a universal timing cut cannot be applied to both detectors simultaneously (with the exception of the global timing cuts imposed by the tape signal in the case of ^{92}Rb described later). Figure 5.15 shows the relationship between

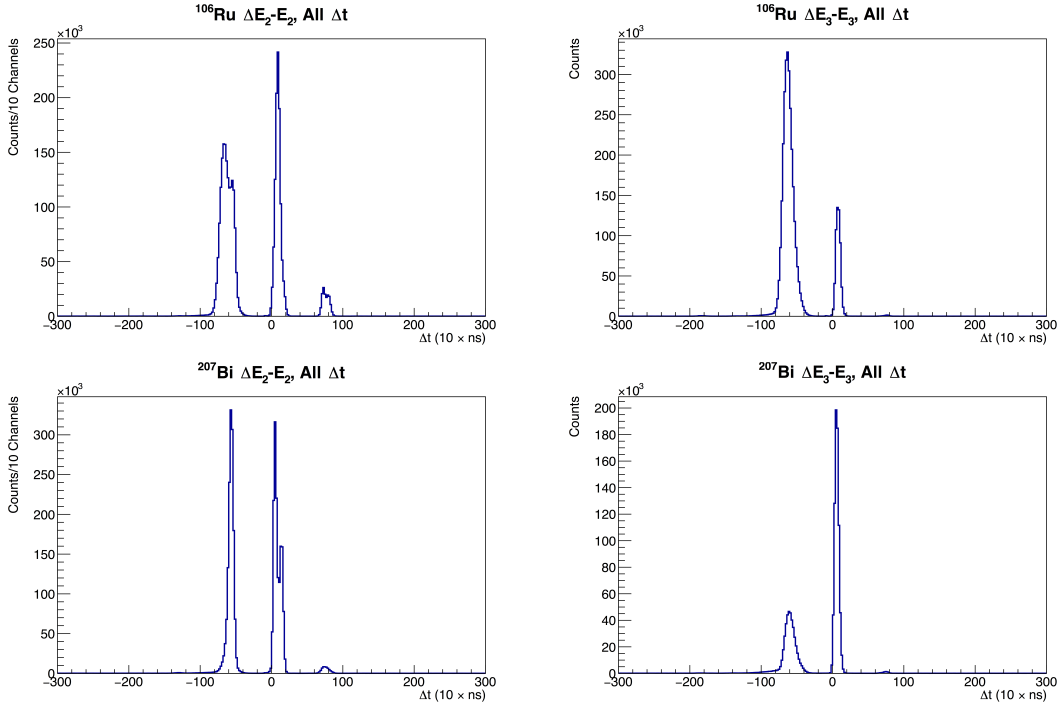

Figure 5.14: Coincidences in each telescope across all times.

time coincidences and the plastic channel number for each telescope, while Figure 5.16 shows the same plot for the silicon detectors.

The signals from the calibration sources are immediately identifiable as high-intensity features, providing a means to select appropriate timing intervals to eliminate accidental coincidences. The coincidence plots with timing cuts for the silicon detectors are shown in Figure 5.17.

The heavy bands visible near the lower channels in Figures 5.15 and 5.16 are the result of constant noise in the detectors counted as coincidences and other low-energy background activity present in the experimental hall. To remove this additional source of background, representative samples of accidental coincidences away from the signal feature were averaged and subtracted from in the timing range of real calibration source signal in the plastic detectors.

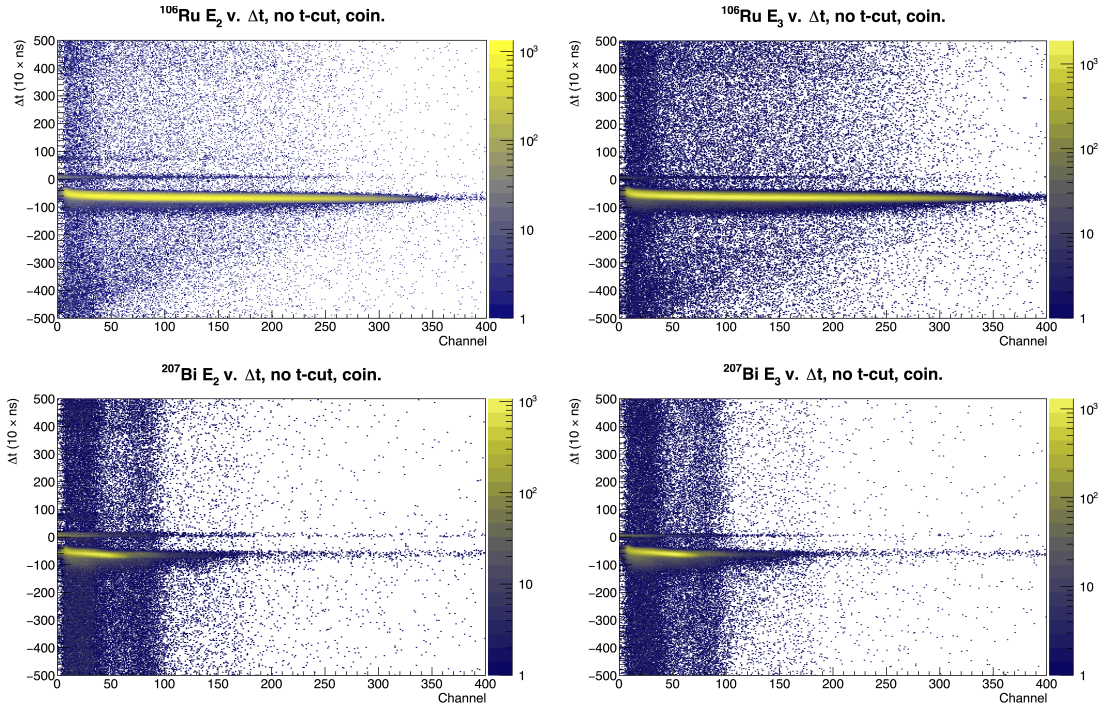

Figure 5.15: Raw Plastic coincidences from the calibration sources, detector noise, and ambient background.

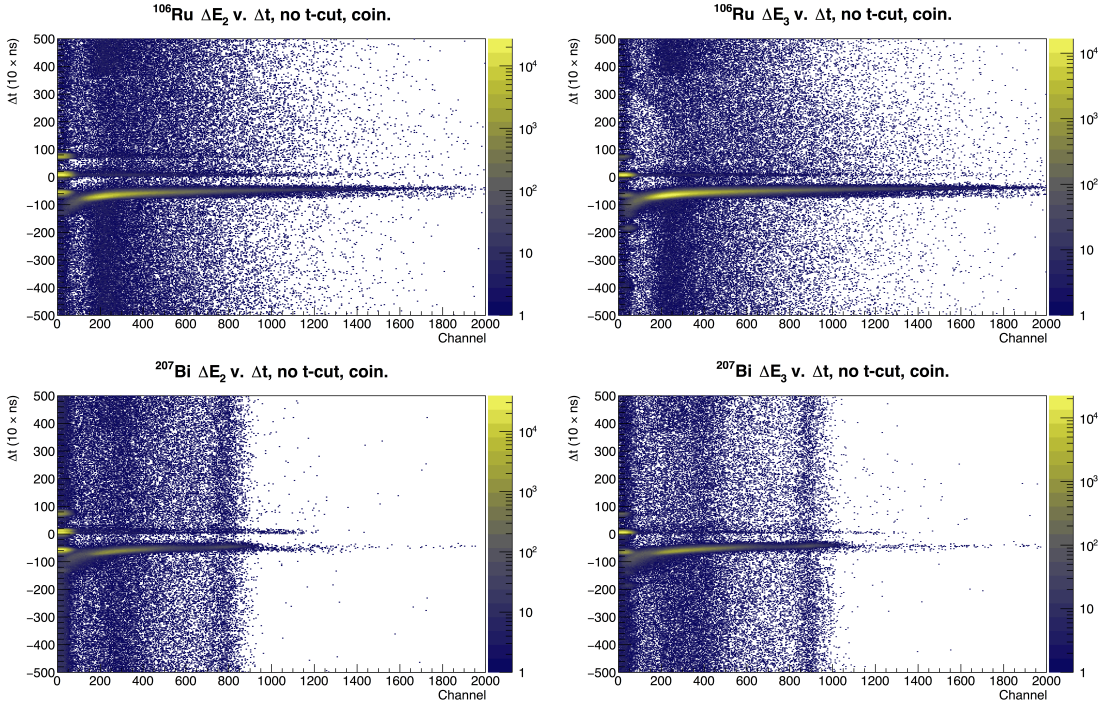

Figure 5.16: Raw silicon coincidences from the calibration sources, detector noise, and ambient background.

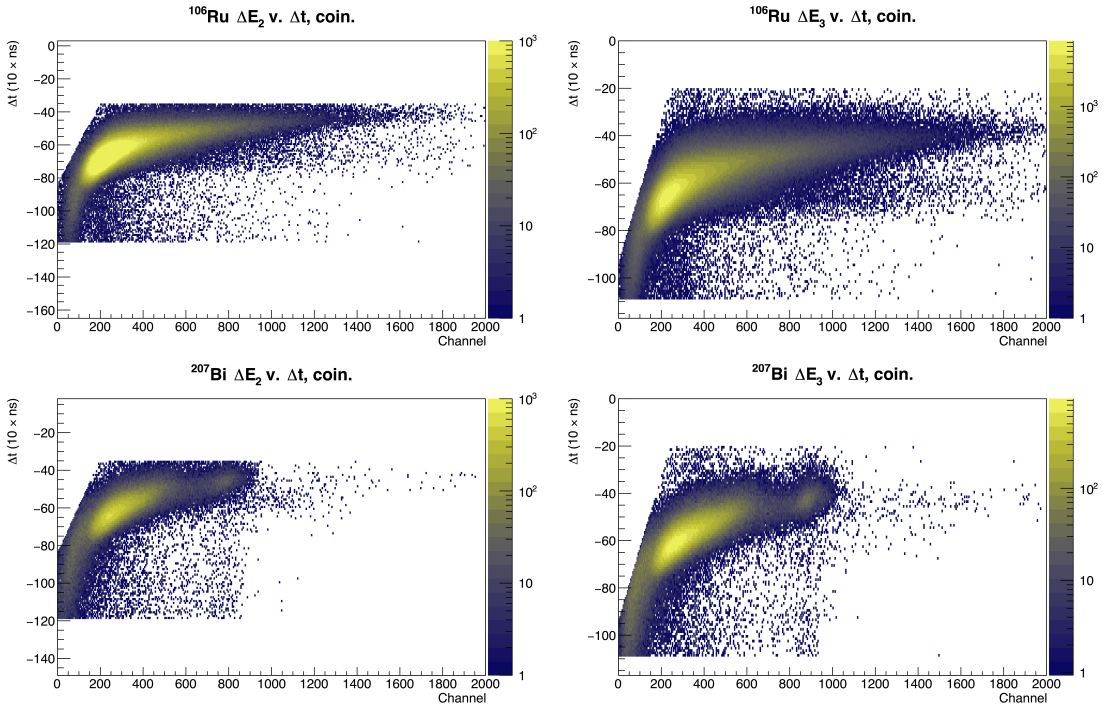

Figure 5.17: Silicon coincidences with timing cuts applied.

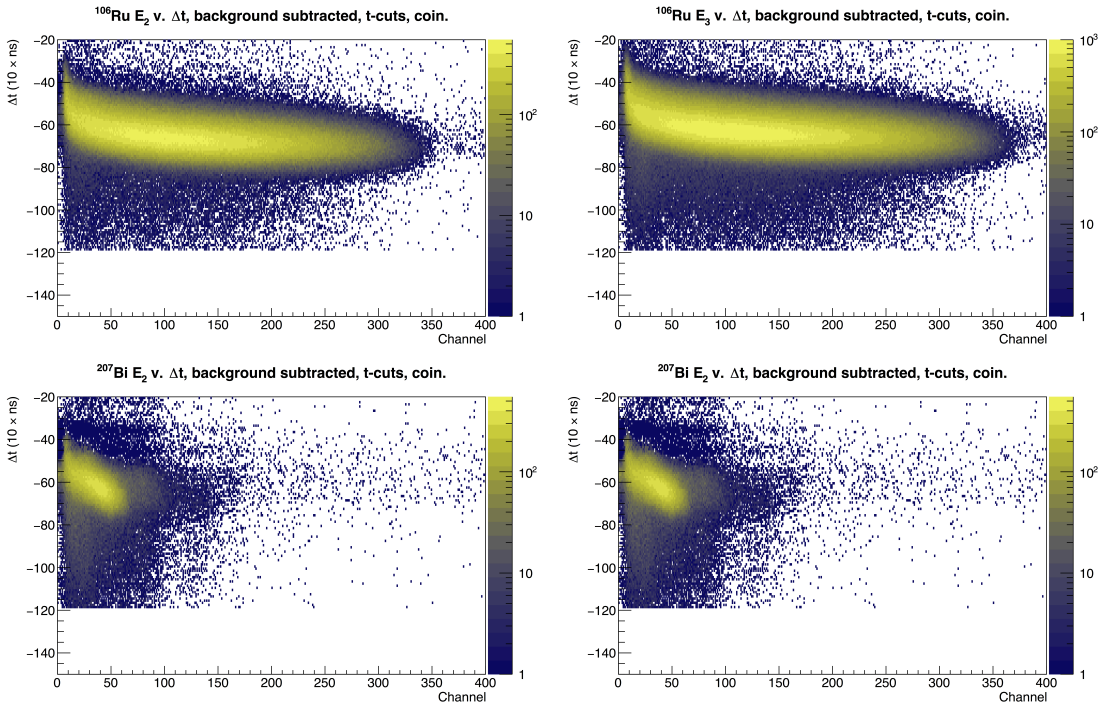

Figure 5.18: Plastic coincidences with timing cuts and background subtraction.

The net effect of the timing cuts and background subtraction is made clear when the remaining coincidences are plotted across all times 5.19. Each real timing signal now assumes a Gaussian-like shape with a mean of similar time difference with a slight distortion in the case of ^{106}Ru coincidences in Telescope 2, possibly arising from similar periodic features visible as bright spots in the lower channels in Figure 5.15 overlapping with real coincidences.

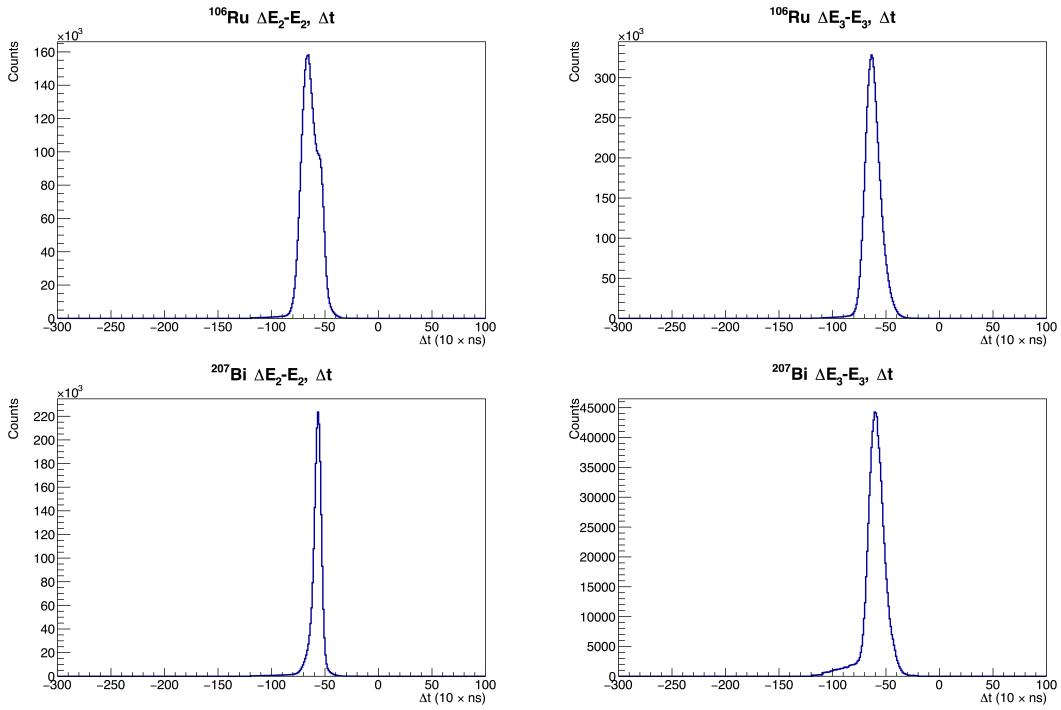

Figure 5.19: Coincidences in each telescope across all times after timing cuts and background subtraction.

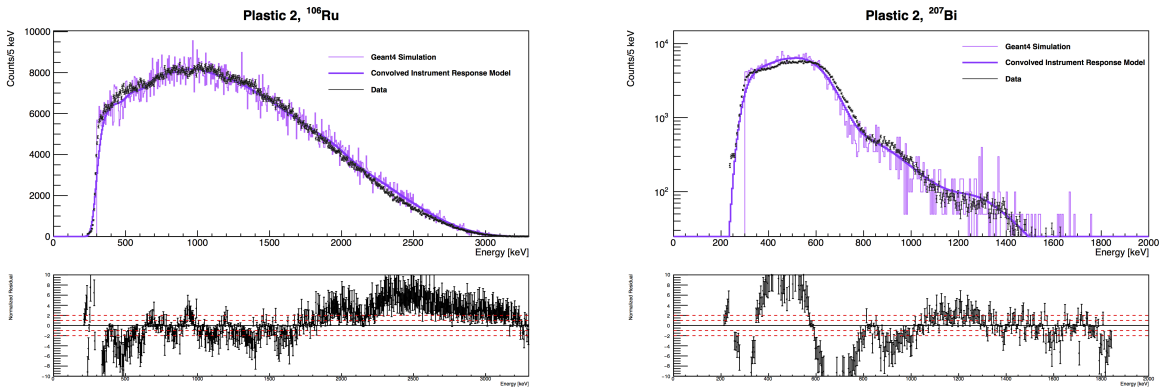

Figure 5.20: Overlaid plastic calibrations for Telescope 2 (top) and the normalized residuals between the simulation and data (bottom). The thick purple line denotes the simulated test source spectrum convolved with the model for detector response

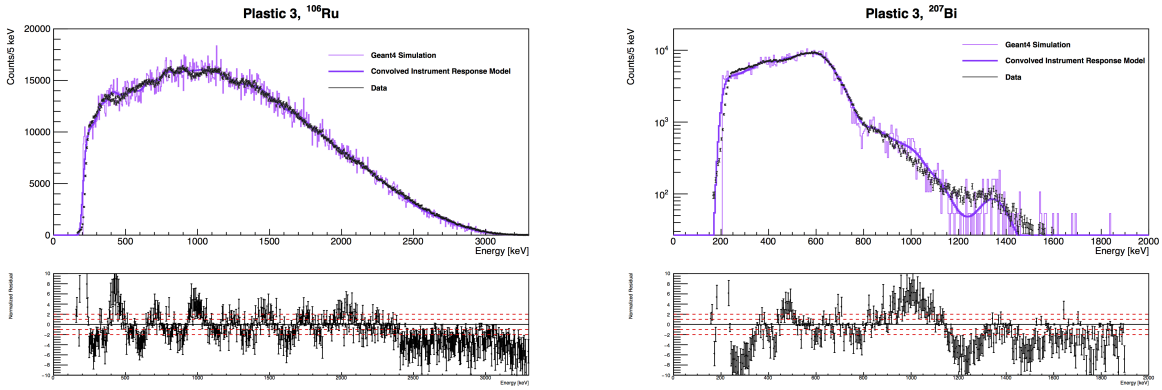

Figure 5.21: Overlaid plastic calibrations for Telescope 3 (top) and the normalized residuals between the simulation and data (bottom). The thick purple line denotes the simulated test source spectrum convolved with the model for detector response.

The cleaned spectra were calibrated from channel number to energy following the same procedure as described in Chapter 3. Figures 5.20 and 5.21 show the overlaid calibrated spectra with the simulated spectra generated using *v.3* of the Geant4 pseudo-trap model. In all cases, the simulated spectra are normalized to the data. By eye, the calibrated data generally reflect the obvious spectral features exhibited by the simulated spectra.

In the case of Telescope 2 for ^{106}Ru, the error of the normalized residuals in the region of 500 keV to 2000 keV are generally centered around zero, largely remaining within 2σ. The fit from 2000 keV through approximately 2500 keV is not as good, with the data showing a deficit in counts in that region. Near the endpoint, the fit begins to recover, again matching

the data to within 2σ. For ^{207}Bi, the fit suffers the effect of low statistics, particularly in the low-energy region below 1000 keV, where the data shows an excess of counts as compared to the simulation.

The data for Telescope 3 show better agreement with the simulated spectra. The residuals for ^{106}Ru for the most part remain within 2σ over the entire energy region, diverging somewhat toward the higher energies near the low-statistics endpoint. For ^{207}Bi, the simulated spectra matches the data more closely below 1000 keV, capturing the "shoulder" feature near 600 keV, as compared to Telescope 2.

5.4 Results

5.4.1 ^{92}Rb Beta Spectrum Measurement

For the fission products experiment run, plastic scintillator detectors on Telescopes 2 and 3 were biased at -1300 V with the preamplifiers set at 1000 pF input capacitance. The silicon detectors were biased at +100 V, with 0.5 μs pulse shaping time. Prior to the run, Telescope 4's silicon detector experienced critical failure, with breakdown occurring after applying just 0.5 V, having possibly suffered slight surface damage during installation on the pseudo-trap. Ultimately, the combination of plastic scintillator failure in Telescope 1 and silicon detector failure in Telescope 4 eliminated both telescopes from the analysis, effectively halving the run statistics.

^{92}Rb data was collected for just over 5 hours, yielding approximately 1.45M raw silicon-plastic coincidences in Telescope 3, and 1.30M raw silicon-plastic coincidences in Telescope 2.

To isolate the ^{92}Rb signal from the ^{92}Sr daughter and other background, coincident events were gated on the 20 second stationary interval of the tape movement cycle. Hits outside this window, during the 2 second period where the tape is moving, were rejected. Figure 5.22 shows coincident events in Telescopes 2 and 3 over a portion of the run duration (*top*). A smaller interval (*bottom*) reveals a sawtooth pattern of activity build up and decay over the tape duty cycle. The variation in intensity is reflective of CARIBU beam instability which affects total number of measured coincidences over the run, but does not introduce any uncertainty.

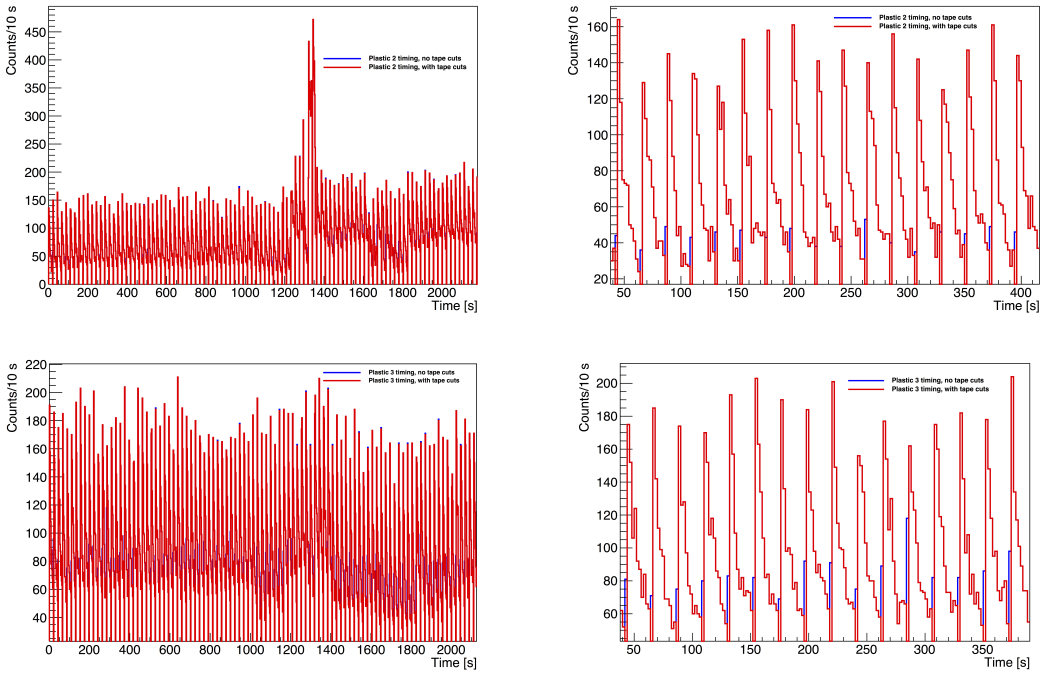

Figure 5.22: Telescope 2 (top) and Telescope 3 (bottom) coincident events over the tape cycle.

Coincidences in the tape acceptance windows were summed and fit to an exponential function with a linear offset to represent constant background using Minuit to determine the half-life of the activity. Figure 5.23 shows the decay curves and fit parameters. The calculated half-life is $t_{1/2} = 4.44$ s and $t_{1/2} = 4.43$ s for Telescopes 2 and 3, respectively. These values are

in close agreement with each other and within 5% from the reported value of 4.48 ± 0.03 s, suggesting the detected events overwhelmingly originate from the ^{92}Rb implanted source.

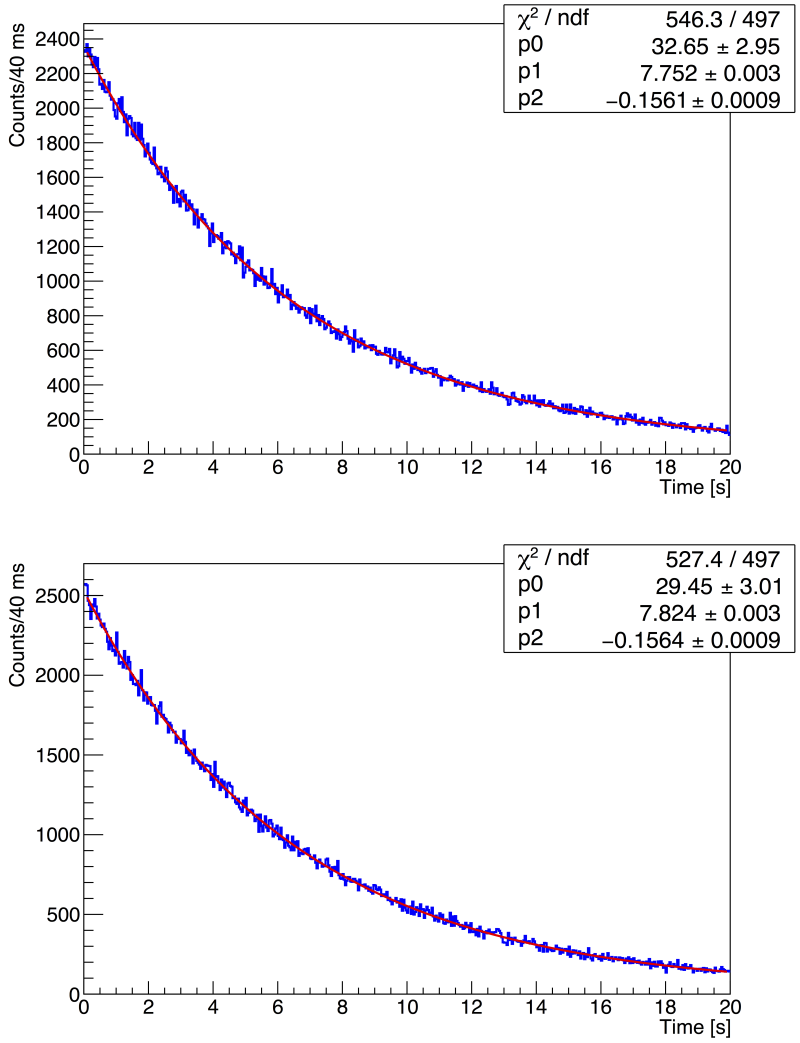

Figure 5.23: Summed coincident events over the entire ^{92}Rb data collection run with the decay curve fit (red) for Telescope 2 (top) and Telescope 3 (bottom).

The same timing cuts and channel-to-energy scaling used for the calibrations in Section 5.3.1 were applied to the ^{92}Rb data.

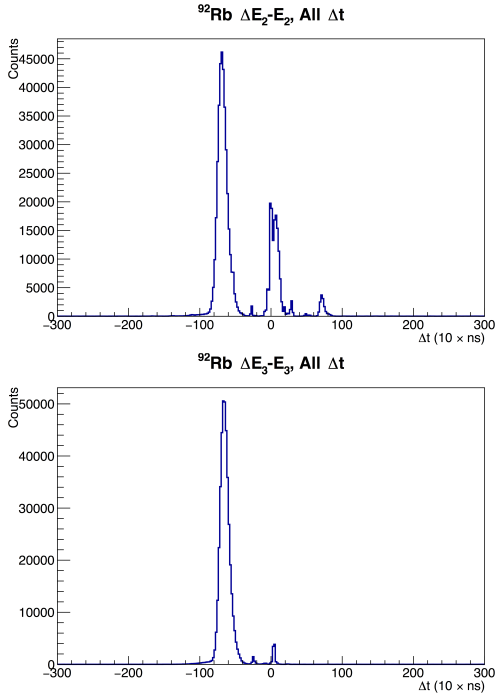

Figure 5.24: ^{92}Rb coincidences (post-tape timing cuts) across all times.

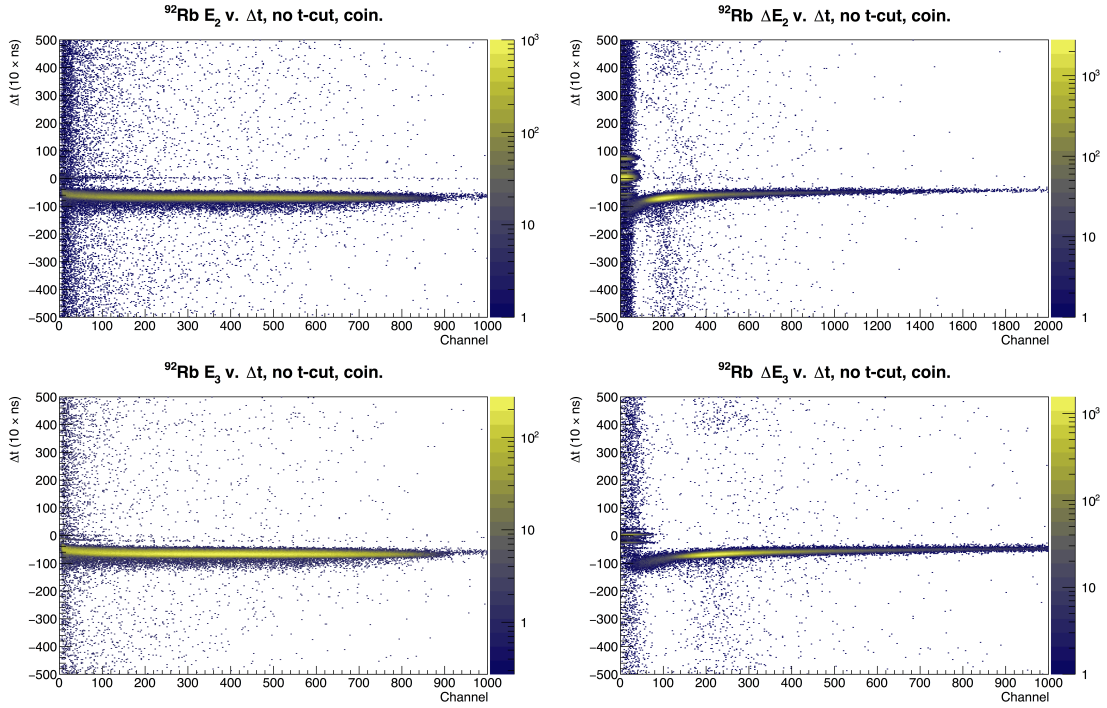

Figure 5.25: Raw ^{92}Rb plastic and silicon coincidences (post-tape timing cuts).

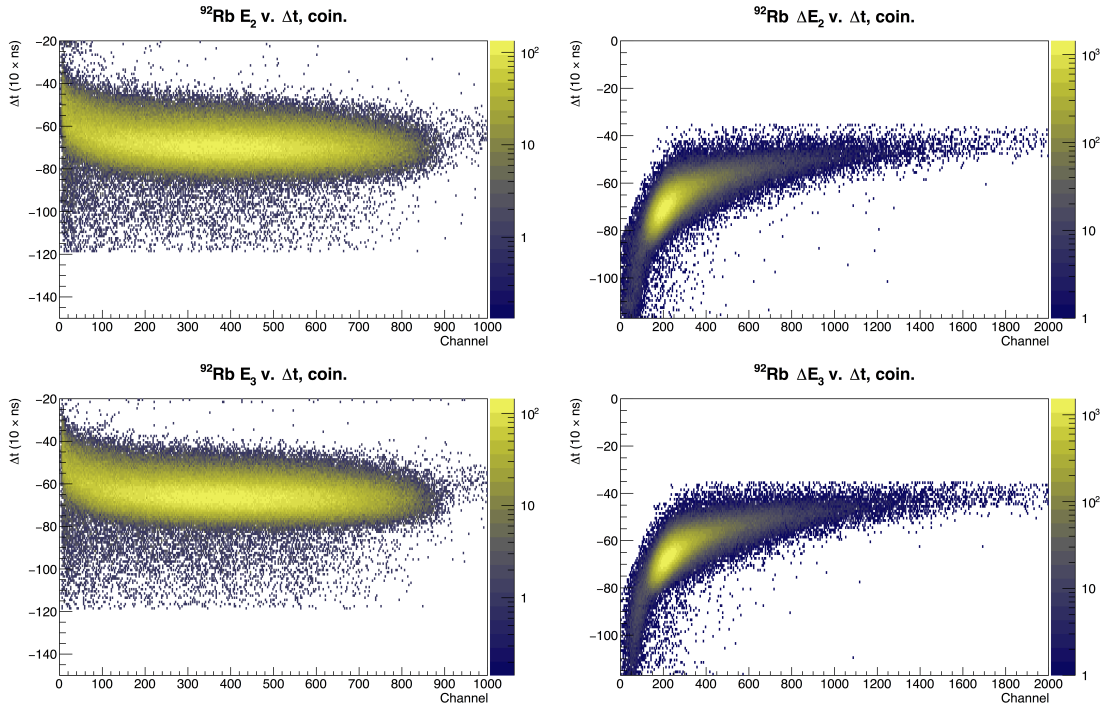

Figure 5.26: ^{92}Rb plastic and silicon coincidences for Telescope 2 (top) and Telescope 3 (bottom) with calibration timing cuts applied.

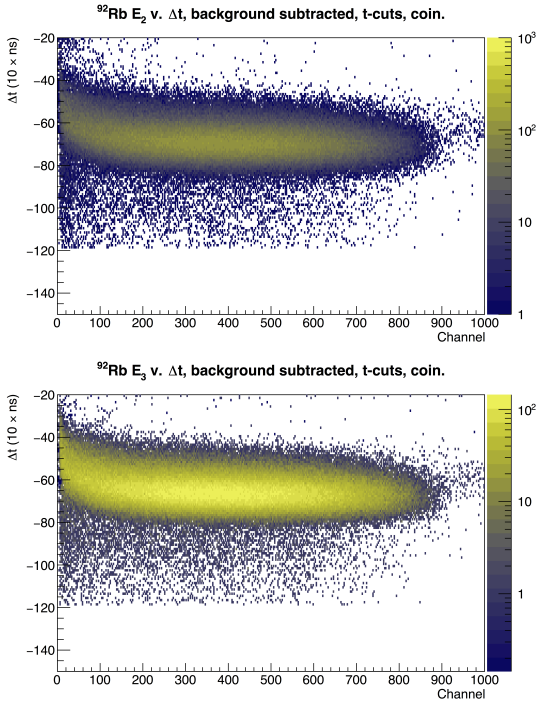

Figure 5.27: ^{92}Rb Plastic coincidences with calibration timing cuts and background subtraction.

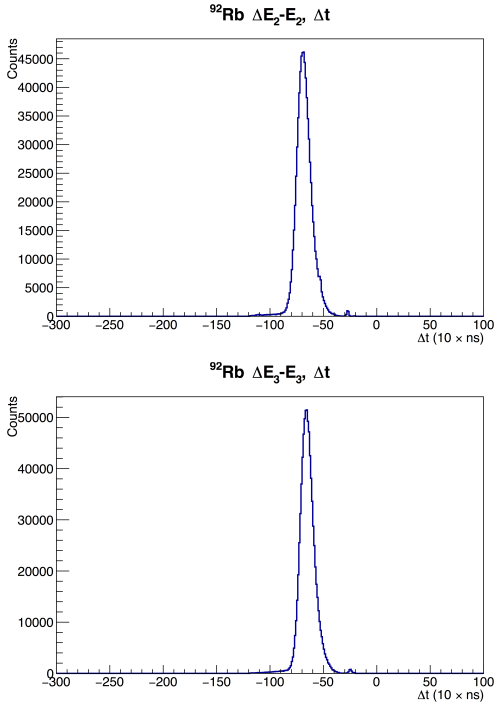

Figure 5.28: ^{92}Rb coincidences in each telescope across all times after calibration timing cuts and background subtraction.

5.4.2 A Preliminary Limit on the Weak Magnetism Slope Parameter

To generate the Geant4 input spectrum file, the BD code utilizes gamma transition information for the daughter isotope from the IAEA Nuclear Data Services library ("Reference Input Parameter Library" or "RIPL").

A "mock" RIPL file was created using results from a recent total absorption mass spectroscopy (MTAS) measurement of ^{92}Rb beta-feeding [28] to generate separate spectra assuming purely-allowed and purely-weak magnetism shape factors (Chapter 3). These input files were flown into Geant4 using *v.3* of the fission products experiment model and the resulting spectra convolved with the detector response model in the usual manner. Figures 5.29 and 5.30 show the cleaned ^{92}Rb run data overlaid with the two kinds of simulated spectra.

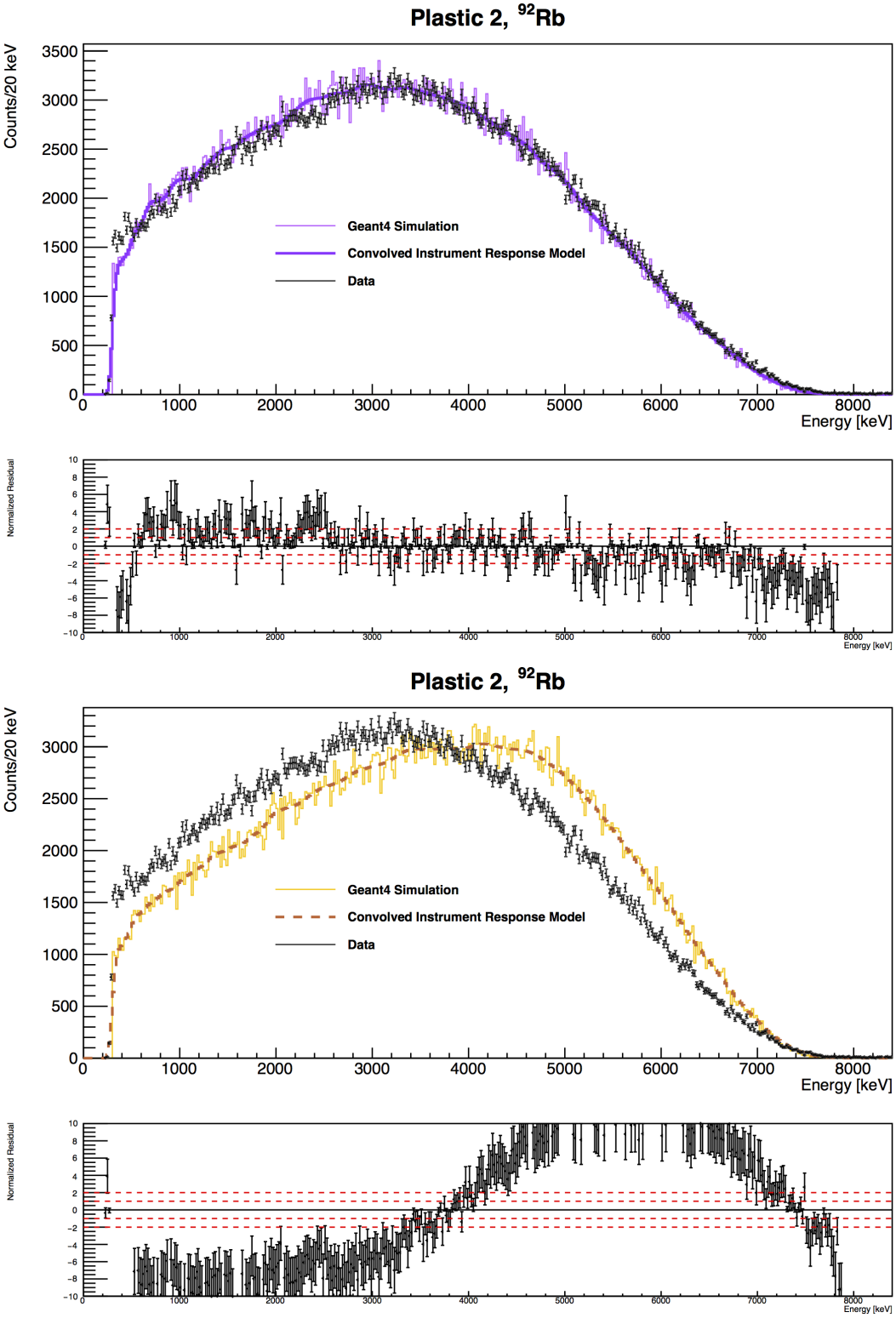

Figure 5.29: The measured data and simulated ^{92}Rb spectra assuming a "purely allowed" (top) and "purely weak magnetism" (bottom) shape factor for Telescope 2.

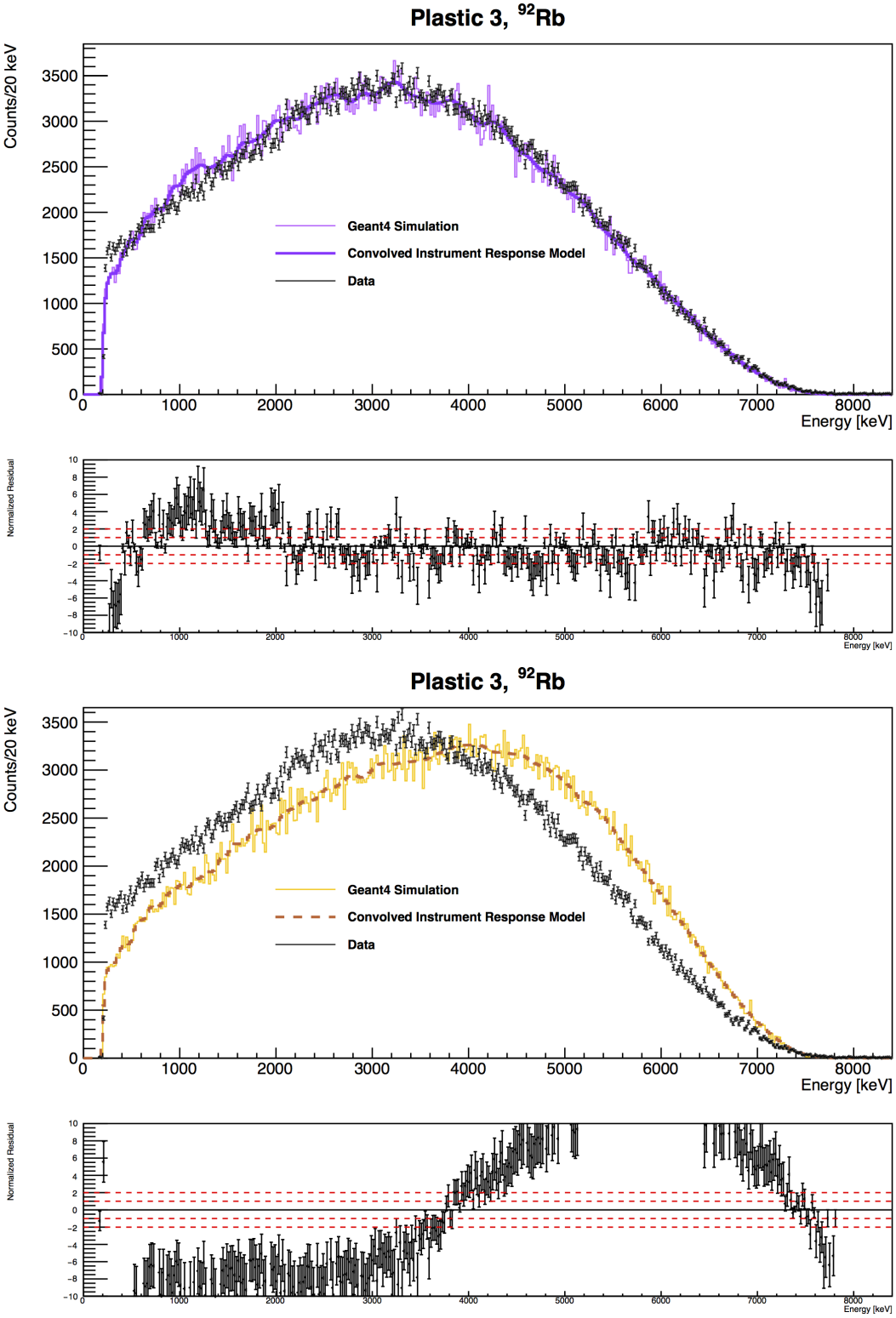

Figure 5.30: The measured data and simulated ^{92}Rb spectra assuming a "purely allowed" (top) and "purely weak magnetism" (bottom) shape factor for Telescope 3.

Examining the residuals (and quite obviously to the eye), the fit to the spectrum with a purely-allowed shape is much better than in the case of the purely-weak magnetism spectrum, consistent with the assumption that any weak magnetism contribution will be small.

As before, a fit function was constructed from a linear combination of the purely-allowed (h_{allowed}) and purely-weak magnetism ($h_{\text{weak mag.}}$) spectra:

$$f_{\text{fit}} = p_0(h_{\text{allowed}} + p_1 h_{\text{weak mag.}}) \tag{5.1}$$

and applied to the data.

Since $N_\beta(E) \propto (1 + \delta_{\text{WM}} E)$, the fit parameter p_1 relates to δ_{WM}, as

$$\delta_{\text{WM}} = \frac{p_1}{E_0} \tag{5.2}$$

where E_0, the endpoint energy, is equal to 8.6 MeV. Figure 5.31 shows the fitted spectra and their parameters and Table 5.2 lists the measured δ_{WM} for each telescope and their uncertainties.

Telescope	p_1	δ_{WM} $[\frac{\%E}{\text{MeV}}]$	$\sigma_{\delta_{\text{WM}}}$
2	0.1249	1.4519	$\pm$ 0.0007
3	0.0885	1.0287	$\pm$ 0.0008

Table 5.2: The measured δ_{WM} for ^{92}Rb.

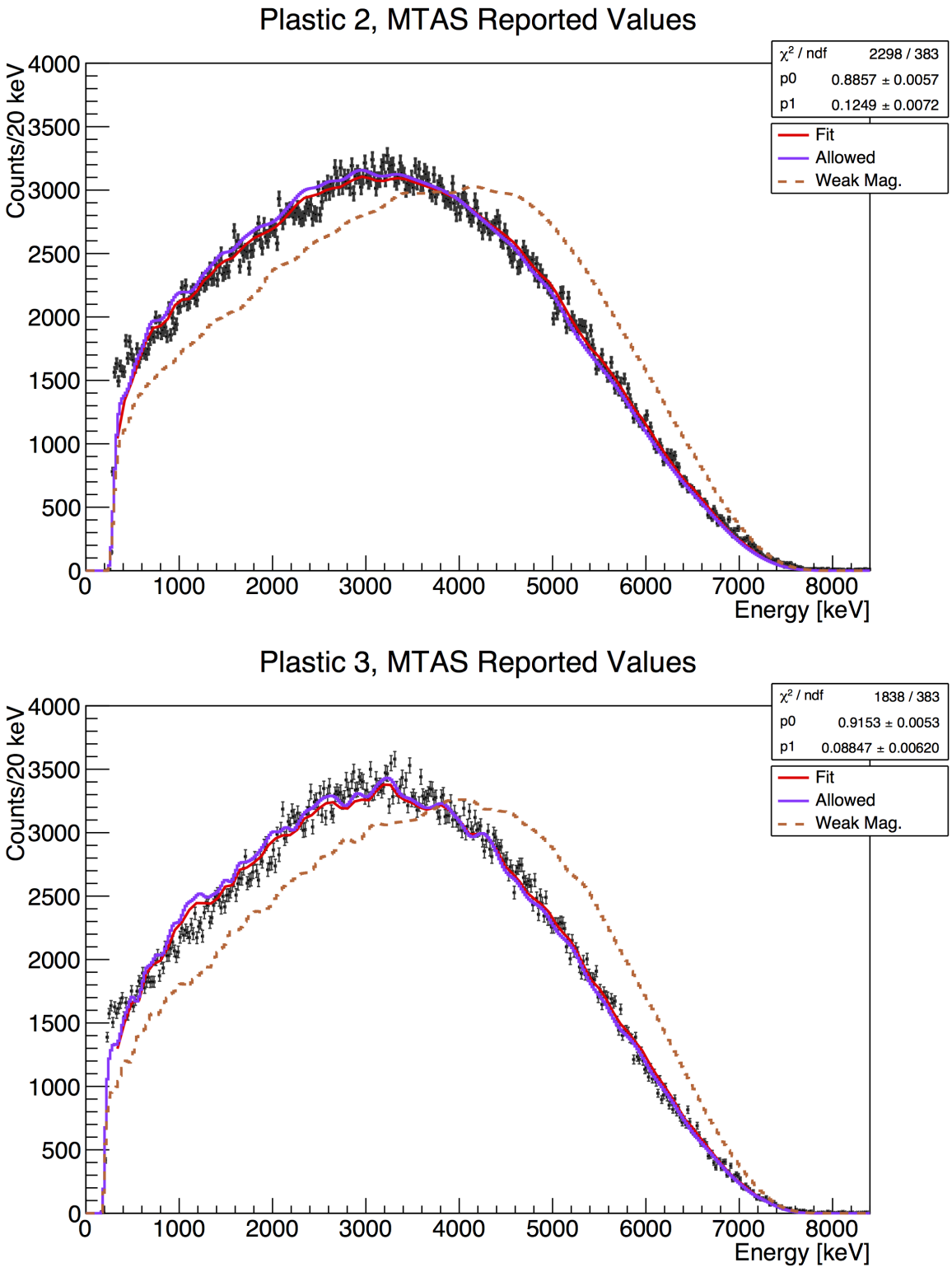

Figure 5.31: The fit ^{92}Rb spectra for Telescope 2 (top) and Telescope 3 (bottom).

Considering the difference in integral counts for silicon-gated coincidences in each telescope, weighted average for the weak magnetism slope factor is

$$\delta_{\mathrm{WM}} = 1.2333 \pm 0.0008\%E/\mathrm{MeV} \tag{5.3}$$

Figure 5.32 shows the δ_{WM} parameter space related to p_1 for each telescope. In both telescopes, the most conservative lower limit at 3σ on the measured value for δ_{WM} lies above 0.8 $\frac{\%E}{\mathrm{MeV}}$, while the upper limit is estimated to be lower than 1.8 $\frac{\%E}{\mathrm{MeV}}$ at a 99.7% confidence level.

5.4.3 Uncertainties and Systematics

Several systematic effects can introduce uncertainty on the limit on δ_{WM} in addition to that of the fit, including the ability of the simulation to model scattering within the final pseudo-trap model, variation in the channel-to-energy scaling, and misalignment of the implanted activity/calibration source placement.

Uncertainty in Simulated Scattering

The ability of the Geant4 simulation in replicating scattering was evaluated by employing the general method used in previous studies of design variation (Chapter 3). The BD code ^{92}Rb simulation input spectra for the purely-allowed and purely-weak magnetism spectra generated using the MTAS data (described in the previous section) was flown into a modified *v.3* geometry. This test model included all components from the default configuration of

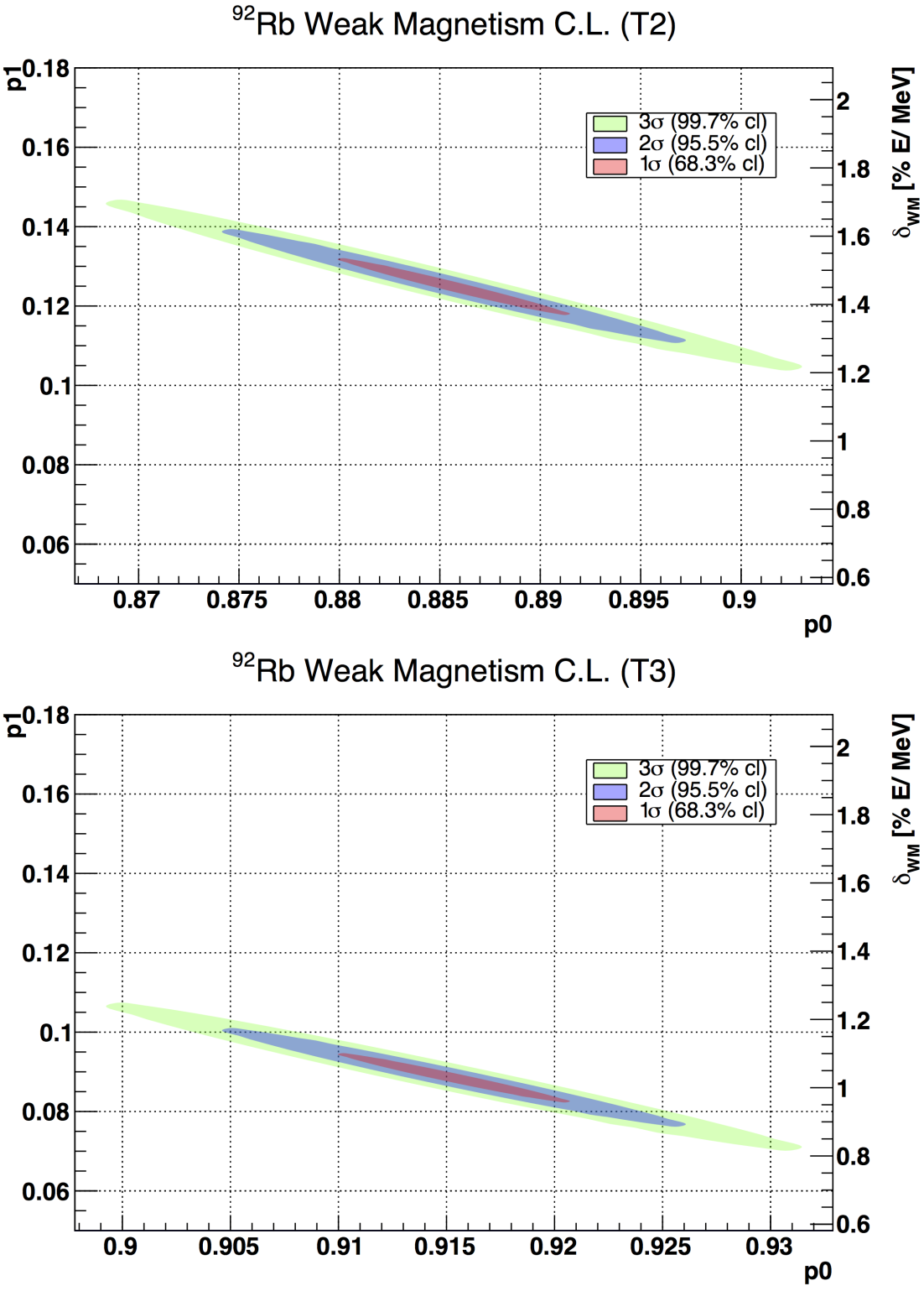

Figure 5.32: δ_{WM} confidence levels for Telescope 2 (top) and Telescope 3 (bottom).

v.3 except for the pseudo-trap frame, which accounts for the bulk of immediate scattering surfaces. Table 5.3 lists the individual δ_{WM} for both telescopes.

Telescope	p_1	δ_{WM} $[\frac{\%E}{\mathrm{MeV}}]$	$\sigma_{\delta_{\mathrm{WM}}}$
2	0.1376	1.6001	$\pm$ 0.0073
3	0.08049	0.9359	$\pm$ 0.0063

Table 5.3: The estimated δ_{WM} for ^{92}Rb with the "No Trap"-modified simulation geometry.

The weighted average for the weak magnetism slope factor using the modified geometry is

$$\delta_{\mathrm{WM}} = 1.2571 \pm 0.0073 \ \%E/\mathrm{MeV} \tag{5.4}$$

The δ_{WM} parameter spaces for each telescope using the modified geometry are shown in 5.33. In this scenario, the 3σ confidence limit placed on the measured δ_{WM} is approximately

$$\frac{0.7\%E}{\mathrm{MeV}} < \delta_{\mathrm{WM}} < \frac{1.9\%E}{\mathrm{MeV}}$$

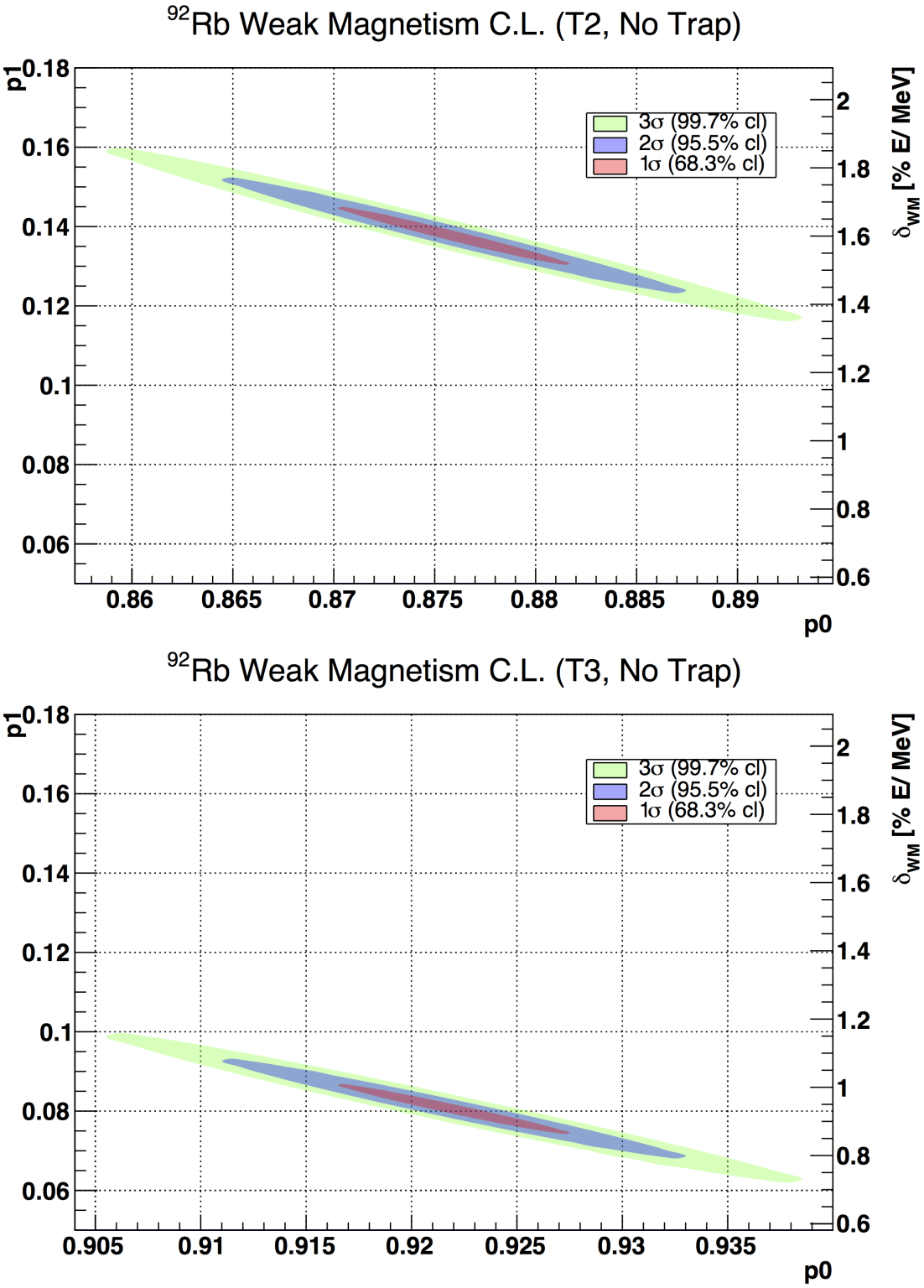

Figure 5.33: δ_{WM} confidence levels for Telescope 2 (top) and Telescope 3 (bottom) with the "No Trap"-modified simulation geometry.

Comparing the weighted averages for δ_{WM} from the two scenarios (values 5.4.2 and 5.4.3), the contribution to the overall uncertainty introduced by Geant4's accuracy in modeling electron scattering will be set at

$$\sigma_{scattering} = 0.0168 \tag{5.5}$$

Uncertainty in Source Placement

The effect of source misalignment on the measurement of a weak magnetism correction was evaluated in 3.2.1. Extreme variation in placement (±5 mm in each direction on the tape) set an uncertainty of

$$\sigma_{misalign.} = 0.0014 \tag{5.6}$$

Uncertainty in Calibration Scaling

Changes in the calibration scaling factor of 1% were considered for both telescopes. The $\sigma_{cal.}$ for each telescope, computed from the standard deviation in δ_{WM}, was found to be approximately

$$\sigma_{cal.} = 0.2 \tag{5.7}$$

The total uncertainty in δ_{WM}, given by

$\sigma_{tot.} = \sigma_{fit} + \sigma_{scattering} + \sigma_{misalign.} + \sigma_{cal.}$

is clearly dominated by $\sigma_{cal.}$.

Therefore, the final estimate of the weak magnetism correction to the beta spectrum is

$$\delta_{\mathrm{WM}} = 1.2333 \pm 0.2\% E/\mathrm{MeV}. \tag{5.8}$$

5.5 Discussion and Conclusion

The impact on the statistics in each telescope due to removal of the tape collimators from the fission products pseudo-trap was evaluated by simulating monoenergetic, isotropic electron sources with the changed design. The difference in the number of detected events between simulations, with and without the tape collimators, was found to be small over the majority of the energy region studied (Figure 5.8).

The channel-to-energy calibration of the plastic scintillator detectors was determined by comparing spectra from test sources recorded at the time of the run to simulated spectra generated using an updated, highly-detailed model of the trap (Figures 5.20 and 5.21). The purity of the implanted ^{92}Rb source was established with a half-life measurement by imposing timing cuts using tape station signal information (Figure 5.23), and the data was calibrated using the test source information.

The weak magnetism correction for each telescope was extracted by fitting a combination of simulated ^{92}Rb purely allowed and purely weak magnetism spectra (Figure 5.31) to the calibrated data. The weak magnetism correction was found to be between 0.7 $\%E$/MeV and 2 $\%E$/MeV at 3σ confidence (Figure 5.32). Uncertainty in the weak magnetism correction was determined by assessing scattering effects in the simulation, misalignment in the source position, and changes in the calibration. Including this, the weak magnetism correction to the ^{92}Rb beta spectrum was found to be $\delta_{\mathrm{WM}} = 1.2333 \pm 0.2\%E/\mathrm{MeV}$.

Chapter 6

Conclusion and Future Work

6.1 Conclusion

This work has presented the development and testing of a new ΔE - E telescope array for fission fragment beta spectroscopy deployed at Argonne National Laboratory's CARIBU user facility. The array is comprised of four plastic scintillator detectors and corresponding silicon detectors mounted to a "pseudo-trap" with a design based on that used in a ^{8}Li ion trap experiment (the Beta Paul Trap, or BPT) at ANL's ATLAS facility. Fission fragment activity from CARIBU is deposited on a transport tape that is fed through the pseudo-trap, yielding a ^{92}Rb source with minimal background from daughter products.

An overview of Geant4, the framework used in simulations of the fission products experiment, was provided. These simulations allowed for evaluation of the impact of design changes to the fission products experiment in pre-experimental run feasibility studies. Simulations of design changes from the default geometry (inspired by the BPT), such as the addition of the transport tape (absent in the BPT), were performed. These studies showed the impact of these changes on the magnitude of the weak magnetism correction to be small. The

uncertainty on the weak magnetism correction introduced by misalignment in position of the implanted source was found to be $\sigma_{\text{misalign.}} = 0.0014$.

The simulations model of the experiment was altered to better match the design of the BPT. A high-statistics measurement of the ^{8}Li spectrum at the BPT was used to characterize the previously untested plastic scintillator detectors used in the fission products experiment. The effect of gain changes on performance of the plastic scintillator detector PMTs was studied using blue LEDs embedded in the scintillator material. These changes were found to be small over durations larger than the intended fission products experimental run. The spectral data from the ^{8}Li measurement was found to be in close agreement with the updated simulation. Utilizing information from the double sided strip detectors used in the ^{8}Li experiment and simulated spectra, the response of the plastic scintillator detectors was found to be largely uniform across the face of the detector. The simulation, eventually adapted to match the layout of the fission products experiment and used in determining the weak magnetism correction in ^{92}Rb, was found to accurately model the ^{8}Li spectrum measured at the BPT.

Simulations reflecting a final design change to the fission products experiment (the removal of the tape collimators) were performed and no significant contribution to the weak magnetism correction was found. The beta spectrum of ^{92}Rb, one of the most important contributors to the aggregate ^{235}U spectrum in the 4 to 6 MeV energy region of the so-called reactor neutrino spectrum shoulder, was measured. The inaugural run of the detector array measured approximately 1.5M silicon-plastic coincidences from ^{92}Rb decay. The ^{92}Rb spectrum was calibrated by comparing spectra of test sources measured at the time of the run to simulations using the most accurate, comprehensive Geant4 model of the detector array. A half-life measurement of the implanted source ($t_{1/2} = 4.44$ s) was found to be in reasonable agreement with the reported value ($t_{1/2} = 4.48 \pm 0.03$ s), suggesting the overwhelming majority of events detected in the telescopes were from ^{92}Rb beta decay. The weak magnetism correction was found to be between 0.7 $\%E$/MeV and 2 $\%E$/MeV at 3σ confidence (Figure

5.32). Uncertainty in the ability of the simulation to reproduce scattering effects in the measurement was found to be $\sigma_{scattering} = 0.0168$.

An estimate of the weak magnetism correction to the ^{92}Rb beta spectrum calculation was found to be $\delta_{\mathrm{WM}} = 1.2333 \pm 0.2\% E/\mathrm{MeV}$.

6.2 Future Studies

The weak magnetism correction found in this work is larger than current estimates that assume an effect comparable to that of light nuclei, currently set at $\delta_{\mathrm{WM}} = 0.5\% E/\mathrm{MeV}$. This result further calls into question the validity of assumptions regarding the spectral shape used in the calculation of reactor antineutrino spectra.

Measurement of ground state-ground state beta-feeding intensities using γ HPGe information collected at the time of the run may allow for further refinement of the weak magnetism correction estimate. These beta-feeding measurements will serve as an important check against the most recently reported results from MTAS experiments used in the simulations discussed in this work.

A similar study of the ^{96}Y beta spectrum, the second largest contributor to the ^{235}U spectrum (Figure 1.2), will be useful in establishing the importance of the weak magnetism, or other shape factor corrections, in calculations of the aggregate spectrum. Taken together, ^{92}Rb and ^{96}Y contribute approximately 36% of the total counts around 5 MeV, possibly accounting for the local excess of neutrinos relative to the conversion method calculations. CARIBU is capable of delivering ^{96}Sr (which decays to ^{96}Y) beams with an intensity of approximately 2.4×10^4 ions/s. Production of ^{96}Sr has the benefit of avoiding complicated background originating from the population of the ^{96m}Y isomer, arising from the direct decay of ^{96}Y. The background of the isomer could otherwise be difficult to de-tangle from a ^{96}Y signal,

as it has a similar half-life to ^{96}Y and a larger yield in ^{252}Cf. Higher statistics may also be achievable over the same run duration, as ^{96}Sr has an order of magnitude larger spontaneous fission yield.

While not a major contributor to the aggregate ^{235}U spectrum, ^{136}Sb, may also provide compelling evidence as to the significance of the effect of shape factor corrections on first-forbidden decays (like ^{92}Rb and ^{96}Y). ^{136}Sb decays to the ground state of ^{136}Te, with a branching ratio of approximately 60% and is thought to have a significant shape factor correction.

Clearly, an additional two working telescopes would not only provide higher statistics (thereby reducing statistical uncertainty in the weak magnetism correction fit), but would also improve calibrations. Future iterations of the fission products experiment might also benefit from the kind of position information afforded by DSSDs to further confirm the origin of signals detected in the telescopes, or permit different types of electroweak interaction studies.

Regardless, a number of fission fragment beta spectra are presently not well-understood and would benefit from further investigation using a variety of experiments. New techniques, such as the direct beta decay measurement presented in this work, provide a novel means to study nuclear structure and investigate outstanding questions concerning the universe's most fundamental constituents.

Bibliography

[1] M. G. Aartsen, K. Abraham, M. Ackermann, J. Adams, J. A. Aguilar, M. Ahlers, M. Ahrens, D. Altmann, K. Andeen, T. Anderson, I. Ansseau, G. Anton, M. Archinger, C. Argüelles, T. C. Arlen, J. Auffenberg, S. Axani, X. Bai, S. W. Barwick, V. Baum, R. Bay, J. J. Beatty, J. Becker Tjus, K.-H. Becker, S. BenZvi, P. Berghaus, D. Berley, E. Bernardini, A. Bernhard, D. Z. Besson, G. Binder, D. Bindig, E. Blaufuss, S. Blot, D. J. Boersma, C. Bohm, M. Börner, F. Bos, D. Bose, S. Böser, O. Botner, J. Braun, L. Brayeur, H.-P. Bretz, A. Burgman, J. Casey, M. Casier, E. Cheung, D. Chirkin, A. Christov, K. Clark, L. Classen, S. Coenders, G. H. Collin, J. M. Conrad, D. F. Cowen, A. H. Cruz Silva, J. Daughhetee, J. C. Davis, M. Day, J. P. A. M. de André, C. De Clercq, E. del Pino Rosendo, H. Dembinski, S. De Ridder, P. Desiati, K. D. de Vries, G. de Wasseige, M. de With, T. DeYoung, J. C. Díaz-Vélez, V. di Lorenzo, H. Dujmovic, J. P. Dumm, M. Dunkman, B. Eberhardt, T. Ehrhardt, B. Eichmann, S. Euler, P. A. Evenson, S. Fahey, A. R. Fazely, J. Feintzeig, J. Felde, K. Filimonov, C. Finley, S. Flis, C.-C. Fösig, T. Fuchs, T. K. Gaisser, R. Gaior, J. Gallagher, L. Gerhardt, K. Ghorbani, W. Giang, L. Gladstone, T. Glüsenkamp, A. Goldschmidt, G. Golup, J. G. Gonzalez, D. Góra, D. Grant, Z. Griffith, A. Haj Ismail, A. Hallgren, F. Halzen, E. Hansen, K. Hanson, D. Hebecker, D. Heereman, K. Helbing, R. Hellauer, S. Hickford, J. Hignight, G. C. Hill, K. D. Hoffman, R. Hoffmann, K. Holzapfel, A. Homeier, K. Hoshina, F. Huang, M. Huber, W. Huelsnitz, K. Hultqvist, S. In, A. Ishihara, E. Jacobi, G. S. Japaridze, M. Jeong, K. Jero, B. J. P. Jones, M. Jurkovic, A. Kappes, T. Karg, A. Karle, U. Katz, M. Kauer, A. Keivani, J. L. Kelley, A. Kheirandish, M. Kim, T. Kintscher, J. Kiryluk, T. Kittler, S. R. Klein, G. Kohnen, R. Koirala, H. Kolanoski, L. Köpke, C. Kopper, S. Kopper, D. J. Koskinen, M. Kowalski, K. Krings, M. Kroll, G. Krückl, C. Krüger, J. Kunnen, S. Kunwar, N. Kurahashi, T. Kuwabara, M. Labare, J. L. Lanfranchi, M. J. Larson, D. Lennarz, M. Lesiak-Bzdak, M. Leuermann, L. Lu, J. Lünemann, J. Madsen, G. Maggi, K. B. M. Mahn, S. Mancina, M. Mandelartz, R. Maruyama, K. Mase, R. Maunu, F. McNally, K. Meagher, M. Medici, M. Meier, A. Meli, T. Menne, G. Merino, T. Meures, S. Miarecki, E. Middell, L. Mohrmann, T. Montaruli, M. Moulai, R. Nahnhauer, U. Naumann, G. Neer, H. Niederhausen, S. C. Nowicki, D. R. Nygren, A. Obertacke Pollmann, A. Olivas, A. Omairat, A. O'Murchadha, T. Palczewski, H. Pandya, D. V. Pankova, J. A. Pepper, C. Pérez de los Heros, C. Pfendner, D. Pieloth, E. Pinat, J. Posselt, P. B. Price, G. T. Przybylski, M. Quinnan, C. Raab, M. Rameez, K. Rawlins, M. Relich, E. Resconi, W. Rhode, M. Richman, B. Riedel, S. Robertson, C. Rott, T. Ruhe, D. Ryckbosch, D. Rysewyk, L. Sabbatini, J. Salvado, S. E. Sanchez Herrera, A. San-

drock, J. Sandroos, S. Sarkar, K. Satalecka, P. Schlunder, T. Schmidt, S. Schöneberg, A. Schönwald, D. Seckel, S. Seunarine, D. Soldin, M. Song, G. M. Spiczak, C. Spiering, M. Stamatikos, T. Stanev, A. Stasik, A. Steuer, T. Stezelberger, R. G. Stokstad, A. Stößl, R. Ström, N. L. Strotjohann, G. W. Sullivan, M. Sutherland, H. Taavola, I. Taboada, J. Tatar, S. Ter-Antonyan, A. Terliuk, G. Tešić, S. Tilav, P. A. Toale, M. N. Tobin, S. Toscano, D. Tosi, M. Tselengidou, A. Turcati, E. Unger, M. Usner, S. Vallecorsa, J. Vandenbroucke, N. van Eijndhoven, S. Vanheule, M. van Rossem, J. van Santen, J. Veenkamp, M. Voge, M. Vraeghe, C. Walck, A. Wallace, N. Wandkowsky, C. Weaver, C. Wendt, S. Westerhoff, B. J. Whelan, K. Wiebe, L. Wille, D. R. Williams, L. Wills, H. Wissing, M. Wolf, T. R. Wood, E. Woolsey, K. Woschnagg, D. L. Xu, X. W. Xu, Y. Xu, J. P. Yanez, G. Yodh, S. Yoshida, and M. Zoll. Searches for sterile neutrinos with the icecube detector. *Phys. Rev. Lett.*, 117:071801, Aug 2016.

[2] Y. Abe, C. Aberle, T. Akiri, J. C. dos Anjos, F. Ardellier, A. F. Barbosa, A. Baxter, M. Bergevin, A. Bernstein, T. J. C. Bezerra, L. Bezrukhov, E. Blucher, M. Bongrand, N. S. Bowden, C. Buck, J. Busenitz, A. Cabrera, E. Caden, L. Camilleri, R. Carr, M. Cerrada, P.-J. Chang, P. Chimenti, T. Classen, A. P. Collin, E. Conover, J. M. Conrad, S. Cormon, J. I. Crespo-Anadón, M. Cribier, K. Crum, A. Cucoanes, M. V. D'Agostino, E. Damon, J. V. Dawson, S. Dazeley, M. Dierckxsens, D. Dietrich, Z. Djurcic, M. Dracos, V. Durand, Y. Efremenko, M. Elnimr, Y. Endo, A. Etenko, E. Falk, M. Fallot, M. Fechner, F. von Feilitzsch, J. Felde, S. M. Fernandes, D. Franco, A. J. Franke, M. Franke, H. Furuta, R. Gama, I. Gil-Botella, L. Giot, M. Göger-Neff, L. F. G. Gonzalez, M. C. Goodman, J. T. Goon, D. Greiner, B. Guillon, N. Haag, C. Hagner, T. Hara, F. X. Hartmann, J. Hartnell, T. Haruna, J. Haser, A. Hatzikoutelis, T. Hayakawa, M. Hofmann, G. A. Horton-Smith, M. Ishitsuka, J. Jochum, C. Jollet, C. L. Jones, F. Kaether, L. Kalousis, Y. Kamyshkov, D. M. Kaplan, T. Kawasaki, G. Keefer, E. Kemp, H. de Kerret, Y. Kibe, T. Konno, D. Kryn, M. Kuze, T. Lachenmaier, C. E. Lane, C. Langbrandtner, T. Lasserre, A. Letourneau, D. Lhuillier, H. P. Lima, M. Lindner, Y. Liu, J. M. López-Castanõ, J. M. LoSecco, B. K. Lubsandorzhiev, S. Lucht, D. McKee, J. Maeda, C. N. Maesano, C. Mariani, J. Maricic, J. Martino, T. Matsubara, G. Mention, A. Meregaglia, T. Miletic, R. Milincic, A. Milzstajn, H. Miyata, D. Motta, T. A. Mueller, Y. Nagasaka, K. Nakajima, P. Novella, M. Obolensky, L. Oberauer, A. Onillon, A. Osborn, I. Ostrovskiy, C. Palomares, S. J. M. Peeters, I. M. Pepe, S. Perasso, P. Perrin, P. Pfahler, A. Porta, W. Potzel, R. Queval, J. Reichenbacher, B. Reinhold, A. Remoto, D. Reyna, M. Röhling, S. Roth, H. A. Rubin, Y. Sakamoto, R. Santorelli, F. Sato, S. Schönert, S. Schoppmann, U. Schwan, T. Schwetz, M. H. Shaevitz, D. Shrestha, J.-L. Sida, V. Sinev, M. Skorokhvatov, E. Smith, J. Spitz, A. Stahl, I. Stancu, M. Strait, A. Stüken, F. Suekane, S. Sukhotin, T. Sumiyoshi, Y. Sun, Z. Sun, R. Svoboda, H. Tabata, N. Tamura, K. Terao, A. Tonazzo, M. Toups, H. H. Trinh Thi, C. Veyssiere, S. Wagner, H. Watanabe, B. White, C. Wiebusch, L. Winslow, M. Worcester, M. Wurm, E. Yanovitch, F. Yermia, K. Zbiri, and V. Zimmer. Indication of reactor $\overline{\nu}_e$ disappearance in the double chooz experiment. *Phys. Rev. Lett.*, 108:131801, Mar 2012.

[3] Y. Abe et al. Reactor electron antineutrino disappearance in the Double Chooz experiment. *Phys. Rev.*, D86:052008, 2012.

[4] P. Adamson, F. P. An, I. Anghel, A. Aurisano, A. B. Balantekin, H. R. Band, G. Barr, M. Bishai, A. Blake, S. Blyth, G. J. Bock, D. Bogert, D. Cao, G. F. Cao, J. Cao, S. V. Cao, T. J. Carroll, C. M. Castromonte, W. R. Cen, Y. L. Chan, J. F. Chang, L. C. Chang, Y. Chang, H. S. Chen, Q. Y. Chen, R. Chen, S. M. Chen, Y. Chen, Y. X. Chen, J. Cheng, J.-H. Cheng, Y. P. Cheng, Z. K. Cheng, J. J. Cherwinka, S. Childress, M. C. Chu, A. Chukanov, J. A. B. Coelho, L. Corwin, D. Cronin-Hennessy, J. P. Cummings, J. de Arcos, S. De Rijck, Z. Y. Deng, A. V. Devan, N. E. Devenish, X. F. Ding, Y. Y. Ding, M. V. Diwan, M. Dolgareva, J. Dove, D. A. Dwyer, W. R. Edwards, C. O. Escobar, J. J. Evans, E. Falk, G. J. Feldman, W. Flanagan, M. V. Frohne, M. Gabrielyan, H. R. Gallagher, S. Germani, R. Gill, R. A. Gomes, M. Gonchar, G. H. Gong, H. Gong, M. C. Goodman, P. Gouffon, N. Graf, R. Gran, M. Grassi, K. Grzelak, W. Q. Gu, M. Y. Guan, L. Guo, R. P. Guo, X. H. Guo, Z. Guo, A. Habig, R. W. Hackenburg, S. R. Hahn, R. Han, S. Hans, J. Hartnell, R. Hatcher, M. He, K. M. Heeger, Y. K. Heng, A. Higuera, A. Holin, Y. K. Hor, Y. B. Hsiung, B. Z. Hu, T. Hu, W. Hu, E. C. Huang, H. X. Huang, J. Huang, X. T. Huang, P. Huber, W. Huo, G. Hussain, J. Hylen, G. M. Irwin, Z. Isvan, D. E. Jaffe, P. Jaffke, C. James, K. L. Jen, D. Jensen, S. Jetter, X. L. Ji, X. P. Ji, J. B. Jiao, R. A. Johnson, J. K. de Jong, J. Joshi, T. Kafka, L. Kang, S. M. S. Kasahara, S. H. Kettell, S. Kohn, G. Koizumi, M. Kordosky, M. Kramer, A. Kreymer, K. K. Kwan, M. W. Kwok, T. Kwok, K. Lang, T. J. Langford, K. Lau, L. Lebanowski, J. Lee, J. H. C. Lee, R. T. Lei, R. Leitner, J. K. C. Leung, C. Li, D. J. Li, F. Li, G. S. Li, Q. J. Li, S. Li, S. C. Li, W. D. Li, X. N. Li, Y. F. Li, Z. B. Li, H. Liang, C. J. Lin, G. L. Lin, S. Lin, S. K. Lin, Y.-C. Lin, J. J. Ling, J. M. Link, P. J. Litchfield, L. Littenberg, B. R. Littlejohn, D. W. Liu, J. C. Liu, J. L. Liu, C. W. Loh, C. Lu, H. Q. Lu, J. S. Lu, P. Lucas, K. B. Luk, Z. Lv, Q. M. Ma, X. B. Ma, X. Y. Ma, Y. Q. Ma, Y. Malyshkin, W. A. Mann, M. L. Marshak, D. A. Martinez Caicedo, N. Mayer, K. T. McDonald, C. McGivern, R. D. McKeown, M. M. Medeiros, R. Mehdiyev, J. R. Meier, M. D. Messier, W. H. Miller, S. R. Mishra, I. Mitchell, M. Mooney, C. D. Moore, L. Mualem, J. Musser, Y. Nakajima, D. Naples, J. Napolitano, D. Naumov, E. Naumova, J. K. Nelson, H. B. Newman, H. Y. Ngai, R. J. Nichol, Z. Ning, J. A. Nowak, J. O'Connor, J. P. Ochoa-Ricoux, A. Olshevskiy, M. Orchanian, R. B. Pahlka, J. Paley, H.-R. Pan, J. Park, R. B. Patterson, S. Patton, G. Pawloski, V. Pec, J. C. Peng, A. Perch, M. M. Pfützner, D. D. Phan, S. Phan-Budd, L. Pinsky, R. K. Plunkett, N. Poonthottathil, C. S. J. Pun, F. Z. Qi, M. Qi, X. Qian, X. Qiu, A. Radovic, N. Raper, B. Rebel, J. Ren, C. Rosenfeld, R. Rosero, B. Roskovec, X. C. Ruan, H. A. Rubin, P. Sail, M. C. Sanchez, J. Schneps, A. Schreckenberger, P. Schreiner, R. Sharma, S. Moed Sher, A. Sousa, H. Steiner, G. X. Sun, J. L. Sun, N. Tagg, R. L. Talaga, W. Tang, D. Taychenachev, J. Thomas, M. A. Thomson, X. Tian, A. Timmons, J. Todd, S. C. Tognini, R. Toner, D. Torretta, K. Treskov, K. V. Tsang, C. E. Tull, G. Tzanakos, J. Urheim, P. Vahle, N. Viaux, B. Viren, V. Vorobel, C. H. Wang, M. Wang, N. Y. Wang, R. G. Wang, W. Wang, X. Wang, Y. F. Wang, Z. Wang, Z. M. Wang, R. C. Webb, A. Weber, H. Y. Wei, L. J. Wen, K. Whisnant, C. White, L. Whitehead, L. H. Whitehead, T. Wise, S. G. Wojcicki, H. L. H. Wong, S. C. F. Wong, E. Worcester, C.-H. Wu, Q. Wu, W. J.

Wu, D. M. Xia, J. K. Xia, Z. Z. Xing, J. L. Xu, J. Y. Xu, Y. Xu, T. Xue, C. G. Yang, H. Yang, L. Yang, M. S. Yang, M. T. Yang, M. Ye, Z. Ye, M. Yeh, B. L. Young, Z. Y. Yu, S. Zeng, L. Zhan, C. Zhang, H. H. Zhang, J. W. Zhang, Q. M. Zhang, X. T. Zhang, Y. M. Zhang, Y. X. Zhang, Z. J. Zhang, Z. P. Zhang, Z. Y. Zhang, J. Zhao, Q. W. Zhao, Y. B. Zhao, W. L. Zhong, L. Zhou, N. Zhou, H. L. Zhuang, and J. H. Zou. Limits on active to sterile neutrino oscillations from disappearance searches in the minos, daya bay, and bugey-3 experiments. *Phys. Rev. Lett.*, 117:151801, Oct 2016.

[5] S. Agostinelli, J. Allison, K. Amako, J. Apostolakis, H. Araujo, P. Arce, M. Asai, D. Axen, S. Banerjee, G. Barrand, F. Behner, L. Bellagamba, J. Boudreau, L. Broglia, A. Brunengo, H. Burkhardt, S. Chauvie, J. Chuma, R. Chytracek, G. Cooperman, G. Cosmo, P. Degtyarenko, A. Dell'Acqua, G. Depaola, D. Dietrich, R. Enami, A. Feliciello, C. Ferguson, H. Fesefeldt, G. Folger, F. Foppiano, A. Forti, S. Garelli, S. Giani, R. Giannitrapani, D. Gibin, J. G. Cadenas, I. Gonzalez, G. G. Abril, G. Greeniaus, W. Greiner, V. Grichine, A. Grossheim, S. Guatelli, P. Gumplinger, R. Hamatsu, K. Hashimoto, H. Hasui, A. Heikkinen, A. Howard, V. Ivanchenko, A. Johnson, F. Jones, J. Kallenbach, N. Kanaya, M. Kawabata, Y. Kawabata, M. Kawaguti, S. Kelner, P. Kent, A. Kimura, T. Kodama, R. Kokoulin, M. Kossov, H. Kurashige, E. Lamanna, T. Lampn, V. Lara, V. Lefebure, F. Lei, M. Liendl, W. Lockman, F. Longo, S. Magni, M. Maire, E. Medernach, K. Minamimoto, P. M. de Freitas, Y. Morita, K. Murakami, M. Nagamatu, R. Nartallo, P. Nieminen, T. Nishimura, K. Ohtsubo, M. Okamura, S. O'Neale, Y. Oohata, K. Paech, J. Perl, A. Pfeiffer, M. Pia, F. Ranjard, A. Rybin, S. Sadilov, E. D. Salvo, G. Santin, T. Sasaki, N. Savvas, Y. Sawada, S. Scherer, S. Sei, V. Sirotenko, D. Smith, N. Starkov, H. Stoecker, J. Sulkimo, M. Takahata, S. Tanaka, E. Tcherniaev, E. S. Tehrani, M. Tropeano, P. Truscott, H. Uno, L. Urban, P. Urban, M. Verderi, A. Walkden, W. Wander, H. Weber, J. Wellisch, T. Wenaus, D. Williams, D. Wright, T. Yamada, H. Yoshida, and D. Zschiesche. Geant4: a simulation toolkit. *Nuclear Instruments and Methods in Physics Research Section A: Accelerators, Spectrometers, Detectors and Associated Equipment*, 506(3):250 – 303, 2003.

[6] M. Aguilar-Bentez, J. Fuster, S. Mart-Garca, and A. Santamara, editors. *Proceedings, 37th International Conference on High Energy Physics (ICHEP 2014)*, volume 273-275, 2016.

[7] J. K. Ahn, S. Chebotaryov, J. H. Choi, S. Choi, W. Choi, Y. Choi, H. I. Jang, J. S. Jang, E. J. Jeon, I. S. Jeong, K. K. Joo, B. R. Kim, B. C. Kim, H. S. Kim, J. Y. Kim, S. B. Kim, S. H. Kim, S. Y. Kim, W. Kim, Y. D. Kim, J. Lee, J. K. Lee, I. T. Lim, K. J. Ma, M. Y. Pac, I. G. Park, J. S. Park, K. S. Park, J. W. Shin, K. Siyeon, B. S. Yang, I. S. Yeo, S. H. Yi, and I. Yu. Observation of reactor electron antineutrinos disappearance in the reno experiment. *Phys. Rev. Lett.*, 108:191802, May 2012.

[8] J. Allison, K. Amako, J. Apostolakis, H. Araujo, P. A. Dubois, M. Asai, G. Barrand, R. Capra, S. Chauvie, R. Chytracek, G. A. P. Cirrone, G. Cooperman, G. Cosmo, G. Cuttone, G. G. Daquino, M. Donszelmann, M. Dressel, G. Folger, F. Foppiano, J. Generowicz, V. Grichine, S. Guatelli, P. Gumplinger, A. Heikkinen, I. Hrivnacova, A. Howard, S. Incerti, V. Ivanchenko, T. Johnson, F. Jones, T. Koi, R. Kokoulin,

M. Kossov, H. Kurashige, V. Lara, S. Larsson, F. Lei, O. Link, F. Longo, M. Maire, A. Mantero, B. Mascialino, I. McLaren, P. M. Lorenzo, K. Minamimoto, K. Murakami, P. Nieminen, L. Pandola, S. Parlati, L. Peralta, J. Perl, A. Pfeiffer, M. G. Pia, A. Ribon, P. Rodrigues, G. Russo, S. Sadilov, G. Santin, T. Sasaki, D. Smith, N. Starkov, S. Tanaka, E. Tcherniaev, B. Tome, A. Trindade, P. Truscott, L. Urban, M. Verderi, A. Walkden, J. P. Wellisch, D. C. Williams, D. Wright, and H. Yoshida. Geant4 developments and applications. *IEEE Transactions on Nuclear Science*, 53(1):270–278, Feb 2006.

[9] J. Allison, K. Amako, J. Apostolakis, P. Arce, M. Asai, T. Aso, E. Bagli, A. Bagulya, S. Banerjee, G. Barrand, B. Beck, A. Bogdanov, D. Brandt, J. Brown, H. Burkhardt, P. Canal, D. Cano-Ott, S. Chauvie, K. Cho, G. Cirrone, G. Cooperman, M. Cortes-Giraldo, G. Cosmo, G. Cuttone, G. Depaola, L. Desorgher, X. Dong, A. Dotti, V. Elvira, G. Folger, Z. Francis, A. Galoyan, L. Garnier, M. Gayer, K. Genser, V. Grichine, S. Guatelli, P. Gueye, P. Gumplinger, A. Howard, I. Hrivnacova, S. Hwang, S. Incerti, A. Ivanchenko, V. Ivanchenko, F. Jones, S. Jun, P. Kaitaniemi, N. Karakatsanis, M. Karamitros, M. Kelsey, A. Kimura, T. Koi, H. Kurashige, A. Lechner, S. Lee, F. Longo, M. Maire, D. Mancusi, A. Mantero, E. Mendoza, B. Morgan, K. Murakami, T. Nikitina, L. Pandola, P. Paprocki, J. Perl, I. Petrovi, M. Pia, W. Pokorski, J. Quesada, M. Raine, M. Reis, A. Ribon, A. R. Fira, F. Romano, G. Russo, G. Santin, T. Sasaki, D. Sawkey, J. Shin, I. Strakovsky, A. Taborda, S. Tanaka, B. Tom, T. Toshito, H. Tran, P. Truscott, L. Urban, V. Uzhinsky, J. Verbeke, M. Verderi, B. Wendt, H. Wenzel, D. Wright, D. Wright, T. Yamashita, J. Yarba, and H. Yoshida. Recent developments in geant4. *Nuclear Instruments and Methods in Physics Research Section A: Accelerators, Spectrometers, Detectors and Associated Equipment*, 835:186 – 225, 2016.

[10] F. P. An, A. B. Balantekin, H. R. Band, M. Bishai, S. Blyth, I. Butorov, D. Cao, G. F. Cao, J. Cao, W. R. Cen, Y. L. Chan, J. F. Chang, L. C. Chang, Y. Chang, H. S. Chen, Q. Y. Chen, S. M. Chen, Y. X. Chen, Y. Chen, J. H. Cheng, J. Cheng, Y. P. Cheng, J. J. Cherwinka, M. C. Chu, J. P. Cummings, J. de Arcos, Z. Y. Deng, X. F. Ding, Y. Y. Ding, M. V. Diwan, J. Dove, E. Draeger, D. A. Dwyer, W. R. Edwards, S. R. Ely, R. Gill, M. Gonchar, G. H. Gong, H. Gong, M. Grassi, W. Q. Gu, M. Y. Guan, L. Guo, X. H. Guo, R. W. Hackenburg, R. Han, S. Hans, M. He, K. M. Heeger, Y. K. Heng, A. Higuera, Y. K. Hor, Y. B. Hsiung, B. Z. Hu, L. M. Hu, L. J. Hu, T. Hu, W. Hu, E. C. Huang, H. X. Huang, X. T. Huang, P. Huber, G. Hussain, D. E. Jaffe, P. Jaffke, K. L. Jen, S. Jetter, X. P. Ji, X. L. Ji, J. B. Jiao, R. A. Johnson, L. Kang, S. H. Kettell, S. Kohn, M. Kramer, K. K. Kwan, M. W. Kwok, T. Kwok, T. J. Langford, K. Lau, L. Lebanowski, J. Lee, R. T. Lei, R. Leitner, K. Y. Leung, J. K. C. Leung, C. A. Lewis, D. J. Li, F. Li, G. S. Li, Q. J. Li, S. C. Li, W. D. Li, X. N. Li, X. Q. Li, Y. F. Li, Z. B. Li, H. Liang, C. J. Lin, G. L. Lin, P. Y. Lin, S. K. Lin, J. J. Ling, J. M. Link, L. Littenberg, B. R. Littlejohn, D. W. Liu, H. Liu, J. L. Liu, J. C. Liu, S. S. Liu, C. Lu, H. Q. Lu, J. S. Lu, K. B. Luk, Q. M. Ma, X. Y. Ma, X. B. Ma, Y. Q. Ma, D. A. Martinez Caicedo, K. T. McDonald, R. D. McKeown, Y. Meng, I. Mitchell, J. Monari Kebwaro, Y. Nakajima, J. Napolitano, D. Naumov, E. Naumova, H. Y. Ngai, Z. Ning, J. P. Ochoa-Ricoux, A. Olshevski, H.-R. Pan, J. Park, S. Patton, V. Pec, J. C.

Peng, L. E. Piilonen, L. Pinsky, C. S. J. Pun, F. Z. Qi, M. Qi, X. Qian, N. Raper, B. Ren, J. Ren, R. Rosero, B. Roskovec, X. C. Ruan, B. B. Shao, H. Steiner, G. X. Sun, J. L. Sun, W. Tang, D. Taychenachev, K. V. Tsang, C. E. Tull, Y. C. Tung, N. Viaux, B. Viren, V. Vorobel, C. H. Wang, M. Wang, N. Y. Wang, R. G. Wang, W. Wang, W. W. Wang, X. Wang, Y. F. Wang, Z. Wang, Z. Wang, Z. M. Wang, H. Y. Wei, L. J. Wen, K. Whisnant, C. G. White, L. Whitehead, T. Wise, H. L. H. Wong, S. C. F. Wong, E. Worcester, Q. Wu, D. M. Xia, J. K. Xia, X. Xia, Z. Z. Xing, J. Y. Xu, J. L. Xu, J. Xu, Y. Xu, T. Xue, J. Yan, C. G. Yang, L. Yang, M. S. Yang, M. T. Yang, M. Ye, M. Yeh, B. L. Young, G. Y. Yu, Z. Y. Yu, S. L. Zang, L. Zhan, C. Zhang, H. H. Zhang, J. W. Zhang, Q. M. Zhang, Y. M. Zhang, Y. X. Zhang, Y. M. Zhang, Z. J. Zhang, Z. Y. Zhang, Z. P. Zhang, J. Zhao, Q. W. Zhao, Y. F. Zhao, Y. B. Zhao, L. Zheng, W. L. Zhong, L. Zhou, N. Zhou, H. L. Zhuang, and J. H. Zou. Measurement of the reactor antineutrino flux and spectrum at daya bay. *Phys. Rev. Lett.*, 116:061801, Feb 2016.

[11] F. P. An, A. B. Balantekin, H. R. Band, M. Bishai, S. Blyth, D. Cao, G. F. Cao, J. Cao, W. R. Cen, Y. L. Chan, J. F. Chang, L. C. Chang, Y. Chang, H. S. Chen, Q. Y. Chen, S. M. Chen, Y. X. Chen, Y. Chen, J.-H. Cheng, J. Cheng, Y. P. Cheng, Z. K. Cheng, J. J. Cherwinka, M. C. Chu, A. Chukanov, J. P. Cummings, J. de Arcos, Z. Y. Deng, X. F. Ding, Y. Y. Ding, M. V. Diwan, M. Dolgareva, J. Dove, D. A. Dwyer, W. R. Edwards, R. Gill, M. Gonchar, G. H. Gong, H. Gong, M. Grassi, W. Q. Gu, M. Y. Guan, L. Guo, R. P. Guo, X. H. Guo, Z. Guo, R. W. Hackenburg, R. Han, S. Hans, M. He, K. M. Heeger, Y. K. Heng, A. Higuera, Y. K. Hor, Y. B. Hsiung, B. Z. Hu, T. Hu, W. Hu, E. C. Huang, H. X. Huang, X. T. Huang, P. Huber, W. Huo, G. Hussain, D. E. Jaffe, P. Jaffke, K. L. Jen, S. Jetter, X. P. Ji, X. L. Ji, J. B. Jiao, R. A. Johnson, J. Joshi, L. Kang, S. H. Kettell, S. Kohn, M. Kramer, K. K. Kwan, M. W. Kwok, T. Kwok, T. J. Langford, K. Lau, L. Lebanowski, J. Lee, J. H. C. Lee, R. T. Lei, R. Leitner, J. K. C. Leung, C. Li, D. J. Li, F. Li, G. S. Li, Q. J. Li, S. Li, S. C. Li, W. D. Li, X. N. Li, Y. F. Li, Z. B. Li, H. Liang, C. J. Lin, G. L. Lin, S. Lin, S. K. Lin, Y.-C. Lin, J. J. Ling, J. M. Link, L. Littenberg, B. R. Littlejohn, D. W. Liu, J. L. Liu, J. C. Liu, C. W. Loh, C. Lu, H. Q. Lu, J. S. Lu, K. B. Luk, Z. Lv, Q. M. Ma, X. Y. Ma, X. B. Ma, Y. Q. Ma, Y. Malyshkin, D. A. Martinez Caicedo, K. T. McDonald, R. D. McKeown, I. Mitchell, M. Mooney, Y. Nakajima, J. Napolitano, D. Naumov, E. Naumova, H. Y. Ngai, Z. Ning, J. P. Ochoa-Ricoux, A. Olshevskiy, H.-R. Pan, J. Park, S. Patton, V. Pec, J. C. Peng, L. Pinsky, C. S. J. Pun, F. Z. Qi, M. Qi, X. Qian, N. Raper, J. Ren, R. Rosero, B. Roskovec, X. C. Ruan, H. Steiner, G. X. Sun, J. L. Sun, W. Tang, D. Taychenachev, K. Treskov, K. V. Tsang, C. E. Tull, N. Viaux, B. Viren, V. Vorobel, C. H. Wang, M. Wang, N. Y. Wang, R. G. Wang, W. Wang, X. Wang, Y. F. Wang, Z. Wang, Z. Wang, Z. M. Wang, H. Y. Wei, L. J. Wen, K. Whisnant, C. G. White, L. Whitehead, T. Wise, H. L. H. Wong, S. C. F. Wong, E. Worcester, C.-H. Wu, Q. Wu, W. J. Wu, D. M. Xia, J. K. Xia, Z. Z. Xing, J. Y. Xu, J. L. Xu, Y. Xu, T. Xue, C. G. Yang, H. Yang, L. Yang, M. S. Yang, M. T. Yang, M. Ye, Z. Ye, M. Yeh, B. L. Young, Z. Y. Yu, S. Zeng, L. Zhan, C. Zhang, H. H. Zhang, J. W. Zhang, Q. M. Zhang, X. T. Zhang, Y. M. Zhang, Y. X. Zhang, Y. M. Zhang, Z. J. Zhang, Z. Y. Zhang, Z. P. Zhang, J. Zhao, Q. W. Zhao, Y. B. Zhao, W. L. Zhong, L. Zhou, N. Zhou, H. L. Zhuang, and J. H. Zou. Improved search for a light

sterile neutrino with the full configuration of the daya bay experiment. *Phys. Rev. Lett.*, 117:151802, Oct 2016.

[12] J. M. Conrad, W. C. Louis, and M. H. Shaevitz. The LSND and MiniBooNE Oscillation Searches at High Δm^2. *Ann. Rev. Nucl. Part. Sci.*, 63:45–67, 2013.

[13] D. A. Dwyer. Antineutrinos from nuclear reactors: recent oscillation measurements. *New J. Phys.*, 17(2):025003, 2015.

[14] Eljen Technology. *General Purpose Plastic Scintillators.* URL: www.eljentechnology.com.

[15] Eljen Technology. *Plastic Scintillator.* URL: www.eljentechnology.com.

[16] E. Fermi. Versuch einer theorie der β-strahlen. i. *Zeitschrift für Physik*, 88(3):161–177, Mar 1934.

[17] Gamma Ray Energy Tracking In-Beam Nuclear Array. *Digitizer Specification*, 03 2008.

[18] HAMAMATSU. *Photomultiplier Tubes*, 08 2014.

[19] A. C. Hayes, J. L. Friar, G. T. Garvey, D. Ibeling, G. Jungman, T. Kawano, and R. W. Mills. Possible origins and implications of the shoulder in reactor neutrino spectra. *Phys. Rev. D*, 92:033015, Aug 2015.

[20] A. C. Hayes, J. L. Friar, G. T. Garvey, G. Jungman, and G. Jonkmans. Systematic Uncertainties in the Analysis of the Reactor Neutrino Anomaly. *Phys. Rev. Lett.*, 112:202501, 2014.

[21] A. C. Hayes and P. Vogel. Reactor neutrino spectra. *Annual Review of Nuclear and Particle Science*, 66(1):219–244, 2016.

[22] https://www.ezag.com/home/products/isotope_products/.

[23] http://www.micronsemiconductor.co.uk/.

[24] P. Huber. On the determination of anti-neutrino spectra from nuclear reactors. *Phys. Rev.*, C84:024617, 2011. [Erratum: Phys. Rev.C85,029901(2012)].

[25] O. Kadri, V. Ivanchenko, F. Gharbi, and A. Trabelsi. Incorporation of the goudsmit-saunderson electron transport theory in the geant4 monte carlo code. pages 3624–3632, 03 2013.

[26] G. F. Knoll. *Radiation Detection and Measurement.* John Wiley & Sons, New York, 2010.

[27] A. J. Mitchell et al. The X-Array and SATURN: A new decay-spectroscopy station for CARIBU. *Nucl. Instrum. Meth.*, A763:232–239, 2014.

[28] B. Rasco et al. Decays of the Three Top Contributors to the Reactor ν_e^- High-Energy Spectrum, ^{92}Rb, ^{96gs}Y, and ^{142}Cs, Studied with Total Absorption Spectroscopy. *Phys. Rev. Lett.*, 117(9):092501, 2016.

[29] J. F. T. Raymond E. March. *Quadrupole Ion Trap Mass Spectrometry.* John Wiley & Sons, New York, 2 edition, 8 2005.

[30] K. Saucke, G. Pausch, J. Stein, H. G. Ortlepp, and P. Schotanus. Stabilizing scintillation detector systems with pulsed leds: a method to derive the led temperature from pulse height spectra. *IEEE Transactions on Nuclear Science*, 52(6):3160–3165, Dec 2005.

[31] G. Savard et al. CARIBU: a new facility for the study of neutron-rich isotopes. *Hyperfine Interact.*, 199(1-3):301–309, 2011.

[32] N. Scielzo, R. Yee, P. Bertone, F. Buchinger, S. Caldwell, J. Clark, A. Czeszumska, C. Deibel, J. Greene, S. Gulick, D. Lascar, A. Levand, G. Li, E. Norman, S. Padgett, M. Pedretti, A. P. Galvan, G. Savard, R. Segel, K. Sharma, M. Sternberg, J. V. Schelt, and B. Zabransky. A novel approach to β-delayed neutron spectroscopy using the beta-decay paul trap. *Nuclear Data Sheets*, 120:70 – 73, 2014.

[33] N. D. Scielzo, S. J. Freedman, B. K. Fujikawa, and P. A. Vetter. Measurement of the $\beta - \nu$ correlation using magneto-optically trapped ^{21}Na. *Phys. Rev. Lett.*, 93:102501, Aug 2004.

[34] S.-H. Seo. New Results from RENO. *PoS*, Neutel2013:018, 2014.

[35] A. A. Sonzogni, T. D. Johnson, and E. A. McCutchan. Nuclear structure insights into reactor antineutrino spectra. *Phys. Rev.*, C91(1):011301, 2015.

[36] M. Sternberg. *Limits on Tensor Currents from ^{8}Li β Decay.* PhD thesis, The University of Chicago, Chicago, Illinois, 8 2013.

[37] M. G. Sternberg, R. Segel, N. D. Scielzo, G. Savard, J. A. Clark, P. F. Bertone, F. Buchinger, M. Burkey, S. Caldwell, A. Chaudhuri, J. E. Crawford, C. M. Deibel, J. Greene, S. Gulick, D. Lascar, A. F. Levand, G. Li, A. Pérez Galván, K. S. Sharma, J. Van Schelt, R. M. Yee, and B. J. Zabransky. Limit on tensor currents from ^{8}Li β decay. *Phys. Rev. Lett.*, 115:182501, Oct 2015.

[38] T. Sumikama et al. Test of the Conserved Vector Current Hypothesis by beta-ray Angular Distribution Measurement in the Mass-8 System. *Phys. Rev.*, C83:065501, 2011.

[39] L. Urban. A model for multiple scattering in Geant4. 2006.

[40] www.fastrad.net.

[41] www.nndc.bnl.gov/ensdf/.

Appendix A

Data Acquisition Sort Code

A.1 FPSort.cc

```
//////////////////////////////////////
/// FPSort.cc                     ///
//////////////////////////////////////

#include <stdio.h>
#include <stdlib.h>
#include <string.h>
#include <fcntl.h>
#include <time.h>
#include <iomanip>
#include <iostream>
#include <fstream>
#include <string.h>
```

```
#include "TROOT.h"
#include "TFile.h"
#include "TH1.h"
#include "TH2.h"
#include "TH3.h"
#include "TObject.h"
#include "TTree.h"
#include <cmath>
#include "TBranch.h"
#include "FP.h"

using namespace std;

#define NumGe 2
#define NumSi 4
#define NumB 4
#define MaxNumChan 10
#define ChanGamma 1
#define ChanBeta 2
#define ChanSi 9
#define Mwidth 350.
#define Kwidth 80.0
#define OverLapWin 1000
#define COINCIWINGBL -50.0
#define COINCIWINGBH 10.
#define COINCIWINGG 60. // everything is in 10s of ns
#define BUNCHERDT 0
#define BetaThreshold 500
vector<int> tapeevtcounter;
```

```
vector<unsigned long long int> tapetimecounter;
float gain[NumGe]={0.0};
float off[NumGe]={0.0};
float BaseLine[NumGe]={0.};;
float PZ[NumGe]={0.};
int   toff[NumGe]={0};
bool noisy = 0;
unsigned short int ChanMap[100]={0};
unsigned short int ChanType[30]={0};
EVENT    event[MaxNumChan];
TH2D *hid;
TH1D *mapid,*SiERaw1,*SiERaw2,*SiERaw3,*SiERaw4,*SiE1,*SiE2,*SiE4;
TH1D *BetaERaw1,*BetaERaw2,*BetaERaw3,*BetaERaw4,*BetaE1,*BetaE2,*BetaE4;
TH1D *GamERaw1,*GamERaw2;
TH2F *GamE,*GamERaw;
TH1D *BetaE3,*SiE3;
TH2F *BetaERaw;
TH2F *SiERaw;
TH1D *BetaE,*SiE;
TH1D *hdtSiB,*hdtSiB1,*hdtSiB2,*hdtSiB3,*hdtSiB4,*SiBeta_E_time_All,*Tape_time;
TH2D *SiBeta_E_All, *SiBeta_E[4],*SiGamma_E[8],*BetaSi_E[4];
TH1D *SiBeta_E_All_X, *SiBeta_E_X[4], *SiBeta_E_All_Y, *SiBeta_E_Y[4];
TH1D *SiGamma_dT_All, *Gamma_E_withSi[2][4], *Gamma_E_withAnySi[2];
TH2I *SiBeta_Coin;
TH2F *gb1,*gb2,*DE_E_total;
TH2F *tb[2];
TH2F *baseCal1;
TH2F *baseCal2;
TH2F *baseRaw;
```

```
TH2F *pz1Cal;
Float_t PlasEG = 0.;
Float_t tapeE = 0.;
Float_t SiEG = 0.;
double dtSiPlasG;
int SiIDG;
int PlasIDG;
unsigned long long int si_LEDts;
unsigned long long int p_LEDts,tape_t,tapeevt,starttime, endtime;
int firsttime = 0.;
bool tapeflag;
int evtcount = 0;
unsigned long long int p_EventNum;
unsigned long long int si_EventNum;
TTree* detrawgated = new TTree("detrawgated","Gated Detectors Tree");
TTree* detrawplas = new TTree("detrawplas","Platics Detector Tree");
TTree* detrawge = new TTree("detrawge","HPGe Detector Tree");
TTree* detrawsi = new TTree("detrawsi","Si Detector Tree");

//////////////////////////////////////////////////////////////////
void setuproot(TFile *f){
  char str[127];
  char fn[127];

  sprintf(str,"BetaE");
  sprintf(fn,"BetaE");
  BetaE=(TH1D*)f->Get(str);
  if(BetaE==0)
    BetaE=new TH1D(str,fn,5000,0,20000);
```

```
sprintf(str,"SiE");
sprintf(fn,"SiE");
SiE=(TH1D*)f->Get(str);
if( SiE==0 )
  SiE=new TH1D(str,fn,5000,0,20000);

sprintf(str,"mapid");
sprintf(fn,"mapid");
mapid=(TH1D*)f->Get(str);
if( mapid==0 )
  mapid = new TH1D(str,fn,100,0,100);

sprintf(str,"id");
sprintf(fn,"Channel_id");
hid=(TH2D*)f->Get(str);
if( hid==0 )
  hid = new TH2D(str,fn,10,0,10,10,0,10);

sprintf(str,"gb1");
sprintf(fn,"gb1");
gb1=(TH2F*)f->Get(str);
if( gb1 == 0 )
gb1 = new TH2F(str,fn,8192,0,8192,8192,0,16384);

sprintf(str,"gb2");
sprintf(fn,"gb2");
gb2=(TH2F*)f->Get(str);
if(gb2 == 0)
```

```
  gb2 = new TH2F(str,fn,8192,0,8192,8192,0,16384);

sprintf(str,"GamERaw");
sprintf(fn,"GamERaw");
GamERaw=(TH2F*)f->Get(str);
if( GamERaw == 0 )
  GamERaw = new TH2F(str,fn,16384,0,16384,10,0,10);

sprintf(str,"GamERaw1");
sprintf(fn,"GamERaw1");
GamERaw1=(TH1D*)f->Get(str);
if( GamERaw1 == 0 )
  GamERaw1 = new TH1D(str,fn,16384,0,16384);

sprintf(str,"GamERaw2");
sprintf(fn,"GamERaw2");
GamERaw2=(TH1D*)f->Get(str);
if( GamERaw2 == 0 )
  GamERaw2 = new TH1D(str,fn,16384,0,16384);

sprintf(str,"BetaERaw");
sprintf(fn,"BetaERaw");
BetaERaw=(TH2F*)f->Get(str);
if( BetaERaw == 0 )
  BetaERaw = new TH2F(str,fn,16384,0,16384,10,0,10);

sprintf(str,"BetaERaw1");
sprintf(fn,"BetaERaw1");
BetaERaw1=(TH1D*)f->Get(str);
```

```
if( BetaERaw1 == 0 )
  BetaERaw1 = new TH1D(str,fn,16384,0,16384);

sprintf(str,"BetaERaw2");
sprintf(fn,"BetaERaw2");
BetaERaw2=(TH1D*)f->Get(str);
if( BetaERaw2 == 0 )
  BetaERaw2 = new TH1D(str,fn,16384,0,16384);

sprintf(str,"BetaERaw3");
sprintf(fn,"BetaERaw3");
BetaERaw3=(TH1D*)f->Get(str);
if( BetaERaw3 == 0 )
  BetaERaw3 = new TH1D(str,fn,16384,0,16384);

sprintf(str,"BetaERaw4");
sprintf(fn,"BetaERaw4");
BetaERaw4=(TH1D*)f->Get(str);
if( BetaERaw4 == 0 )
  BetaERaw4 = new TH1D(str,fn,16384,0,16384);

sprintf(str,"SiERaw");
sprintf(fn,"SiERaw");
SiERaw=(TH2F*)f->Get(str);
if( SiERaw == 0 )
  SiERaw = new TH2F(str,fn,16384,0,16384,10,0,10);

sprintf(str,"SiERaw1");
sprintf(fn,"SiERaw1");
```

```
SiERaw1=(TH1D*)f->Get(str);
if( SiERaw1 == 0 )
  SiERaw1 = new TH1D(str,fn,16384,0,16384);

sprintf(str,"SiERaw2");
sprintf(fn,"SiERaw2");
SiERaw2=(TH1D*)f->Get(str);
if( SiERaw2 == 0 )
  SiERaw2 = new TH1D(str,fn,16384,0,16384);

sprintf(str,"SiERaw3");
sprintf(fn,"SiERaw3");
SiERaw3=(TH1D*)f->Get(str);
if( SiERaw3 == 0 )
  SiERaw3 = new TH1D(str,fn,16384,0,16384);

sprintf(str,"SiERaw4");
sprintf(fn,"SiERaw4");
SiERaw4=(TH1D*)f->Get(str);
if( SiERaw4 == 0 )
SiERaw4 = new TH1D(str,fn,16384,0,16384);

sprintf(str,"BetaE1");
sprintf(fn,"BetaE1");
BetaE1=(TH1D*)f->Get(str);
if( BetaE1 == 0 )
  BetaE1 = new TH1D(str,fn,16384,0,16384);

sprintf(str,"BetaE2");
```

```
sprintf(fn,"BetaE2");
BetaE2=(TH1D*)f->Get(str);
if( BetaE2 == 0 )
  BetaE2 = new TH1D(str,fn,16384,0,16384);

sprintf(str,"BetaE3");
sprintf(fn,"BetaE3");
BetaE3=(TH1D*)f->Get(str);
if(BetaE3 == 0)
  BetaE3 = new TH1D(str,fn,16384,0,16384);

sprintf(str,"BetaE4");
sprintf(fn,"BetaE4");
BetaE4=(TH1D*)f->Get(str);
if( BetaE4 == 0 )
  BetaE4 = new TH1D(str,fn,16384,0,16384);

sprintf(str,"SiE1");
sprintf(fn,"SiE1");
SiE1=(TH1D*)f->Get(str);
if( SiE1 == 0 )
  SiE1 = new TH1D(str,fn,16384,0,16384);

sprintf(str,"SiE2");
sprintf(fn,"SiE2");
SiE2=(TH1D*)f->Get(str);
if( SiE2 == 0 )
  SiE2 = new TH1D(str,fn,16384,0,16384);
```

```
sprintf(str,"SiE3");
sprintf(fn,"SiE3");
SiE3=(TH1D*)f->Get(str);
if( SiE3 == 0 )
  SiE3 = new TH1D(str,fn,16384,0,16384);

sprintf(str,"SiE4");
sprintf(fn,"SiE4");
SiE4=(TH1D*)f->Get(str);
if( SiE4 == 0 )
  SiE4 = new TH1D(str,fn,16384,0,16384);

sprintf(str,"Tape_time");
sprintf(fn,"Tape_time");
Tape_time=(TH1D*)f->Get(str);
if( Tape_time == 0 )
  Tape_time = new TH1D(str,fn,100,0,50000);
  Tape_time->GetXaxis()->SetTitle("global clock time");
  Tape_time->GetYaxis()->SetTitle("Tape Signal");

sprintf(str,"hdtSiB");
sprintf(fn,"hdtSiB");
hdtSiB=(TH1D*)f->Get(str);
if( hdtSiB == 0 )
  hdtSiB = new TH1D(str,fn,4000,-2000,2000);

sprintf(str,"hdtSiB1");
sprintf(fn,"hdtSiB1");
hdtSiB1=(TH1D*)f->Get(str);
```

```
if( hdtSiB1 == 0 )
  hdtSiB1 = new TH1D(str,fn,4000,-2000,2000);

sprintf(str,"hdtSiB2");
sprintf(fn,"hdtSiB2");
hdtSiB2=(TH1D*)f->Get(str);
if( hdtSiB2 == 0 )
  hdtSiB2 = new TH1D(str,fn,4000,-2000,2000);

sprintf(str,"hdtSiB3");
sprintf(fn,"hdtSiB3");
hdtSiB3=(TH1D*)f->Get(str);
if( hdtSiB3 == 0 )
  hdtSiB3 = new TH1D(str,fn,4000,-2000,2000);

sprintf(str,"hdtSiB4");
sprintf(fn,"hdtSiB4");
hdtSiB4=(TH1D*)f->Get(str);
if( hdtSiB4 == 0 )
  hdtSiB4 = new TH1D(str,fn,4000,-2000,2000);

int SiBeta_E_rebin = 10;
sprintf(str,"SiBeta_E_All");
sprintf(fn,"SiBeta_E_All");
SiBeta_E_All=(TH2D*)f->Get(str);

if( SiBeta_E_All == 0 )
  {
    SiBeta_E_All = new TH2D(str,fn,
```

```
      16384/SiBeta_E_rebin,0,16384,
      16384/SiBeta_E_rebin,0,16384);
    SiBeta_E_All->GetXaxis()->SetTitle("Plastic Channel #");
    SiBeta_E_All->GetYaxis()->SetTitle("Si Channel #");
  }

for( int s=0; s<4; s++ )
  {
    sprintf(str,"SiBeta_E_%i",s+1);
    sprintf(fn,"SiBeta_E_%i",s+1);
    SiBeta_E[s]=(TH2D*)f->Get(str);
    if( SiBeta_E[s] == 0 )
      {
        SiBeta_E[s] = new TH2D(str,fn,
        16384/SiBeta_E_rebin,0,16384,
        16384/SiBeta_E_rebin,0,16384);
        SiBeta_E[s]->GetXaxis()->SetTitle("Plastic Channel #");
        SiBeta_E[s]->GetYaxis()->SetTitle("Si Channel #");
      }
    }

sprintf(str,"SiGamma_dT_All");
sprintf(fn,"SiGamma_dT_All");
SiGamma_dT_All = (TH1D*)f->Get(str);
if( SiGamma_dT_All==0 )
 {
  SiGamma_dT_All = new TH1D(str,fn,4000,-2000,2000);
  SiGamma_dT_All->GetXaxis()->SetTitle("Gamma - Si Timing");
 }
```

```
  for( int i=0; i<2; i++ )
  {
    for( int b=0; b<4; b++ )
    {
      sprintf(str,"Gamma_E_withSi%i_Ge%i",b+1,i+1);
      Gamma_E_withSi[i][b]=(TH1D*)f->Get(str);
      if( Gamma_E_withSi[i][b] == 0 )
      {
         Gamma_E_withSi[i][b] = new TH1D(str,str,16384,0,16384);
      }
    }
          sprintf(str,"Gamma_E_withAnySi_Ge%i",i+1);
          Gamma_E_withAnySi[i]=(TH1D*)f->Get(str);
          if( Gamma_E_withAnySi[i] == 0 )
    {
      Gamma_E_withAnySi[i] = new TH1D(str,str,16384,0,16384);
    }
  }

  sprintf(str,"SiBeta_Coin");
  sprintf(fn,"SiBeta_Coin");
  SiBeta_Coin=(TH2I*)f->Get(str);
  if( SiBeta_Coin==0 )
  {
    SiBeta_Coin = new TH2I(str,fn,4,0,4,4,0,4);
  }

for( int i=0;i<2;i++ ){
```

```
  sprintf(str,"tb%i",i+1);
  sprintf(fn,"tb%i",i+1);
  tb[i]=(TH2F*)f->Get(str);
  if( tb[i] == 0 )
    tb[i] = new TH2F(str,fn,2248,-200,2048,2048,0,2048);
}

sprintf(str,"baseCal1");
sprintf(fn,"baseCal1");
baseCal1=(TH2F*)f->Get(str);
if( baseCal1 == 0 )
  baseCal1 = new TH2F(str,fn,3000,7000,10000,2,0,2);

sprintf(str,"baseCal2");
sprintf(fn,"baseCal2");
baseCal2=(TH2F*)f->Get(str);
if( baseCal2 == 0 )
baseCal2 = new TH2F(str,fn,3000,7000,10000,2,0,2);

sprintf(str,"baseRaw");
sprintf(fn,"baseRaw");
baseRaw=(TH2F*)f->Get(str);
if( baseRaw == 0 )
  baseRaw = new TH2F(str,fn,3000,7000,10000,2,0,2);

sprintf(str,"pz1Cal");
sprintf(fn,"pz1Cal");
pz1Cal=(TH2F*)f->Get(str);
if( pz1Cal == 0 )
```

```
    pz1Cal = new TH2F(str,fn,100000,0.5,1.5,2,0,2);


  sprintf(str,"DE_E_total");
  sprintf(fn,"DE_E_total");
  DE_E_total=(TH2F*)f->Get(str);
  if( DE_E_total==0 ){
    DE_E_total = new TH2F(str,fn,
          16384/SiBeta_E_rebin,0,16384,
          16384/SiBeta_E_rebin,0,16384);
          DE_E_total->GetXaxis()->SetTitle("E Channel #");
          DE_E_total->GetYaxis()->SetTitle("#DeltaE Channel #");
    }


  for( int s=0; s<4; s++ )
    {
      sprintf(str,"BetaSi_E_%i",s+1);
      sprintf(fn,"BetaSi_E_%i",s+1);
      BetaSi_E[s]=(TH2D*)f->Get(str);
      if( BetaSi_E[s] == 0 )
        {
          BetaSi_E[s] = new TH2D(str,fn,
          16384/SiBeta_E_rebin,0,16384,
          16384/SiBeta_E_rebin,0,16384);
          BetaSi_E[s]->GetXaxis()->SetTitle("Plastic Channel #");
          BetaSi_E[s]->GetYaxis()->SetTitle("Si Channel #");
        }
    }
}
```

```
//////////////////////////////////////////////////////////////////
void GEInit(const char *fn){
  int i;
  string OneLine;

  ifstream CALFILE(fn, ios::in);
  if( CALFILE.is_open() ){
    getline(CALFILE,OneLine);
    printf("\n");
    cout << "Reading calibration file..." << endl;
    cout << "Here's your HPGe information:" << endl;

    for( i=0; i<2;i++ ){
      CALFILE >> gain[i] >> off[i] >> BaseLine[i] >> PZ[i] >> toff[i];
      cout << "HPGe = " << i << " ," << "Gain = " << gain[i] << " ,"
      << "BaseLine = " << BaseLine[i] << ", "
      << "PZ = " << PZ[i] << ", " << "toff = "<< toff[i]
      << endl;
    }
    cout << "\n" << endl;
  }
  else{
    cerr << "Error opening Calibration file "<< fn << endl;
    exit(1);
  }
  CALFILE.close();
}
//////////////////////////////////////////////////////////////////
static unsigned int *GetEvBuf(FILE *fp, const char *FileName){
```

```
  unsigned int      i;
  unsigned int      *TEMP;
  unsigned int      t1, t2, t3, t4;
  GEBheader      *Header;

  Header = (GEBheader*) malloc(GEBHDRLENBYTES);
  if( fread(Header,GEBHDRLENBYTES,1,fp) != 1 ){
    if( feof(fp) ){
      printf("End of file %s\n",FileName);
      fclose(fp);
      return NULL;
    }
    printf("file read error %s\n",FileName);
    return NULL;
  }
  TEMP = (unsigned int*) malloc(Header->length);
  fread(TEMP,Header->length,1,fp);

  for( i=0;i<Header->length/4;i++ ){
    t1 = (TEMP[i] & 0x000000ff) << 24;
    t2 = (TEMP[i] & 0x0000ff00) << 8;
    t3 = (TEMP[i] & 0x00ff0000) >> 8;
    t4 = (TEMP[i] & 0xff000000) >> 24;
    TEMP[i] = t1 + t2 + t3 + t4;
  }
  return TEMP;
}
////////////////////////////////////////////////////////////////////
int GetEv(unsigned int *TEMP, DGSEVENT *DGS, DGSTrace *TRACE){
```

```
static int        nn = 0;
int               i;
int               EventLen;

/* note: no need to swap bytes... */

DGS->chan_id = (unsigned short int) (TEMP[0] & 0xf);
DGS->board_id = (unsigned short int) ((TEMP[0] & 0x00f0)>>4);
EventLen = (unsigned short int) ((TEMP[0] & 0x7ff0000) >> 16) + 1;

DGS->LEDts = 0;
DGS->LEDts = (unsigned long long int) TEMP[1];
DGS->LEDts += ((unsigned long long int) (TEMP[2] & 0x0000ffff)  << 32);

DGS->PreEnergy = (TEMP[7] & 0xffffff);

DGS->PostEnergy = ((TEMP[7] >> 24) & 0xff);
DGS->PostEnergy += ((TEMP[8] & 0xffff) << 8);
DGS->Base = (short int) ((TEMP[12]>>16) & 0x3fff);

DGS->m1_end_sample = (unsigned short int) (((TEMP[10]) & 0x3fff0000) >> 16);
DGS->m1_begin_sample = (unsigned short int) (((TEMP[10]) & 0x00003fff) >> 0);
DGS->m2_begin_sample = (unsigned short int) (((TEMP[11]) & 0x00003fff) >> 0);
DGS->m2_end_sample = (unsigned short int) (((TEMP[11]) & 0x3fff0000) >> 16);
DGS->peak_sample = (unsigned short int) (((TEMP[12]) & 0x00003fff) >> 0);
DGS->base_sample = (unsigned short int) (((TEMP[12]) & 0x3fff0000) >> 16);
DGS->offset_flag = (unsigned short int) (((TEMP[3]) & 0x00000400) >> 10);
```

```
  TRACE->Len = 0;
  for(i = HDRLENINTS; i < EventLen-1; i++)
    if( i<1037 ){
      TRACE->trace[2*(i-HDRLENINTS)] = (short int) (TEMP[i] & 0x3fff);
      TRACE->trace[2*(i-HDRLENINTS)+1] = (short int) ((TEMP[i] >> 16) & 0x3fff);
      TRACE->Len += 2;
    }
  nn++;
  fflush(stdout);
  return 1;
}
////////////////////////////////////////////////////////////////////////////
void ProcessEvent(int EVLEN){
  bool is_moving_assumption = false;
  static float window_start = -1.;
  static bool window_ok = false;
  int i,j;
  int dt;
  tapeflag = false;
  bool boost;

  if( EVLEN >= MaxNumChan ) EVLEN=MaxNumChan;
  for( i=0;i<EVLEN-1;i++ ){

    for( j=i+1;j<EVLEN;j++ ){
       boost = false;
      if ( (event[i].Beta && event[j].Si) || (event[i].Si && event[j].Beta) ) {
        boost = true;
        int a=i; // a is always beta
```

```
int b=j; // b is always silicon
if ( event[i].Si ) {
  a = j;
  b = i;
}

PlasEG = 0.;
SiEG = 0.;
tapeE = 0.;
PlasIDG = -1;
SiIDG = -1;
dt = event[a].t - event[b].t;
dtSiPlasG = dt;
hdtSiB->Fill(dt);

if ( event[b].id == 0 && event[a].id == 0 ) hdtSiB1->Fill(dt);
if ( event[b].id == 1 && event[a].id == 1 ) hdtSiB2->Fill(dt);
if ( event[b].id == 2 && event[a].id == 2 ) hdtSiB3->Fill(dt);
if ( event[b].id == 3 && event[a].id == 3 ) hdtSiB4->Fill(dt);
if ( event[a].id != 0)

BetaE->Fill(event[a].e);
if ( event[a].id == 0 ) BetaE1->Fill(event[a].e);
if ( event[a].id == 1 ) BetaE2->Fill(event[a].e);
if ( event[a].id == 2 ) BetaE3->Fill(event[a].e);
if ( event[a].id == 3 ) BetaE4->Fill(event[a].e);

SiE->Fill(event[b].e);
if ( event[b].id == 0 ) SiE1->Fill(event[b].e);
```

```
if ( event[b].id == 1 ) SiE2->Fill(event[b].e);
if ( event[b].id == 2 ) SiE3->Fill(event[b].e);
if ( event[b].id == 3 ) SiE4->Fill(event[b].e);

SiBeta_Coin->Fill(event[a].id,event[b].id);

if( (event[a].id == event[b].id) && a != 1 && b != 4 ) {
  DE_E_total->Fill(event[a].e,event[b].e);
}

for( int s=0; s<4; s++ ){
    SiBeta_E[s]->Fill(event[a].e,event[b].e);
  }
    SiBeta_E_All->Fill(event[a].e,event[b].e);
    p_LEDts = event[a].t;
    si_LEDts = event[b].t;
    PlasEG = event[a].e;
    SiEG = event[b].e;
    PlasIDG = event[a].id+1;
    SiIDG = event[b].id+1;

    p_EventNum = event[a].numevent;
    si_EventNum = event[b].numevent;
    detrawgated->Fill();
    detrawplas->Fill();
    detrawsi->Fill();
    evtcount +=1;

if( !event[i].Beta && !event[i].Si ){
```

```
  if ( event[j].Si ){
    dt = event[i].t - event[j].t;
     SiGamma_dT_All->Fill(dt);
  }
}

if( event[i].Si ){
  if( !event[j].Beta && !event[j].Si ){
    dt = event[j].t - event[i].t;
    SiGamma_dT_All->Fill(dt);
    if( event[i].id < 4 && event[j].id < 2 )
      Gamma_E_withSi[event[j].id][event[i].id]->Fill(event[j].e);
    if( event[j].id < 2 )
      Gamma_E_withAnySi[event[j].id]->Fill(event[j].e);
  }
}

if( event[j].Si ){
  if(!event[i].Beta && !event[i].Si){
    dt = event[i].t - event[j].t;
    SiGamma_dT_All->Fill(dt);
    if( event[j].id < 4 && event[i].id < 2 )
      Gamma_E_withSi[event[i].id][event[j].id]->Fill(event[i].e);
    if( event[i].id < 2 )
      Gamma_E_withAnySi[event[i].id]->Fill(event[i].e);
  }
}
else if( (!event[i].Beta) && (event[j].Beta) ){
  dt = event[j].t - event[i].t;
```

```
          if( dt>=COINCIWINGBL && dt<=COINCIWINGBH ){
            if(event[j].e<=-10.)
              event[i].WithBeta = true;
          }
        }

        if ( boost )
          break;
      }
    }
  }
}
////////////////////////////////////////////////////////////////////////////
int main ( int argc, char **argv )
{
  detrawgated->Branch("plasEnergyRawGated",&PlasEG,"PlasEG/F");
  detrawgated->Branch("siEnergyRawGated",&SiEG,"SiEG/F");
  detrawgated->Branch("plasIDGated",&PlasIDG,"PlasIDG/I");
  detrawgated->Branch("siIDGated",&SiIDG,"SiIDG/I");
  detrawgated->Branch("dtSiPlasGated",&dtSiPlasG,"dtSiPlasG/D");
  detrawgated->Branch("plasEventNum",&p_EventNum,"p_EventNum/l");
  detrawgated->Branch("siEventNum",&si_EventNum,"si_EventNum/l");

  detrawplas->Branch("id",&PlasIDG,"IDChannel/I");
  detrawplas->Branch("EventNum",&p_EventNum,"EventNum/I");
  detrawplas->Branch("tape_t",&tape_t,"tape_t/l");
  detrawplas->Branch("tapeevt",&tapeevt,"tapeevt/l");
  detrawplas->Branch("plasLEDts",&p_LEDts,"LEDts/l");
  detrawplas->Branch("plasEnergyRaw",&PlasEG,"e/F");
```

```
detrawplas->Branch("tapeE",&tapeE,"tapeE/F");


detrawsi->Branch("id",&SiIDG,"IDChannel/I");
detrawsi->Branch("EventNum",&si_EventNum,"EventNum/I");
detrawsi->Branch("siLEDts",&si_LEDts,"LEDts/l");
detrawsi->Branch("siEnergyRaw",&SiEG,"e/F");
detrawsi->Branch("tape_t",&tape_t,"tape_t/l");
const float d = (float) (RAND_MAX) + 1.0;
#include "ChanMap.h"
int status;
const char *DataName;
const char *RootName;
const char *OPTION;
const char *CalName;
FILE *fp1;
TFile *f;
unsigned int *EventBuf=NULL;
int EVLEN,NumEv;
int NumBeta[NumB]={0},NumGamma[NumGe]={0},NumBSi[NumSi]={0};
long EventNum=0;
unsigned long long int tsGamma0[NumGe]={0};
unsigned long long int tsFirst=0,tsLast=0;
unsigned long long int tsEarliest=0,tsLatest=0;
unsigned long long int tsDelta=0;
unsigned short int id;
int IDChannel;
int dt;


float begin1,end1,base1;
```

```
float begin2,end2,base2;
float sum1,sum2,energy;
float pz1,amp;
float sumpz1[2]={0.0};
float npz1[2]={0.0};

DGSEVENT DGS;
DGSTrace TRACE;

if ( argc!=5 ) {
  printf("USAGE: RootFileName DataName OPTION CalFileName\n");
  exit(-1);
}
time_t t = time(0);
tm* localtm = localtime(&t);
printf("\n");
cout << "The local date and time is: " << asctime(localtm) << endl;
printf("RootName is %s\n",argv[1]);
RootName = argv[1];
printf("OPTION is %s\n",argv[3]);
OPTION = argv[3];
f = new TFile(RootName,OPTION);
setuproot(f);

printf("HPGe Calibration File is %s\n",argv[4]);
CalName = argv[4];

printf("DataName is %s\n",argv[2]);
DataName = argv[2];
```

```
fp1 = fopen(DataName,"rb");
GEInit(CalName);

EVLEN=0;NumEv=0;
if( (EventBuf=GetEvBuf(fp1,DataName) )!=NULL){
  status=GetEv(EventBuf,&DGS,&TRACE);
  tsFirst = DGS.LEDts;
  tsLast = DGS.LEDts;
  tsEarliest = DGS.LEDts;
  tsLatest = DGS.LEDts;
  free(EventBuf);
}

while( (EventBuf=GetEvBuf(fp1,DataName))!=NULL ){
  status=GetEv(EventBuf,&DGS,&TRACE);
  free(EventBuf);
  hid->Fill(DGS.board_id,DGS.chan_id);
  dt = (int)DGS.LEDts - (int)tsLast;
  tsLast = DGS.LEDts;
  id = ChanMap[DGS.board_id*10+DGS.chan_id];
  mapid->Fill(id);

  if( DGS.LEDts > tsLatest )tsLatest=DGS.LEDts;
  else if( DGS.LEDts < tsEarliest )tsEarliest=DGS.LEDts;

  if( ChanType[id]==ChanGamma ){

    if( NumGamma[id]==0 )tsGamma0[id] = DGS.LEDts;
    if( (float)DGS.PostEnergy/Mwidth > 16384 ) DGS.e= DGS.e + 16384*Mwidth;
```

```
DGS.e = ((float)DGS.PostEnergy - (float)DGS.PreEnergy*PZ[id])/Mwidth;
DGS.e-= BaseLine[id]*(1.-PZ[id]);
DGS.e = DGS.e*gain[id]+off[id];
GamERaw->Fill(DGS.e,id);

sum1 = (float)DGS.PreEnergy/Mwidth;
sum2 = (float)DGS.PostEnergy/Mwidth;
begin1 = (float)DGS.m1_begin_sample+(float)rand()/d-0.5;
end1 = (float)DGS.m1_end_sample+(float)rand()/d-0.5;
end2 = (float)DGS.m2_end_sample+(float)rand()/d-0.5;
begin2 = (float)DGS.m2_begin_sample+(float)rand()/d-0.5;
base1 = (sum2*begin1-sum1*begin2)/((sum2-sum1)-(begin2-begin1));
base2 = (end1*begin2-begin1*end2)/((begin2-end2)-(begin1-end1));
pz1 = (end1-end2)/(begin1-begin2);

if( pz1>=0.7 && pz1<=1.10 ){
  sumpz1[id]+=pz1;
  npz1[id]+=1.0;
}

amp = sum2-sum1;
energy  = sum2 - sum1*PZ[id];
energy -=BaseLine[id]*(1.-PZ[id]);
energy  = energy *gain[id]+off[id]+(float)rand()/d-0.5;
baseCal1->Fill(base1-BaseLine[id],id);
baseCal2->Fill(base2-BaseLine[id],id);
baseRaw->Fill(TRACE.trace[0],id);
pz1Cal->Fill(powf(pz1,(Mwidth+Kwidth)/Mwidth),id);
```

```
  tb[id]->Fill(energy*0.3333333,TRACE.trace[0]-BaseLine[id]);

  if( id == 0 ){
    GamERaw1->Fill(DGS.e);
    gb1->Fill( DGS.e,TRACE.trace[0] );
  }
  if( id == 1 ){
    GamERaw2->Fill(DGS.e);
    gb2->Fill( DGS.e,TRACE.trace[0] );

    IDChannel = id;
    detrawge->Fill();
  }
  NumGamma[id]++;
}

// For Si detectors
else if( ChanType[id]==ChanSi ){
  DGS.e = ((float)DGS.PostEnergy - (float)DGS.PreEnergy)/Mwidth;
  if ( DGS.e < 0 )
      DGS.e += 16384;
  SiERaw->Fill(DGS.e,id);
  if( id == 6 ){
    SiERaw1->Fill(DGS.e);
  }
  if( id == 7 ){
    SiERaw2->Fill(DGS.e);
  }
  if( id == 8 ){
```

```
    SiERaw3->Fill(DGS.e);
  }
  if( id == 9 ){
    SiERaw4->Fill(DGS.e);
  }
  NumBSi[id]++;
}

else if( ChanType[id] == ChanBeta ){
  DGS.e = -1.0*((float)DGS.PostEnergy - (float)DGS.PreEnergy)/Mwidth;

  if ( DGS.e < 0 )
    DGS.e += 16384;
    BetaERaw->Fill(DGS.e,id);

  if( id == 2 ){
    BetaERaw1->Fill(DGS.e);
   }
  if( id == 3 ){
    BetaERaw2->Fill(DGS.e);
  }
  if( id == 4 ){
    BetaERaw3->Fill(DGS.e);
  }
  if( id == 5 ){
    IDChannel = id;
    BetaERaw4->Fill(DGS.e);
  }
  NumBeta[id]++;
```

```
}
tsDelta = tsLatest - tsEarliest;
if( tsDelta > OverLapWin ){
  ProcessEvent(NumEv);
  NumEv=0;
  if( ChanType[id] == ChanGamma ){
    event[NumEv].Si=false;
    event[NumEv].Beta=false;
    event[NumEv].WithBeta=false;
    event[NumEv].t = DGS.LEDts+toff[id];
    event[NumEv].e = DGS.e;
    event[NumEv].id = id;
    event[NumEv].numevent = EventNum;
    NumEv++;
  }
  else if( ChanType[id] == ChanBeta ){
    event[NumEv].Si = false;
    event[NumEv].Beta = true;
    event[NumEv].t = DGS.LEDts;
    event[NumEv].e = DGS.e;
    event[NumEv].id = id-2;
    event[NumEv].numevent = EventNum;
    NumEv++;
  }
  else if ( ChanType[id] == ChanSi ){
    event[NumEv].Si=true;
    event[NumEv].Beta=false;
    event[NumEv].t = DGS.LEDts;
    event[NumEv].e = DGS.e;
```

```
    event[NumEv].id = id-6;
    event[NumEv].numevent = EventNum;
    NumEv++;
  }
  tsEarliest = DGS.LEDts;
  tsLatest = DGS.LEDts;
}
else{
  if( NumEv<MaxNumChan ){
    if( ChanType[id] == ChanGamma ){
      event[NumEv].Si = false;
      event[NumEv].Beta = false;
      event[NumEv].WithBeta = false;
      event[NumEv].t = DGS.LEDts+toff[id];
      event[NumEv].e = DGS.e;
      event[NumEv].id = id;//-1;
      event[NumEv].numevent = EventNum;
      NumEv++;
    }
  else if( ChanType[id] == ChanBeta ){
      event[NumEv].Si = false;
      event[NumEv].Beta = true;
      event[NumEv].t = DGS.LEDts;
      event[NumEv].e = DGS.e;
      event[NumEv].id = id-2;
      event[NumEv].numevent = EventNum;
      NumEv++;
    }
  else if ( ChanType[id] == ChanSi ){
```

```
        event[NumEv].Si = true;
        event[NumEv].Beta=false;
        event[NumEv].t = DGS.LEDts;
        event[NumEv].e = DGS.e;
        event[NumEv].id = id-6;
        event[NumEv].numevent = EventNum;
        NumEv++;
      }
    }
  }

EventNum++;

if( (EventNum % 1000000) == 0 )
  {
    printf("%ld Events Processed\n",EventNum);
  }
}

for( int s=0; s<4; s++ )
{
  char name[20];
  sprintf(name,"SiBeta_E_X_%i",s+1);
  SiBeta_E_X[s] =  (TH1D*) SiBeta_E[s]->ProjectionX(name);
  sprintf(name,"SiBeta_E_Y_%i",s+1);
  SiBeta_E_Y[s] =  (TH1D*) SiBeta_E[s]->ProjectionY(name);
}

SiBeta_E_All_X = (TH1D*) SiBeta_E_All->ProjectionX("SiBeta_E_All_X");
```

```
  SiBeta_E_All_Y = (TH1D*) SiBeta_E_All->ProjectionY("SiBeta_E_All_Y");
  SiBeta_E_All_Y->GetXaxis()->SetRangeUser(-1000.,9000.);

  cout << "********************" << endl;
  printf("Total %d Events in Collection Window\n",evtcount);
  printf("Total %ld Events Processed\n",EventNum);
  printf("Writing...\n");

  detrawge->Write();
  detrawsi->Write();
  detrawsi->GetEntries();
  detrawplas->Write();
  detrawplas->GetEntries();
  detrawgated->Write();
  detrawgated->GetEntries();
  f->Write("",TObject::kOverwrite);
  f->Close();
  printf("Finished sorting successfully.\n");
  exit(0);
}
```

A.2 FP.h

```
//////////////////////////////////////
/// FP.h                           ///
//////////////////////////////////////

#define TRUE 1
```

```
#define FALSE 0
#define NOTDEF -1
#define STRLEN 256

#define EOE          0xaaaaaaaa
#define HDRLENBYTES  52
#define HDRLENWORDS  26
#define HDRLENINTS   13
#define MAXLENINTS   525
#define LENEOVWORDS  2
#define GEBHDRLENBYTES 16

typedef struct DGSEVENT_struct
{
  unsigned short int      chan_id;
  unsigned short int      board_id;
  unsigned long long int  LEDts;
  int                     PreEnergy;
  int                     PostEnergy;
  short int     Base;
  short int     BaseSample;
  short int     PeakSample;
  float       e;

  unsigned short int      m1_begin_sample;
  unsigned short int      m1_end_sample;
  unsigned short int      m2_begin_sample;
  unsigned short int      m2_end_sample;
  unsigned short int      peak_sample;
```

```
  unsigned short int      base_sample;
  unsigned short int      offset_flag;
}  DGSEVENT;

typedef struct DGSTrace_struct
{
  unsigned short int      Len;
  short int               trace[1024];
}  DGSTrace;

typedef struct EVENT_struct
{
  bool               Beta;
  bool               Si;
  bool               Gam;
  bool               TapeSig;
  unsigned short int id;
  unsigned long long int t;
  unsigned long long int LEDts;
  float              e;
  bool               WithBeta;
  double             Tape;
  double             Buncher;
  int                BuncherID;
  int                numevent;
}EVENT;

typedef struct GEBheader_struct
{
```

```
  unsigned int           type;
  unsigned int           length;
  unsigned long long int timestamp;
} GEBheader;
```

A.3 ChanMap.h

```
//////////////////////////////////////
/// ChanMap.h                      ///
//////////////////////////////////////

/* Channel for digitizer*/

ChanMap[50]=0;
ChanMap[51]=1;
ChanMap[52]=2;
ChanMap[53]=3;
ChanMap[54]=4;
ChanMap[55]=5;
ChanMap[56]=6;
ChanMap[57]=7;
ChanMap[58]=8;
ChanMap[59]=9;

/* Defines what is going in channel*/
ChanType[0]=ChanGamma;
ChanType[1]=ChanGamma;
```

```
ChanType[2]=ChanBeta; // Tape signal

ChanType[3]=ChanBeta; // Plas #2

ChanType[4]=ChanBeta; // Plas #3

ChanType[5]=ChanBeta; // Plas #4

ChanType[6]=ChanSi; // Si #1

ChanType[7]=ChanSi; // Si #2

ChanType[8]=ChanSi; // Si #3

ChanType[9]=ChanSi; // TTL signal
```